Proximity Analysis of Native Proteomes Reveals Interactomes Predictive of Phenotypic Modifiers of Autism and Related Neurodevelopmental Conditions

Authors: Yudong Gao[1], Matthew Trn[1], Daichi Shonai[2], Jieqing Zhao[3], Erik J. Soderblom[4], S. Alexandra Garcia-Moreno[5], Charles A. Gersbach[5,6], William C. Wetsel[7], Geraldine Dawson[8], Dmitry Velmeshev[9], Yong-hui Jiang[10], Laura G. Sloofman[11], Joseph D. Buxbaum[11,12], Scott H. Soderling[1,9,*]

Affiliations:

[1] Department of Cell Biology, Duke University School of Medicine, Durham, NC, USA

[2] Department of Molecular Genetics and Microbiology, Duke University School of Medicine, Durham, NC, USA

[3] Department of Biology, Duke University, Durham, NC, USA

[4] Department of Cell Biology, Proteomics and Metabolomics Shared Resource, Duke University School of Medicine, Durham, NC, USA

[5] Department of Biomedical Engineering, Duke University, Durham, NC, USA.

[6] Center for Advanced Genomic Technologies, Duke University, Durham, NC, USA; Department of Cell Biology, Duke University Medical Center, Durham, NC, USA; Department of Surgery, Duke University Medical Center, Durham, NC, USA.

[7] Departments of Psychiatry and Behavioral Sciences, Cell Biology, and Neurobiology, Mouse Behavioral and Neuroendocrine Analysis Core Facility, Duke University School of Medicine, Durham, NC, USA.

[8] Department of Psychiatry and Behavioral Sciences, Duke University School of Medicine, Durham, NC, USA.

[9] Department of Neurobiology, Duke University School of Medicine, Durham, NC, USA

[10] Department of Genetics, Yale University School of Medicine, New Haven, Connecticut, USA.

[11] Seaver Autism Center for Research and Treatment, Icahn School of Medicine at Mount Sinai, New York, NY, USA; Department of Psychiatry, Icahn School of Medicine at Mount Sinai, New York, NY, USA

[12] The Mindich Child Health and Development Institute, Icahn School of Medicine at Mount Sinai, New York, NY, USA; Friedman Brain Institute, Icahn School of Medicine at Mount Sinai, New York, NY, USA.

*Corresponding author. Email: Scott.Soderling@duke.edu

Abstract: One of the main drivers of autism spectrum disorder is risk alleles within hundreds of genes, which may interact within shared but unknown protein complexes. Here we develop a scalable genome-editing-mediated approach to target 14 high-confidence autism risk genes within the mouse brain for proximity-based endogenous proteomics, achieving high specificity spatial interactomes compared to prior methods. The resulting native proximity interactomes are enriched for human genes dysregulated in the brain of autistic individuals and reveal unexpected and highly significant interactions with other lower-confidence autism risk gene products, positing new avenues to prioritize genetic risk. Importantly, the datasets are enriched for shared cellular functions and genetic interactions that may underlie the condition. We test this notion by spatial proteomics and CRISPR-based regulation of expression in two autism models, demonstrating functional interactions that modulate mechanisms of their dysregulation. Together, these results reveal native proteome networks *in vivo* relevant to autism, providing new inroads for understanding and manipulating the cellular drivers underpinning its etiology.

Introduction

Autism spectrum disorder (hereinafter "autism") is a neurodevelopmental condition associated with social communication difficulties and restricted and repetitive behaviors. Autism presents with significant clinical heterogeneity and complex genetic etiology [1]. Decades of research have identified and curated an evolving list of gene mutations associated with autism risk, many of which converge on pathways mediating synaptic/axonal functions and gene regulation [2-7], and exhibit cell-type specific expression patterns across the brain [8]. Until recently, evidence of shared biology across these risk genes has been inferred primarily from RNA-level gene expression results [9-11], or interpreted from protein interaction analyses [12-15], although these are often derived from non-neuronal cells. Thus, there is a prevailing notion in the literature that molecular convergence in autism may be optimally reflected at the protein level in the brain.

One hallmark of neurons is their distinctive sub-cellular compartmentation - such as the synapse and axonal initial segment (AIS) - that are pivotal for neurotransmission [16,17]. In addition, gene expression regulators, many of which reside within the nucleus, also orchestrate key milestones of neurodevelopment [6]. It is not surprising that autism risk converges on genes encoding proteins

62 associated with these sub-cellular compartments [18-22]. Identifying the autism-associated proteome
63 architecture of these compartments could define how seemingly diverse genetic mutations are
64 functionally connected, thereby providing a new roadmap to reveal a converging autism etiology.
65 Current efforts to dissociate protein complexes and protein-protein interactions (PPIs) rely upon
66 techniques such as cellular fractionation, immunoaffinity purification, cross-linking, and
67 proximity-based proteomic methods, including biotin-identification (BioID) [23-30]. However, due
68 to inherent specificity constraints of antibody-dependent immunoprecipitation or recombinant
69 exogenous promoter-based strategies that express proteins at non-physiologic levels in non-native
70 cell types, access to the native proximity interactomes of endogenously expressed autism risk
71 proteins within brain tissue remains a significant challenge. Given these limitations, high-fidelity
72 proteomes organized around autism risk proteins in the brain are clearly needed for better
73 mechanistic insights.
74
75 Previously, we published a two-vector CRISPR/Cas9 approach, Homology independent Universal
76 Genome Engineering (HiUGE), which enables rapid endogenous neuronal gene knock-in for
77 protein modification *in vivo* [31]. Here, we have leveraged HiUGE and simplified it with a one-vector
78 design to achieve a robust knock-in in brain tissue with an engineered biotin ligase, TurboID [32],
79 for scalable proximity proteomics of endogenous protein complexes. The approach is flexible also
80 from a protein engineering perspective, as the proteins can be modified by placing TurboID within
81 terminal coding exons or internally within introns using splicing sequences [33]. Importantly,
82 because this strategy uses AAV transduction of readily available Cas9-transgenic mice, it obviates
83 the significant time and cost burden of the traditional method of generating *in vivo* fusions of
84 endogenous proteins by producing transgenic mice via germline transmission. Coupling this
85 approach with *in vivo* BioID (iBioID) [23], we have targeted 14 genetic drivers of autism that are
86 mapped to the synapse, AIS, or the nucleus. Out of these 14 targets, 13 are SFARI gene score 1,
87 one is gene score 2, also noted as syndromic, and 7 are from the autism risk gene lists of Satterstrom
88 et al., 2020 [3], or Fu et al., 2022 [7]. With this approach, we have modified the endogenous proteins
89 with TurboID and then unraveled their native proximal proteomes directly from brain tissue for
90 the first time to our knowledge. We have identified 1252 proteins within these 14 proximity
91 proteomic interactomes (hereinafter "interactomes") and 3264 proximity PPIs associated with
92 these autism targets. Amongst them, 16% are proteins encoded by mouse orthologs of SFARI

genes [2], 8% overlap with differentially expressed genes (DEGs) found in brain tissue of autistic individuals [8], and 65% of the PPIs are not reported in STRING queries [34,35]. Importantly, direct comparisons of HiUGE-iBioID to the prior "gold standard" of immunoprecipitation revealed its interactomes are more specific to the baits' biological functions, containing far fewer proteins with potential off-target functions. Similar conclusions are drawn from comparison with results obtained from non-native recombinant BioID expression *in vitro*, supporting the advantages of native interactome discovery using HiUGE-iBioID *in vivo*. Notably, the interactomes contain products of many newly discovered autism risk genes identified in recent studies [7,36-38] and reveal shared biological processes among autism proteins that may be predictive of interactions influencing autism phenotypes.

We have tested this notion by identifying intersections between HiUGE-iBioID interactomes and co-perturbed proteins in two autism mouse models (Syngap1 synaptopathy and Scn2a channelopathy). In the Syngap1 model, we find that its binding with Anks1b is disrupted by an autism-associated Syngap1 mutation, and their interaction is essential for shaping neural activity during critical synaptogenesis periods. In the Scn2a model, we show that a patient-derived missense mutation results in repetitive behaviors and abnormal social communication in mice. The mutation also downregulates a key Scn2a modulatory protein cluster discovered in its interactome and results in aberrant attenuation of neural activity. Strikingly, re-expression of this cluster rescues this autism-associated electrophysiological impairment.

Together, our results establish a new scalable platform to engineer endogenous proteins and map native proximity interactomes at the protein-level that are associated with genetic risks for neurodevelopmental conditions such as autism. Our findings also reveal an intersectional approach to prioritize candidates based on proteomic co-perturbation. These data support a protein-centric model to reveal novel mechanisms of autism and related neurodevelopmental disorders and potential mitigation approaches.

Results

Endogenous labeling of autism risk proteins using HiUGE

124

125 Previously we have used overexpression of bait proteins fused to various biotin ligases to discover
126 interactomes from brain tissue [23,39] . Although this approach has been highly successful, it is known
127 that the expression of proteins using artificial promoters may result in non-native interactions due
128 to non-physiological expression levels and/or expression in inappropriate cell types. To overcome
129 these issues, cell lines harboring CRISPR-edited knock-ins (KIs) of TurboID have been utilized
130 [40]. Nonetheless, such approaches are limited by the inability to recapitulate the diversity of
131 neuronal cell types that exist *in vivo*, and cultured cells cannot replicate many conditions governed
132 by native neuropil interactions. To address this technological gap, we developed a new approach
133 for iBioID experiments with in-frame TurboID fusions introduced into endogenous gene regions
134 by HiUGE genome editing (Fig. 1A). Using a highly expressed gene Tubb3 as a pilot example, we
135 confirmed that the HiUGE-iBioID yields efficient *in vivo* KI and biotinylation in neurons across
136 the brain (Fig. S1A).

137

138 Because autism is driven by mutations in a large number of risk genes whose products may interact
139 with each other in unknown functional ways, we next targeted 14 high-confidence autism risk
140 genes from the SFARI gene list (*Anks1b*, *Syngap1*, *Shank2*, *Shank3*, *Nckap1*, *Nbea*, *Ctnnb1*,
141 *Lrrc4c*, *Iqsec2*, *Arhgef9*, *Ank3*, *Scn2a*, *Scn8a*, and *Hnrnpu*) that are expressed in neuronal
142 compartments of the synapse, AIS, and nucleus [2,41,42]. Note, due to packaging limits, many of these
143 protein targets are too large to overexpress using conventional AAV methods, which further
144 supports the need to label the endogenous copies of these genes. Importantly, for targets with C-
145 terminal (C-term) PDZ-binding motifs (Syngap1, Ctnnb1, Iqsec2, and Lrrc4c), intron-targeting [33]
146 or custom donor strategies were used to preserve these critical protein-interaction sites (Fig. 1A).
147 First, to confirm the proper localization of HiUGE-labeled targets, a highly immunogenic spaghetti
148 monster (smFP) tag [43], similar in size to TurboID, was used to visualize fusion proteins. We found
149 that HiUGE-labeled proteins were either properly localized to the synaptic sites, colocalizing with
150 the Homer1 immunosignal (Fig. S1B-J, Q), or were restricted to the distinct features of the AIS
151 and nuclear compartments (Fig. S1L-O). We further validated that the HiUGE-labeling was
152 colocalized with the immunofluorescence of specific antibodies, demonstrating the localization of
153 these proteins was not affected by the tag fusion (Fig. S2). Having thus confirmed proper genome
154 editing and correct fusion protein localization, we next fused each protein *in vivo* with TurboID-

155 HA by injecting HiUGE AAV directly into Cas9 transgenic neonatal pup brains (P0-2), and then
156 biotinylated surrounding proteins by supplying biotin via intraperitoneal (i.p.) injections over 5
157 consecutive days starting at ~P21. Western blot analyses of the purified streptavidin-precipitations
158 from forebrain lysates collected at ~P26 detected epitope-tagged baits at the expected molecular
159 masses, confirming correct TurboID fusion protein expression (Fig. S3A-H).
160
161 **HiUGE-iBioID reveals endogenous interactomes associated with autism risk proteins of**
162 **diverse subcellular compartments.**
163
164 LC-MS/MS analysis of the 14 HiUGE-iBioID samples detected a total of 1252 proteins that were
165 enriched in the bait proteomes, with expected interactions faithfully captured (Fig. 1B, S11-24,
166 Table S1,2). Importantly, 65% of the interactions detected were new, being absent from STRING
167 queries (using a generous stringency interaction score of 0.15 [34,35]) - likely a reflection of prior
168 studies being conducted in non-neuronal cell types or methods other than proximity proteomics.
169 Gene ontology (GO) analyses revealed highly cohesive cellular functions corresponding to the
170 known biology of the bait proteins, such as pathways associated with synaptic transmission
171 (Anks1b, Syngap1, Shank2, Shank3, Nckap1, Nbea, Ctnnb1, Lrrc4c, Iqsec2, Arhgef9), voltage-
172 gated channel activity (Ank3, Scn2a, Scn8a), and RNA processes (Hnrnpu); thereby demonstrating
173 high fidelity identification of local interactomes (Fig. S11-24, S27). These networks were also
174 consistent with the latest knowledge of the structures and functions of specific neuronal
175 compartments. For example, the detection of Mical3 and Septin complexes with the AIS baits (Fig.
176 S21-23, Table S2) echoed a previous study that suggested their roles in regulating cytoskeletal
177 stability and polarized trafficking at the AIS [24]. Reciprocal analyses also supported the
178 reproducibility of the interactomes, showing that the baits frequently cross-identified each other
179 (Fig. S4A, Table S2). Additional HiUGE-iBioID of proteomic "hubs" (e.g., Homer1 and Wasf1,
180 which were commonly associated with many baits) demonstrated they could reversely detect the
181 majority of baits in validation experiments (Fig. S4B-H). In addition, comparisons showed that
182 HiUGE-iBioID interactomes significantly overlap with, but also differ from proteomic detections
183 derived from independent antibody immunoprecipitations we performed for Anks1b and Scn2a
184 (Fig. S4I, J). Interactions specific to HiUGE-iBioID compared to these antibody pulldowns were
185 expected since BioID is based on covalent labeling of nearby proteins and thus does not require

186 transient or weak interactions to survive the pulldown and washing steps of immunoaffinity
187 purification. Of note, proteomic detections unique to HiUGE-iBioID conformed to the expected
188 top molecular function GO terms of Anks1b and Scn2a, while detections unique to
189 immunoprecipitations did not (Fig. S4K, L). These data demonstrate that HiUGE-iBioID excels in
190 specificity for detecting biologically-relevant proteomic interactions.
191
192 We also sought to determine if the interactomes showed a significant overlap with differentially
193 expressed genes (DEGs) from specific cell types in autistic individuals by cross-referencing a
194 recent human tissue single-cell genomics study [8]. HiUGE-iBioID networks showed the highest
195 level of overlap with autism DEGs in cortical layer 2/3 (L2/3) excitatory neurons (Fig. S5A),
196 consistent with the study suggesting L2/3 neurons are significantly affected in autism [8]. Notably,
197 most networks were also significantly enriched for other autism risk genes (SFARI, Satterstrom et
198 al. [3], and Fu et al. [7]; Fig. 1C, S5B), demonstrating the convergence of autism genetic susceptibilities
199 at the protein interaction level in previously unknown ways. We also performed enrichment
200 analyses between these networks and an autism genome-wide association meta-analysis (GWAS)
201 study [44]; however, the result was largely nonsignificant or marginal, likely due to limited power
202 (Table S7). It has also been noted that larger autism cohorts [38], or new approarchs, are needed to
203 determine the potential genome-wide significance of a large number of moderate-risk genes.
204 Importantly, the HiUGE-iBioID networks of high-confidence autism risk proteins formed physical
205 communities with other candidate proteins of moderate confidence (Table S2, overlap tab). These
206 genes represent a resource of moderate autism candidates that likely should be prioritized in future
207 studies of genetic contributions due to their possible functional interactions with high-confidence
208 autism risk genes. Furthermore, we noted the interactomes contained numerous potentially
209 druggable targets, including ~ 80 kinases and phosphatases, 18 of which are encoded by SFARI
210 gene mouse orthologs: Camk2a, Camk2b, Cask, Cdc42bpb, Cdkl5, Csnk1e, Csnk2a1, Dyrk1a,
211 Mapk3, Ntrk2, Ntrk3, Ocrl, Pak1, Pak2, Ppp3ca, Rps6ka2, Taok2, Wnk3.
212
213 Finally, similarity clustering of the bait interactomes revealed subgroups that largely segregated
214 according to their expected cellular compartments (Fig. 1D). Networks of the overlapping
215 interactomes between two baits with highly significant SFARI gene enrichment (Syngap1 and
216 Anks1b) and three similarity-clustered AIS baits (Ank3, Scn2a, and Scn8a) revealed shared

217 pathways that emphasized glutamate receptor and voltage-gated channel activities, respectively,
218 and common modules that were involved in actin organization in both networks (Fig. 1E-F). These
219 interactomes may contain proteins that function together with the autism-associated baits,
220 modulation of which may reveal the complex genetic risks of autism or serve as potential inroads
221 for normalizing relevant phenotypes.
222
223 **Syngap1 mutations lead to reshaping of its synaptic interactome and loss of Anks1b binding.**
224
225 We hypothesized that protein interactome discovery could inform functional interactions relevant
226 to the phenotypes underlying autism. To test this proposition, we first focused on the intersection
227 between Syngap1 and Anks1b, as their proteomes show a high degree of overlap and exhibit
228 significant SFARI gene enrichment (Fig. 1C). Markov cluster algorithm (MCL) [45] analysis of their
229 overlapping interactome identified a large PPI community (27 proteins, including Syngap1 and
230 Anks1b), that was significantly enriched for pathways of "autistic disorder" and "glutamate
231 receptor activity", indicating this shared cluster may regulate excitatory synaptic transmission in
232 autism. Although molecular interaction between Syngap1-Anks1b has been reported previously
233 [27,46-48], an understanding of their functional interaction remains limited. Prior studies have
234 indicated that Anks1b and Syngap1 both regulate synaptic activity and plasticity through NMDA-
235 type glutamate receptors [49,50], they are dispersed from the PSD in response to synaptic activity in
236 a CaMKII-dependent manner [51-53], and are associated with similar autism-like phenotypes in
237 haploinsufficiency models [54,55]. Hence, we sought to test whether Syngap1 and Anks1b
238 functionally interact in driving neuronal phenotypes.
239
240 We first analyzed the synaptic proteomes in wildtype (WT) and Syngap1 heterozygous (Syngap1-
241 Het) mice [56-58] (Fig. 2A) to determine if Anks1b was influenced by haploinsufficiency of Syngap1.
242 Fractionation steps were performed to isolate the synaptosomes [26,59,60] from the cerebral cortex and
243 striatum. In Syngap1-Het mice, Anks1b was depleted (~60%) to a level similar as for Syngap1 in
244 both cortical and striatal synaptosomes of Syngap1-Het mice (Fig. 2B, Table S4), supporting the
245 notion of a very close functional interaction between Syngap1 and Anks1b not only in typical
246 physiology, but also in autism-associated synaptopathy.
247

248 As truncating mutations of Syngap1 confer significant genetic risk for autism [50,55], we next asked
249 whether these mutations predicted to be pathogenic might lead to perturbation of its interactors,
250 including Anks1b. When expressed in HEK293T cells, C-term truncation of human SYNGAP1 at
251 amino acids (a.a.) 730 (C1-Trunc) and a.a. 848 (C2-Trunc) completely abolished binding with
252 ANKS1B. In contrast, the interaction was retained with truncation at a.a. 1181 (C3-Trunc) or a
253 truncation missing the N-term a.a. 2-361 (N-Trunc). These results suggest that the sequence
254 surrounding the disordered region of SYNGAP1 (a.a. 848-1181) is crucial for the interaction with
255 ANKS1B (Fig. S6). A pathological mutation found in a human patient (SYNGAP1-
256 c.2214_2217del [61]), which resulted in a frame-shift and premature truncation in this region, also
257 abolished the SYNGAP1-ANKS1B interaction (Fig. 2C). A previous report showed that a 2 a.a.
258 substitution in the C-term PDZ-binding motif of Syngap1 impaired several synaptic PPIs, but not
259 Anks1b [62]. As an orthogonal validation of the putative Anks1b interaction region identified above,
260 we sought to test if a more disruptive truncation of Syngap1 that ablated this region could lead to
261 a deeper remodeling of its interactome, including a loss of the Anks1b interaction *in vivo*.
262 Endogenously expressed smFP-labeled Syngap1 truncated at exon 13 (Syngap1:1-744-smFP)
263 retained synaptic localization in cultured neurons, although mis-localization in the soma was
264 detected as well (Fig. 2D). We then targeted this locus to generate TurboID fusion to the truncated
265 Syngap1 protein. HiUGE-iBioID revealed that although some interactors were preserved in
266 Syngap1:1-744 (e.g., Dlg3, Shisa9, Prickle1), most of its synaptic interactions were abolished,
267 including Anks1b (Fig. 2E-G, Table S1). Thus, we confirmed that the region identified by
268 structure-function analysis *in vitro* is also crucial for the Syngap1-Anks1b interaction *in vivo*.
269
270 **Depletion of Anks1b exacerbates electrophysiological abnormalities associated with Syngap1**
271 **during *in vitro* neural development.**
272
273 We next sought to determine whether Syngap1 and Anks1b functionally interact by asking if
274 further depletion of Anks1b would ameliorate or aggravate the phenotypes found in Syngap1 loss-
275 of-function (LOF) mutants (Fig. 2H). AAV-mediated CRISPR disruption targeting Syngap1 at
276 exon 13 and the first common exon of Anks1b (exon 15) led to a profound loss of their total protein
277 (Fig. 2I). Using a multielectrode array (MEA) system to monitor electrophysiological activities
278 longitudinally during neurodevelopment, we observed elevated firing rate and burst activities in

279 Syngap1-gRNA treated neurons at DIV11, but not at DIV8 or DIV14 (Fig. 2J-M). This result
280 phenocopied previous reports demonstrating that Syngap1 LOF atypically accelerated synaptic
281 and network activities during the synaptogenesis period [63,64]. Interestingly, further depletion of
282 Anks1b exacerbated the abnormally heightened neural activity linked to Syngap1 mutation (Fig.
283 2J-M), primarily during the period of synaptogenesis (DIV 11). Taken together, the data support a
284 model in which Syngap1 and Anks1b physically and functionally interact within a common
285 pathway to regulate the development of neuronal activity. Based on the phenotype and common
286 biological pathways found in the overlapping interactomes, this effect may be due to the altered
287 developmental trajectory of the glutamate receptor module found in both networks.
288
289 **HiUGE-iBioID and spatial co-perturbation proteomics reveal targets that can restore**
290 **spontaneous activity of neurons harboring a patient-derived Scn2a$^{+/R102Q}$ mutation.**
291
292 Another critical rationale for interrogating endogenous interactomes is the prospect of identifying
293 proteins functioning with the autism-implicated targets that can be modulated to buffer or
294 normalize phenotypes. Such candidates could be relevant targets for future drug development. To
295 test this possibility, we focused on Scn2a, mutations of which are one of the most highly significant
296 for association with autism [3,65-67]. In recent years, whole exome sequencing (WES) from autistic
297 individuals identified a missense mutation, SCN2A-p.R102Q, that was previously reported [68,69]
298 but uncharacterized. Clinical observations of one patient with this mutation included meeting
299 DSM-5 diagnostic criteria for autism spectrum disorder (i.e., qualitative differences in social
300 communication and the presence of restrictive interests/repetitive behaviors), minimal use of
301 spoken language, disruptive and impulsive behaviors, sleep problems, and gastrointestinal
302 concerns (reflux and constipation). A neurological exam including EEG did not reveal evidence
303 of epilepsy. To test the mechanistic linkage of this mutation to autism, we generated a Scn2a point-
304 mutant heterozygous mouse model (Scn2a$^{+/R102Q}$) (Fig. 3A). Behavioral testing of the Scn2a$^{+/R102Q}$
305 mice found that compared to WT littermates, the mutants presented with hyperactivity and reduced
306 anxiety in the elevated zero maze, excessive repetitive behaviors in the self-grooming and the hole-
307 board tests, and reduced ultrasonic vocalizations (USV) during social interactions (Fig. 3B). Social
308 behavioral tests were also conducted with the resident-intruder and social dyadic assays where
309 C3H/HeJ males served as social partners of WT and Scn2a$^{+/R102Q}$ males. In both the resident-

310 intruder and the dyadic tests, the social behaviors of the mutants appear to be relatively similar to
311 WT, although abnormal numbers of social events and reduced withdrawal were noted (Fig. S7).
312 Hence, the primary behavioral deficits of Scn2a$^{+/R102Q}$ mice lie within social communication and
313 repetitive behaviors. It is known that mutations in Scn2a can result in either infantile epileptic
314 encephalopathy (IEE) or autism, depending upon the nature of the mutational effect (gain- or loss-
315 of-function) [70]. Cortical neurons cultured from Scn2a$^{+/R102Q}$ mice exhibited a significant
316 attenuation in neural firing activity (~40% decrease at DIV14; $p < 0.001$, Fig. 3D), consistent with
317 a role in autism but not IEE. Next, we analyzed the spatial proteome of these mutants versus WT
318 mice using fractionation steps of whole brain tissue adapted from the Localisation of Organelle
319 Proteins by Isotope Tagging after Differential ultraCentrifugation (LOPIT-DC) procedure [30], as
320 we have published previously [71]. Interestingly, we identified a down-regulation of a protein cluster
321 associated with voltage-gated sodium channel (VGSC) activity in Scn2a$^{+/R102Q}$ mice. This VGSC
322 modulatory cluster included candidates intersecting with the Scn2a HiUGE-iBioID interactome:
323 an auxiliary β subunit, Scn1b [72], and an intracellular VGSC modulator, Fgf12 [73] (Fig. 3C; Table
324 S4).
325
326 Based on the finding of the downregulated VGSC modulatory cluster, a rescue strategy to restore
327 the electrophysiological deficits in Scn2a$^{+/R102Q}$ neurons was devised. First, lentiviral-mediated
328 CRISPR-activation (CRISPRa) was used to upregulate endogenous Scn2a expression (Fig. S8A).
329 A similar strategy has recently been used to phenotypically rescue Scn2a haploinsufficiency [74];
330 however, it has not yet been tested in neurons harboring patient-derived missense mutations. This
331 treatment transcriptionally activates Scn2a expression; however, it is expected to amplify both the
332 WT and mutant allele. RT-PCR data from WT and Scn2a$^{+/R102Q}$ neurons showed normal transcript
333 levels (Fig. S8B), suggesting the reduced protein levels in the mutant were likely due to post-
334 transcriptional effects such as protein destabilization. Thus, it was unclear if Scn2a-CRISPRa
335 alone would fully rescue phenotypes, as the effect potentially could be diluted by the mutant allele.
336 Indeed, CRISPRa treatment only partially rescued the Scn2a$^{+/R102Q}$ phenotype (Fig. 3D, purple
337 bars), suggesting this approach is unlikely to work in the context of missense mutations. A
338 treatment strategy was next tested by supplying either additional SCN1B or FGF12 via AAV-
339 mediated expression to augment these down-regulated intersecting proteins identified in the VGSC
340 modulatory cluster. MEA analysis revealed that neither expressing SCN1B or FGF12 alone, or

341 when added together, was sufficient to rescue the phenotype (Fig S8C). Finally, a combinatory
342 ("combo") approach was tested, combining the upregulation of all three of the depleted VGSC
343 cluster proteins. This combo approach resulted in a full restoration of neural firing activity metrics
344 at DIV14 (Fig. 3D, S8D), suggesting the potential dominant-negative effect of the mutation in
345 Scn2a-CRISPRa was overcome by the increased expression of SCN1B and FGF12; thereby
346 confirming the hypothesis that this modulatory cluster is crucial for the phenotypic rescue of
347 $Scn2a^{+/R102Q}$. Collectively, these results strongly indicate that intersectional proteomics between
348 HiUGE-iBioID and spatial co-perturbation can be an informative approach to discover novel
349 approaches for the functional rescue of abnormal phenotypes and potential therapeutic targets.
350
351 **Discussion**
352
353 Here we report a strategy combining the advantages of HiUGE and iBioID to resolve native
354 interactomes associated with 14 autism-associated proteins. The combination of the interaction
355 data presented for Syngap1 and Anks1b and the Scn2a rescue results validate the HiUGE-iBioID
356 method for discovering the functional links between autism genetics and proteomics. The findings
357 also emphasize an effective proteomic-driven systems-biology approach to discover molecular
358 mechanisms and potential treatment targets.
359
360 Compared to immunoprecipitation or recombinant BioID expression methods *in vitro*, HiUGE-
361 iBioID is expected to have four key benefits. First, the bait protein is expressed from the
362 endogenous promoter with native cell-type specificity preserved at physiological levels. Second,
363 the cells expressing the bait protein are within the context of the tissue, obviating perturbations to
364 their native environment essential for development and cell physiology that can occur *in vitro*.
365 Third, interactomes are covalently marked as they exist *in vivo* and thus, the proteins can be
366 purified subsequently under stringent conditions without the need to optimize samples for weak or
367 transient interactions. This feature is especially important for protein complexes organized by
368 transmembrane baits, which must be extracted from the lipid bi-layer under conditions that are
369 unfavorable for maintaining many PPIs. Fourth, the selection of the bait-protein is not limited by
370 viral packaging capacity or availability of high-specificity and validated antibodies.
371

372 HiUGE-iBioID is a technique that, from a biochemical perspective, combines the strengths of
373 endogenous protein-based purification from tissue that antibodies afford with the advantages of
374 covalent marking of proximity interactomes by BioID. These qualities suggest that HiUGE-iBioID
375 may be an optimal approach. Nevertheless, an essential question is how its interactomes compare
376 with analogous studies using immunoprecipitation or recombinant BioID expression. To address
377 this important issue, we performed a direct comparison of HiUGE-iBioID to antibody
378 immunoprecipitations of Anks1b and Scn2a from mouse brain tissue (Fig. S4 I, J). While there
379 was a significant overlap in the interactomes between HiUGE-iBioID and each immunoaffinity
380 pulldown, the differences between them were even greater (Fig. S4 K, L). For example,
381 immunoprecipitation of the voltage-gated sodium channel, Scn2a, identified the expected proteins
382 that overlap with HiUGE-iBioID, including clusters of Na^+ / K^+ channels and Fgf12, consistent
383 with previous reports [28,75]. However, GO analysis of the fraction that did not overlap with HiUGE-
384 iBioID yielded top-ranked molecular function terms of "structural constituent of the ribosome"
385 and multiple RNA processes. In contrast, the fraction unique to HiUGE-iBioID were enriched
386 correctly for top GO terms of voltage-gated ion channel functions. Similar conclusions were noted
387 from the comparison of HiUGE-iBioID to the recent publication of immunoprecipitation-based
388 interactomes of Syngap1, Shank3, Scn2a, and Ctnnb1 [28] (Fig. S9). We also compared recently
389 published data of recombinant bait-BioID expression in cultured mouse neurons to HiUGE-iBioID
390 for the baits Syngap1, Shank3, and Lrrc4c that were shared between both studies [27] (Fig. S10).
391 While the BioID and HiUGE-iBioID interactomes had more in common with each other than the
392 analogous immunoprecipitation comparisons, there were again more differences between the
393 interactomes than there were similarities. While HiUGE-iBioID specific interactomes for each had
394 the top GO term "Glutamate receptor binding" for all three synaptic baits, the recombinant BioID
395 specific data were enriched for top GO terms such as "Tubulin binding", "RNA binding", "Heat
396 shock protein binding", and "Acidic amino acid transmembrane transporter activity". While
397 further comparisons are needed to confirm the above observations, the available data suggest that
398 endogenous proximity proteomics outperforms both immunoprecipitation and recombinant BioID
399 methods *in vitro*. Employing HiUGE-iBioID for the *in vivo* study of endogenous protein
400 complexes appears to be an advantageous method overall.
401

402 Consistent with the observation that HiUGE-iBioID performs well, each interactome revealed the
403 expected, as well as new potential biological insights following further analysis with MCL to
404 partition biologically-relevant communities (Fig. S11-24). For example, neurobeachin (Nbea) (Fig.
405 S16) is known to regulate the surface levels of ionotropic GABA and glutamate receptors as well
406 serve as an A-Kinase (PKA) Anchoring Protein (AKAP) [76-79]. HiUGE-iBioID revealed that both
407 the regulatory and catalytic subunits of PKA were detected. Clusters of the relevant receptors with
408 significant enrichment for "GABA signaling pathway", "Ionotropic glutamate receptor signaling",
409 and "Regulation of AMPA receptor activity" were also found, consistent with Nbea's known
410 functions. Of note, the "GABA signaling pathway" cluster was also significantly enriched for the
411 terms "autism spectrum disorder" and "epilepsy", both to which Nbea is implicated [80,81].
412 Interestingly, GABA and glutamate surface levels are thought to be modulated by distinct
413 pathways influenced by Nbea [82]. Consistent with this idea, clusters enriched for "AP-type
414 membrane coat adaptor complex", "COPI vesicle coat", and "TRAPP complex" were discovered,
415 suggesting these may be the trafficking processes that Nbea modulates. Moreover, the analysis
416 suggests Nbea may influence other signaling pathways that have yet to be appreciated, including
417 "G-protein-coupled GABA receptors" and "Voltage-gated potassium channel complexes",
418 although additional experimental analyses will be needed to test these new interactome-derived
419 hypotheses.
420
421 In addition to specificity advantages, HiUGE-iBioID is easily scalable in terms of time and
422 resources when compared to the alternative of the traditional transgenic animal approaches to
423 generate endogenous protein fusions *in vivo*. We have found that forebrain tissue collected from
424 as few as two mice is sufficient for one biological replicate. Therefore, a typical mouse litter (~ 8
425 pups) is sufficient to analyze a bait interactome in biological triplicates. We anticipate this method
426 can be optimized even further for larger-scale applications, where costs can be limiting. These
427 approaches could include multiplexed mass-spectrometry techniques such as isobaric labeling [83,84],
428 or new advancements in mass spectrometry scan rates that reduce instrument time.
429
430 We also recognize a few limitations of our method. First, the proximity proteomes reported here
431 are based on an enrichment with the bait over negative control, thus it is possible some proteins
432 are present yet not identified as significantly enriched [85]. Second, since the fusion proteins are

433 expressed at an endogenous level, efficient biotinylation may be challenging for some low-
434 expression proteins. Third, common to all protein fusion strategies, it is unrealistic to guarantee
435 that the tag does not alter any interaction. The ability to generate fusion proteins by inserting
436 TurboID directly into coding exons, or by splicing TurboID in from introns for proteins that cannot
437 be altered at their N- or C-termini, provides flexible gRNA selection as well as protein engineering
438 design. We envision further developments to our approach will include adapting *in silico* structure
439 prediction tools (e.g. AlphaFold [86] and ESMFold [87]) to minimize potential disturbances by
440 structure-based optimization of TurboID fusions. Additionally, rapid advancements in the
441 sensitivity of mass-spectrometry [88-90] promise to enable further HiUGE-iBioID analysis, even for
442 low-level proteins.
443
444 A crucial finding from the current HiUGE-iBioID application is that diverse autism genes
445 physically form protein interaction networks with each other and can be co-perturbed in genetic
446 models of autism. This result confirms that divergent genetic mutations can converge at the protein
447 level to drive autism neurobiology, providing a working paradigm to prioritize co-regulated
448 candidates in physiology and atypical brain development. Furthermore, we demonstrate that high-
449 confidence autism genes interact with other lower-confidence autism genes at the proteome level.
450 Indeed, three proteins detected in the interactome dataset (Itsn1, associated with Scn2a, Scn8a,
451 Ank3, and Shank3 baits; Nav3, associated with Scn2a bait; and Hnrnpul2, associated with Hnrnpu
452 bait) were discovered subsequently as new autism risk genes of genome-wide significance [38]
453 during the preparation of this manuscript. These results emphasize the possibility that additional
454 genes - whose significance in autism are as yet unknown - exist in the dataset. Thus, HiUGE-
455 iBioID may be useful to prioritize lower-confidence autism genes, which could either play a role
456 in regulating core autism drivers or serve as novel targets for pharmacological developments. In
457 addition, we expect the endogenous autism interactome data will stimulate a new impetus for
458 predictive modeling of autism genetics [91,92] and cell-type specific analyses harnessing single-cell
459 proteomics [93-95].
460
461 Informed by the autism interactome and proteomic co-perturbation results, we focused on a tightly
462 co-regulated pair, Syngap1 and Anks1b [27,46-48], and verified the functional significance of their
463 interaction. We identified a putative internal region on Syngap1 that is crucial for interaction with

464 Anks1b, and confirmed that Syngap1 truncation led to remodeling of its interactome, including a
465 loss of interaction with Anks1b. The data support the notion that remodeling of synaptic protein
466 complexes, such as previously reported PDZ-associated alterations [62] and the disruption of
467 specific interactions like Syngap1-Anks1b, could be possible mechanisms relevant to Syngap1
468 synaptopathy beyond nonsense-mediated decay [50]. Further, we identified several neomorphic
469 proteomic interactions associated with the Syngap1 truncation (Fig. 2G). The mechanisms of
470 whether or how these abnormal interactions might contribute to Syngap1-associated phenotypes
471 remain to be carefully assessed, and cannot be easily extrapolated to patients. The additive effects
472 of Syngap1 and Anks1b deficits seen in the aberrant neural activity indicate that the
473 downregulation of Anks1b in Syngap1-Het mice is not a compensatory effect, but rather it may
474 contribute to a mechanism that alters neuronal development. The disordered region of Syngap1,
475 identified as a critical domain mediating binding with Anks1b, contains proline-rich stretches, a
476 poly-histidine motif, and is phosphorylated at multiple sites [96,97]. This architecture suggests their
477 interaction could be under activity-dependent kinase modulation. Accordingly, within the Anks1b-
478 Syngap1 core interactome, there are 12 kinases / phosphatases, 4 of which are likely autism risk
479 genes themselves (Pak2, Cdkl5, Ntrk3, Dyrk1a) [2]. Thus, an intriguing speculation is that these
480 gene products may play a role in regulating synaptogenesis via acting on the Syngap1/Anks1b
481 complex, and contributing to the activity-dependent shuttling of Syngap1/Anks1b during
482 plasticity.
483
484 A notable finding of this study is the discovery of a mechanism for restoring *in vitro* neural activity
485 deficits associated with a patient-derived SCN2A-p.R102Q mutation. We have identified three
486 proteins (Scn2a, Scn1b, and Fgf12) within the VGSC complex that are critical for phenotypic
487 rescue by intersecting the Scn2a HiUGE-iBioID interactome with co-perturbation spatial-
488 proteomics in a mouse model harboring this mutation. A qPCR analysis revealed that the
489 abundances of Scn2a, Scn1b, and Fgf12 mRNAs in cultured $Scn2a^{+/R102Q}$ neurons are comparable
490 to the WT (Fig. S8B), suggesting the downregulation of these proteins occurs at the post-
491 transcriptional level - likely due to destabilization of VGSC supramolecular assembly. The exact
492 mechanisms as to how the loss of a positively charged arginine residue on the N-term intracellular
493 tail of Scn2a affects VGSC assembly remains to be determined. Similarly, the effects of these

494 perturbations need to be assessed further as some alterations may be benign with respect to
495 phenotypes.
496
497 Both β-subunits and FGF family proteins play critical roles in maintaining neuronal excitability
498 through regulating VGSC kinetics [72,98]. Thus, their downregulation in Scn2a$^{+/R102Q}$ is likely a
499 contributing factor to VGSC channelopathy. These results also explain why Scn2a-CRISPRa
500 treatment alone is insufficient to rescue the electrophysiological deficits, especially since the
501 treatment does not differentiate the functional allele from the point-mutant allele [74]. We further
502 show that supplying additional SCN1B and FGF12 without Scn2a-CRISPRa does not rescue the
503 deficits either (Fig. S8C). Thus, it appears that upregulation of all three components is required to
504 provide the molecular environment necessary to restore functional VGSC complexes and reinstate
505 the level of spontaneous neural activity. The *in vitro* phenotypic rescue presented here will require
506 future testing *in vivo*. Although we did not observe an overt epileptogenic effect on the MEA, these
507 potential adverse effects should be carefully assessed in future animal studies. In addition, since
508 VGSCs are believed to contribute to neuronal excitability and plasticity at both pre- and post-
509 synapses [65,99], future studies are needed to further dissect their unique subcellular effects.
510
511 Together, our results show that HiUGE-iBioID provides a new CRISPR/proximity proteomics
512 method to reveal native proteomes *in vivo* with higher-confidence interactomes than
513 immunoprecipitation or BioID over-expression approaches, and with considerable ease compared
514 to traditional transgenic approaches. Combined with co-perturbation proteomics, our intersectional
515 approach offers a generalizable strategy to identify and prioritize candidates for discovering new
516 biology and potential therapeutic targets. Thus, future work could adopt a similar approach to
517 investigate genetic co-perturbations and PPIs in other models. We expect that the framework
518 developed in this study will encourage further research of native proximity interactomes in the
519 brain, enhancing our understanding of proteome organization in various aspects of cellular
520 neurobiology and disease.
521
522 **Acknowledgments**
523

We would like to thank Drs. Tyler Bradshaw and Jamie Courtland for performing synaptosome and fractionation proteomics, Dr. Ramona M. Rodriguiz, Mr. Christopher R. Means, Mr. Nathan Franklin, and Ms. Sarah Page Steffens for conducting the behavioral experiments, and Dr. Rodriguiz for helping with the behavioral statistical analyses. We would like to thank Arinze Okafor for assistance with the similarity matrix plot, Greg Waitt for developing the DPMSR Proteome Discoverer Data Visualization Tool, and Daniel J. Morone for assistance with lentiviral production and titration. We would also like to thank Dr. Jiechun Zhou for her assistance with mouse husbandry. Schematic illustrations were created using a licensed BioRender.com account.

Funding: Research reported in this publication was supported by a donation to the Duke Center for Autism and Brain Development, NIH R01MH111684 (SHS), UM1HG012053 (CAG), R01MH125236 (CAG), RM1HG011123 (CAG), and in part by the Office of The Director, National Institutes of Health of the National Institutes of Health under Award Number S10OD024999 (M Arthur Moseley). The content is solely the responsibility of the authors and does not necessarily represent the official views of the National Institutes of Health.

Data and Materials Availability: Requests for data, resources, and reagents should be directed to and will be fulfilled by the Corresponding Author, Dr. Scott Soderling (scott.soderling@duke.edu). Key plasmids from this study have also been deposited to Addgene.

Code availability: Requests for custom computer code used in this study should be directed to and will be fulfilled by the Corresponding Author, Dr. Scott Soderling (scott.soderling@duke.edu). Key codes from this study have also been deposited to Github.

Competing interests:

SHS and YG have a patent application related to the HiUGE technology. The intellectual property was licensed to CasTag Biosciences. SHS is a founder of CasTag Biosciences; Duke University as an institution holds equity in CasTag Biosciences. CAG is an inventor on patents and patent applications related to CRISPR-based gene activation, is a co-founder of Tune Therapeutics, Locus Biosciences, and Element Genomics, and is an advisor to Sarepta Therapeutics. GD Dr. Dawson

555 is on the Scientific Advisory Boards of Akili Interactive, Inc, and Tris Pharma, is a consultant to
556 Apple, Gerson Lehrman Group, and Guidepoint Global, Inc. GD has developed autism-related
557 technology, data, and/or products that have been licensed to Apple, Inc. and Cryocell, Inc. and
558 Dawson and Duke University have benefited financially. JDB is a consultant for Bridgebio. WCW
559 is a consultant for Onsero Therapeutics.
560
561 **Author contributions:**
562
563 YG and SHS conceived the study. YG, MT, DS and EJS performed HiUGE-iBioID experiments
564 and analyses. SAGM designed CRISPRa constructs and JZ performed validation experiments. YG
565 and MT performed MEA experiments. WCW designed and managed the behavioral experiments
566 and statistical analyses. GD and YJ contributed to the generation of Scn2a$^{+/R102Q}$ model. DV and
567 LGS performed gene-set analyses. CAG, JDB, and SHS supervised the collaborative study. YG
568 and SHS wrote the original manuscript. All authors contributed to manuscript editing and revision.
569
570 **Materials and Methods**
571
572 **Animals**
573 For all CRISPR-Cas9-related experiments, H11-Cas9 mice (Jackson Laboratory #28239) were
574 used. The Syngap1-Het mouse model, originally described by Kim and colleagues [56], was a gift
575 from Dr. Gavin Rumbaugh. The Scn2a$^{+/R102Q}$ mouse model of the human c.305G>A (p.R102Q)
576 mutation [68,69] was created by the Duke Transgenic and Knockout Mouse Shared Resource. The
577 Scn2a$^{+/R102Q}$ mice were generated using a heterozygous breeding scheme and genotyping was
578 performed by sequencing the amplicon using the following primer set: Scn2a-s,
579 acagacatggcggaaaacatgag; and Scn2a-as, agcaggagaggaaagaaagaagc. C3H/HeJ males (#000659;
580 Jackson Laboratory, Bar Harbor, ME) served as social partners in the resident-intruder and social
581 dyadic tests. All procedures were performed with a protocol approved by the Duke University
582 Institutional Animal Care and Use Committee in accordance with US National Institutes of Health
583 guidelines.
584
585 **Single-vector HiUGE TurboID knock-in**

586

587 HiUGE plasmids were constructed based on the previously described method [31]. Briefly, a donor
588 of HA-tagged TurboID coding sequence was flanked by DNA sequences that were specifically
589 recognized by a synthetic donor-specific gRNA (DS-gRNA), inert to the host genome. The gene-
590 specific gRNA (GS-gRNA) expression cassette (U6 promotor, GS-gRNA, and gRNA scaffold)
591 was inserted in tandem to the DS-gRNA expression cassette permitting a single-vector delivery.
592 GS-gRNAs were designed using CRISPOR [100], and a pair of 23-24mer oligonucleotides were
593 annealed and ligated into the *SapI* site of the GS-gRNA expression cassette. The genomic target
594 sequences for the baits were: Anks1b: cggcgggtatcagaaaatcgtgg, Shank2:
595 aacagctgctggacagataaggg, Shank3: cgtgcgctcaggcagctggatgg, Nckap1: gcatttctcagcaacacataagg,
596 Nbea: ggcattatgagcatcagaacagg, Arhgef9: cattctggcaaaacttcagtagg, Ank3:
597 gaagaaggaaatccggaacgtgg, Scn2a: ggacaaggggaaagatatcaggg, Scn8a: tcagggagtccaagtgctagagg,
598 Hnrnpu: tggagtcagcattatcaccaagg, Homer1: ttagctgcattccagtagcttgg, and Wasf1:
599 gttcgatgaagtagactggctgg. To protect the PDZ-binding motifs of Syngap1, Ctnnb1, and Iqsec2, an
600 intron-targeting strategy [33] was used, where the donor was flanked by intron / exon boundary
601 sequences from an obligatory intron to enable internal TurboID insertion. The following intronic
602 sequences were targeted: Syngap1: acttattgagacgcttcgcgggg, Ctnnb1: aacaggcttccagatgcgatggg,
603 and Iqsec2: agggccaactccaaatagggagg. To insert TurboID while protecting the C-term PDZ-
604 binding motif of Lrrc4c that has only one coding exon, a custom donor was used where the coding
605 sequence of a.a. ETQI was appended to the C-term of the TurboID donor, thus preserving the
606 native motif. The genomic target for Lrrc4c: gagttcattcggatcaataacgg. Exon 13 of Syngap1 was
607 targeted for Syngap1 truncation and disruption: acggactcggtctcagcccatgg. To endogenously
608 express soluble TurboID as a survey for background detection, C-term or 3'-UTR sequences were
609 targeted with a stop codon - internal ribosome entry site (IRES) - TurboID-HA donor. The genomic
610 target sequences were: Syngap1: aggaggtctgtgacgctgggtgg, Scn2a: agtttggcatagacctcctgagg,
611 Hnrnpu: aaacagtcgacttcttgtgaagg, Ctnnb1: ttataagctttcttacctaaagg, Iqsec2:
612 tactggggagcaggatagtctgg, Homer1: ttagctgcattccagtagcttgg, and Wasf1: gttcgatgaagtagactggctgg.
613

614 **AAV preparation**

615

616 AAV was prepared following previously described methods [23,31]. Briefly, concentrated AAV virus
617 was produced in HEK293T cells grown in six 15cm dishes by triple-transfection with 15µg HiUGE
618 vector, 30µg pADdeltaF6, and 15µg serotype plasmid (pUCmini-iCAP-PHP.eB, a gift from
619 Viviana Gradinaru [101], Addgene plasmid #103005). Three days following transfection, cells were
620 lysed and virus was concentrated using an Optiprep density gradient (Sigma #D1556). Small-scale
621 AAV virus was produced in HEK293T cells grown in 12-well plates by triple-transfection with
622 0.4µg HiUGE vector, 0.8µg pADdeltaF6, and 0.4µg serotype 2/1 plasmids. Three days following
623 transfection, the virus-containing medium was filtered through Costar Spin-X columns (Sigma
624 #8162) as previously described [31].
625
626 **AAV injection and biotin injection for HiUGE-iBioID**
627
628 Neonatal (P0-2) H11-Cas9 mice were injected intracranially with the purified AAV (2µL per
629 hemisphere, PHP.eB serotype, > 10^{10} GC / µL titer). Donor vector backbone AAV (empty gRNA)
630 was used as negative control. Approximately 3 weeks after injection, mice received daily
631 intraperitoneal injections (i.p.) of biotin (50mg/kg) over 5 consecutive days. Forebrain tissue was
632 collected one day after the final injection and snap-frozen at -80°C until purification.
633
634 **HiUGE-iBioID sample purification**
635
636 For each replicate, forebrain tissue from two mice was combined, homogenized, sonicated in RIPA
637 lysis buffer (Cell Signaling #9806) supplemented with cOmplete protease inhibitor cocktail
638 (Sigma #11873580001), and centrifuged at 16,000 xg for 30min at 4°C. The supernatant lysate
639 was desalted with Zebra columns 7K MWCO (ThermoFisher #89894 or #89892). The flow-
640 through was combined with 150µL magnetic Strepavidin beads (Pierce #88816) and incubated at
641 4°C overnight. On the next day, the beads were washed with the following steps: RIPA buffer 2
642 times, 1M KCl once, 0.1M Na_2CO_3 once, 2M urea in 10mM Tris-HCl once, and RIPA buffer 2
643 times. Biotinylated proteins were eluted by boiling the beads in 90µL 2X sample buffer,
644 supplemented with 2.5mM biotin, and used for downstream LC-MS/MS and Western blot
645 analyses.
646

647 **HiUGE-iBioID LC-MS/MS analysis**

648

649 Samples were spiked with undigested bovine casein at a total of either 120 or 240 fmol as an
650 internal quality control standard. Next, samples were supplemented with 12.4 µL of 20% SDS,
651 reduced with 10 mM dithiolthreitol for 30 min at 80 °C, alkylated with 20 mM iodoacetamide for
652 30 min at room temperature (RT), then supplemented with a final concentration of 1.2%
653 phosphoric acid and 723 µL of S-Trap (Protifi) binding buffer (90% MeOH/100mM TEAB).
654 Proteins were trapped on the S-Trap micro cartridge, digested using 20 ng/µL sequencing grade
655 trypsin (Promega) for 1 hr at 47 °C, and eluted using 50 mM TEAB, followed by 0.2% FA, and
656 lastly using 50% acetonitrile (ACN) /0.2% FA. All samples were lyophilized to dryness. Samples
657 were resolubilized using 12 µL of 1% TFA/2% ACN with 25 fmol/µL yeast ADH.

658

659 Quantitative LC-MS/MS was performed on 2 µL (~17% of total sample) using a nanoAcquity
660 UPLC system (Waters Corp) coupled to a Thermo Orbitrap Fusion Lumos high resolution accurate
661 mass tandem mass spectrometer (Thermo) equipped with a FAIMSPro device via a
662 nanoelectrospray ionization source. Briefly, the sample was first trapped on a Symmetry C18 20
663 mm × 180 µm trapping column (5 µl/min at 99.9/0.1 v/v water/ACN), after which the analytical
664 separation was performed using a 1.8 µm Acquity HSS T3 C18 75 µm × 250 mm column (Waters
665 Corp.) with a 90-min linear gradient of 5 to 30% ACN with 0.1% formic acid at a flow rate of 400
666 nanoliters/minute (nL/min) with a column temperature of 55°C. Data collection on the Fusion
667 Lumos mass spectrometer was performed for three difference compensation voltages (-40v, -60v,
668 -80v). Within each CV, a data-dependent acquisition (DDA) mode of acquisition with a r=120,000
669 (@ m/z 200) full MS scan from m/z 375 – 1600 with a target AGC value of 4e5 ions was
670 performed. MS/MS scans were acquired in the ion trap in rapid mode with a target AGC value of
671 1e4 and max fill time of 35 msec. The total cycle time for each CV was 0.66s, with total cycle
672 times of 2 sec between like full MS scans. A 20s dynamic exclusion was employed to increase
673 depth of coverage. The total analysis cycle time for each injection was approximately 2 hours.

674

675 Following UPLC-MS/MS analyses, data were imported into Proteome Discoverer 2.5 ("PD",
676 Thermo Scientific Inc.) and individual LCMS data files were aligned based on the accurate mass
677 and retention time of detected precursor ions ("features") using Minora Feature Detector algorithm

678 in Proteome Discoverer. Relative peptide abundance was measured based on peak intensities of
679 selected ion chromatograms of the aligned features across all runs. The MS/MS data was searched
680 against the SwissProt *M. musculus* database and a common contaminant/spiked protein database
681 (bovine albumin, bovine casein, yeast ADH, etc.), and an equal number of reversed- sequence
682 "decoys" for false discovery rate determination. Sequest with Infernys enabled (v 2.5, Thermo PD)
683 was utilized to produce fragment ion spectra and to perform the database searches. Database search
684 parameters included fixed modification on Cys (carbamidomethyl) and variable modification on
685 Met (oxidation). Search tolerances were 2ppm precursor and 0.8Da product ion with full trypsin
686 enzyme rules. Peptide Validator and Protein FDR Validator nodes in Proteome Discoverer were
687 used to annotate the data at a maximum 1% protein false discovery rate based on q-value
688 calculations. Note that peptide homology was addressed using razor rules in which a peptide
689 matched to multiple different proteins was exclusively assigned to the protein has more identified
690 peptides. Protein homology was addressed by grouping proteins that had the same set of peptides
691 to account for their identification. A master protein within a group was assigned based on %
692 coverage.
693
694 Prior to imputation, a filter was applied such that a peptide was removed if it was not measured in
695 at least 2 unique samples (50% of a single group). After filtration, any missing data missing values
696 were imputed using the following rules; 1) if only a single signal was missing within the group of
697 three, an average of the other two values was used or 2) if two out of three signals were missing
698 within the group of three, a randomized intensity within the bottom 2% of the detectable signals
699 was used. To summarize to the protein level, all peptides belonging to the same protein were
700 summed into a single intensity. This protein value was then subjected to a robust mean
701 normalization in which the top and bottom 10 of the signals were removed and then the remaining
702 mean was made to be the same across all samples.
703
704 The results were log2-transformed and analyzed using the PolySTest online tool [102]. Proteomic
705 detection was defined as proteins identified by at least 2 peptides in LC-MS/MS. Protein
706 abundances were considered significantly enriched if they met FDR < 0.05 (PolySTest), and fold
707 change ≥ 2 (Log2-FC ≥ 1) compared to controls. The enriched gene lists were filtered against
708 known experimental and omnipresent biological contaminants, and soluble TurboID background

709 detections. Note that this high-stringency filter removed a few well-known interactors such as
710 Dlg4, Shank2, and Shank3 from the dataset of several baits.
711
712 **Synaptosomal preparation and proteomic analysis of Syngap1-Het mice.**
713
714 Synaptosomal preparation was performed with four adult Syngap1-Het mice and four WT controls.
715 Briefly, rapidly isolated brain tissue was sliced to 1mm sections using a brain matrix (Zivic
716 Instruments), followed by dissection of cortical and striatal tissue. Tissue was homogenized in
717 homogenization buffer (320 mM sucrose, 5 mM HEPES, pH 7.4) using a Dounce homogenizer.
718 The lysate was centrifuged at 1,000 xg to remove cell debris and nuclei. The supernatant was
719 further centrifuged at 12,000 xg to obtain a crude synaptosomal pellet and it was resuspended in
720 Tris buffer (320 mM sucrose, 5 mM Tris/HCl, pH 8.1). Additional centrifugation in a sucrose
721 density gradient (0.8/1.0/1.2 M) at 85,000 xg was performed to isolate purified synaptosome at the
722 1.0/1.2 interface. The purified synaptosomes were subjected to multiplexed LC-MS/MS
723 quantification following tandem mass tags (TMT) isobaric labeling.
724
725 **LOPIT-DC subcellular fractionation and proteomic analysis of Scn2a$^{+/R102Q}$ mice.**
726
727 LOPIT-DC fractionation was performed with three adult Scn2a$^{+/R102Q}$ mice and three WT controls,
728 following a previously described method [30,71,103]. Briefly, rapidly isolated brain tissue was added
729 to isotonic TEVP homogenization buffer (320 mM sucrose, 10 mM Tris, 1 mM EDTA, 1 mM
730 EGTA, 5 mM NaF, pH7.4), supplemented with cOmplete protease inhibitor cocktail (Sigma
731 #11873580001). The tissue was homogenized for 15 passes in a 2mL Dounce homogenizer. The
732 volume of the homogenate was brought up to a 5 mL volume with TEVP buffer, and then passed
733 through a 0.5 mL ball-bearing homogenizer for two passes (14 µm ball, Isobiotec). Differential
734 centrifugation steps were performed at 4°C sequentially at 200, 1000, 3000, 5000, 9000, 12,000,
735 15,000, 30,000, 79,000, and 120,000 xg. Fraction-5, determined to be enriched with Scn2a in a
736 pilot experiment [71], was used for tandem mass tag (TMT)-multiplexed proteomic analysis.
737
738 **TMT-multiplexed quantitative LC-MS/MS analysis.**
739

740 Samples were supplemented with 100 µL of 8 M urea and probe sonicated. Protein concentrations
741 were determined via Bradford Assay and ranged from 1.8 – 2.3 mg/mL. Samples were normalized
742 to 120 µg using 8 M urea and spiked with undigested bovine casein at a total of either 120 or 240
743 fmol as an internal quality control standard. Next, they were supplemented with 13 µL of 20%
744 SDS, reduced with 10 mM dithiolthreitol for 45 min at 32 °C, alkylated with 20 mM iodoacetamide
745 for 45 min at RT, then supplemented with a final concentration of 1.2% phosphoric acid and 70
746 µL of S-Trap (Protifi) binding buffer (90% MeOH/100mM TEAB). Proteins were trapped on the
747 S-Trap micro cartridge, digested using 100 ng/µL sequencing grade trypsin (Promega) for 1 hr at
748 47 °C, and eluted using 50 mM TEAB, followed by 0.2% FA, and lastly using 50% CAN/0.2%
749 FA. All samples were then lyophilized to dryness.
750
751 For TMT labeling, each sample was resuspended in 120 µL 200 mM triethylammonium
752 bicarbonate, pH 8.0 (TEAB). 40uL of each sample was combined to form an SPQC pool, which
753 was then aliquoted into 3 SPQC pools. Fresh TMT10plex reagents (0.8 mg for each 10-plex
754 reagent) were resuspended in 41 µL 100% ACN and was added to 75 µg of each sample. Samples
755 were incubated for 1 hour at RT. After 1-hour reaction, 8 µL of 5% hydroxylamine was added and
756 incubated for 15 minutes at RT to quench the reaction. Samples were combined then lyophilized
757 to dryness.
758
759 For offline fractionation, samples were resuspended in 300uL 0.1% formic acid. 400µg was
760 fractionated into 48 unique high pH reversed-phase fractions using pH 9.0 20 mM ammonium
761 formate as mobile phase A and neat ACN as mobile phase B. The column used was a 2.1 mm x
762 50 mm BEH C18 (Waters) and fractionation was performed on an Agilent 1100 HPLC with
763 G1364C fraction collector. Throughout the method, the flow rate was 0.4 mL/min and the column
764 temperature was 55 °C. The gradient method was set as follows: 0 min, 3%B; 1 min, 7% B; 50
765 min, 50%B; 51 min, 90% B; 55 min, 90% B; 56 min, 3% B; 70 min, 3% B. Forty-eight fractions
766 were collected in equal time segments from 0 to 52 minutes, then concatenated into 12 unique
767 samples using every 12th fraction. For instance, fraction 1, 13, 25, and 37 were combined, fraction
768 2, 14, 26, and 38 were combined, etc. Fractions were frozen and lyophilized overnight. Samples
769 were resuspended in 50 µL 1%TFA/2% ACN prior to LC-MS analysis.
770

771 Quantitative LC-MS/MS was performed on 2 µL (1 µg) of each sample, using a nanoAcquity
772 UPLC system (Waters Corp) coupled to a Thermo Orbitrap Fusion Lumos high resolution accurate
773 mass tandem mass spectrometer (Thermo) equipped with a FAIMSPro device via a
774 nanoelectrospray ionization source. Briefly, the sample was first trapped on a Symmetry C18 20
775 mm × 180 µm trapping column (5 µl/min at 99.9/0.1 v/v water/ACN), after which the analytical
776 separation was performed using a 1.8 µm Acquity HSS T3 C18 75 µm × 250 mm column (Waters
777 Corp.) with a 90-min linear gradient of 5 to 30% ACN with 0.1% formic acid at a flow rate of 400
778 nanoliters/minute (nL/min) with a column temperature of 55°C. Data collection on the Fusion
779 Lumos mass spectrometer was performed for three difference compensation voltages (-40v, -60v,
780 -80v). Within each CV, a data-dependent acquisition (DDA) mode of acquisition with a r=120,000
781 (@ m/z 200) full MS scan from m/z 375 – 1600 with a target AGC value of 4e5 ions was
782 performed. MS/MS scans were acquired in the Orbitrap at r=50,000 (@ m/z 200) from m/z 100
783 with a target AGC value of 1e5 and max fill time of 105 msec. The total cycle time for each CV
784 was 1s, with total cycle times of 3 sec between like full MS scans. A 45 sec dynamic exclusion
785 was employed to increase depth of coverage. The total analysis cycle time for each sample
786 injection was approximately 2 hr.
787
788 Data were imported into Proteome Discoverer 2.4 (Thermo Scientific Inc.) and individual LCMS
789 data files were aligned based on the accurate mass and retention time of detected precursor ions
790 ("features") using Minora Feature Detector algorithm in Proteome Discoverer. Relative peptide
791 abundance was measured based on peak intensities of selected ion chromatograms of the aligned
792 features across all runs. The MS/MS data was searched against the SwissProt M. musculus
793 database (downloaded in Nov 2019), a common contaminant/spiked protein database (bovine
794 albumin, bovine casein, yeast ADH, etc.), and an equal number of reversed- sequence "decoys"
795 for false discovery rate determination. Mascot Distiller and Mascot Server (v 2.5, Matrix Sciences)
796 were utilized to produce fragment ion spectra and to perform the database searches. Database
797 search parameters included fixed modification on Cys (carbamidomethyl) and variable
798 modification on Met (oxidation), Asn/Gln (deamindation), Lys (TMT6plex) and peptide N-termini
799 (TMT6plex). Peptide Validator and Protein FDR Validator nodes in Proteome Discoverer were
800 used to annotate the data at a maximum 1% protein false discovery rate based on q-value
801 calculations. Note that peptide homology was addressed using razor rules in which a peptide

802 matched to multiple different proteins was exclusively assigned to the protein has more identified
803 peptides. Protein homology was addressed by grouping proteins that had the same set of peptides
804 to account for their identification. A master protein within a group was assigned based on percent
805 coverage. To account for any missing data (from a misalignment, low quality peak, low signal to
806 noise, etc.) missing values were imputed by using a randomized intensity within the bottom 2% of
807 the detectable signals. The data was then intensity normalized using a trim-mean normalization in
808 which the highest and lowest 10% of the signals from each sample was excluded and then the
809 remaining average intensities of the proteins was made equal across all of the samples.
810
811 The results were then analyzed using the Duke Proteomics and Metabolomics Shared Resource
812 (DPMSR) Proteome Discoverer Data Visualization Tool. Proteomic detection was defined as
813 proteins identified by at least 2 peptides in LC-MS/MS following a 1% FDR correction. Protein
814 abundance was considered significantly altered if they met p-value < 0.05 (two-tailed t-test), and
815 abs(fold change) ≥ 1.2 (abs(Log2-FC) ≥ 0.263). Those with p-value < 0.1 and abs(fold change) $\geq$
816 1.2 (abs(Log2-FC) ≥ 0.263) were considered indicative candidates.
817
818 **Protein network visualization**
819
820 Protein networks were constructed using Cytoscape [104] with nodes representing enriched or
821 dysregulated proteins identified by LC-MS/MS. Known interactions with high confidence (i.e.,
822 0.7 score) between these nodes were queried from the full STRING database (https://string-db.org)
823 [34,35] and plotted on the network figure. To assess the percentage of interactions not reported in
824 STRING queries, a low confidence (0.15) threshold was used. The Markov Cluster Algorithm in
825 STRING and gene ontology (GO) analysis were used to detect protein communities within each
826 interactome, with additional adjustments made based on known protein functions.
827
828 **Gene set enrichment analyses**
829
830 Gene ontology (GO) enrichment of interactomes was searched against a custom statistical domain
831 of all identified brain proteins (9,686 unique proteins, Table S5) from cumulative mouse brain
832 proteomic studies in our lab (n=107), using ShinyGO [105]. Pathway size boundary was set at

833 between 10 and 500 to exclude ambiguous terms for querying the Molecular Function pathway
834 database. Default pathway size boundary was used for all other queries. Redundancy removal
835 option was enabled. SynGO function analyses [106] were also conducted with the synaptic bait
836 proteomes versus the nucleus Hnrnpu proteome as control. Overlaps of identified interactors with
837 the SFARI gene list (2022 Q1 release) were calculated using Venny (Oliveros, J.C. (2007-2015)
838 Venny. An interactive tool for comparing lists with Venn's diagrams.
839 https://bioinfogp.cnb.csic.es/tools/venny/index.html). Hypergeometric tests were performed using
840 an online tool (http://www.nemates.org/MA/progs/overlap_stats.html). In addition, we mapped
841 autism risk genes identified at FDR < 0.1 (102 genes) in Satterstrom et al., 2020 [3] and FDR < 0.05
842 (185 genes) in Fu et al., 2022 [7] to mouse orthologs, and examined their overlap with each set of
843 proteins obtained from the 14 HiUGE-iBioID experiments, via hypergeometric testing (Github
844 Link: git@github.com:lauragails/gene_baiting.git). Bonferroni adjustments were performed and
845 thresholds for statistical significance were delineated on the graphs. We also performed an
846 enrichment analysis between our bait proteomes and the Grove et al., 2019 autism genome-wide
847 association meta-analysis study [44] with MAGMA, as described [107]. Mouse genes in each proximity
848 network were mapped to human entrez gene IDs when possible, using HGNC gene nomenclature
849 (https://www.genenames.org/, Downloaded 06/06/2023).
850
851 For cell-type specific representations, the list of genes for each bait were intersected with mouse
852 orthologs of cell type-specific differentially expressed genes (DEGs) from a single-cell genomics
853 study of post-mortem cortical brain tissues from autistic individuals [8]. We used genes expressed
854 in each cell type as the background to perform the hypergeometic test for overlap between each
855 bait gene list and a list of autism DEGs in each cell type.
856
857 To compare HiUGE-iBioID datasets against immunoprecipitation results from brain lysate, or with
858 recently published autism proteomic interaction datasets [27,28], GO analyses were conducted using
859 input gene lists unique to each set with ShinyGO. Bait self-identifications were excluded from
860 analyses across studies. Gene names were converted to mouse orthologs if applicable. For analyses
861 that lack a consensus statistical domain, mouse genome was used as a non-biased background.
862
863 **Western blot**

For Western blot analyses, 10µL of HiUGE-iBioID purified samples were subjected to SDS-PAGE. After transferring to nitrocellulose membranes, the blot was probed for HA-epitope (rabbit anti-HA, Cell Signaling #3724, 1:1000; or rat anti-HA, Sigma #11867423001, 1:1000), or PSD95 (mouse anti-PSD95, Abcam #ab2723, 1:1000) at 4°C overnight. Equal amounts of input protein from mouse brain lysate were also subjected to SDS-PAGE, and the blot was probed for GAPDH (rabbit anti-GAPDH, Abcam #ab9485 or Cell Signaling #2118, 1:1000) at 4°C overnight. Matching IRDye secondary antibodies (LI-COR, 1:10,000) were incubated with the blot for 1 hr at RT, and the immunosignal was detected using Odyssey FC imager (LI-COR).

Immunocytochemistry and immunohistochemistry

Cells were fixed with 4% PFA and 4% sucrose on DIV 14, then blocked with blocking buffer (Abcam #ab126587, 1:10 in PBS with 0.3% Triton-X). Immunocytochemistry was performed by incubating with primary antibody overnight at 4°C, and with secondary antibody for 1 hr at RT. Antibodies and dilutions consisted of: mouse anti-V5-epitope (ThermoFisher #R960-25, 1:500), rabbit anti-V5-epitope (Cell Signaling #13202S, 1:1000), guinea pig anti-Homer1 (Synaptic Systems #160004, 1:2000), rabbit anti-Syngap1 (ThermoFisher #PA5-58362, 1:1000), rabbit anti-Shank2 (Cell signaling #12218S, 1:1000), mouse anti-Ank3 (ThermoFisher #33-8800, 1:1000), mouse anti-Scn2a (Antibodiesinc #75-024, 1:1000), goat anti-mouse Alexa Fluor Plus 594 (ThermoFisher #A32742, 1:1000), goat anti-guinea pig Alexa Fluor 488 (ThermoFisher #A11073, 1:1000), and goat anti-rabbit Alexa Fluor 488 (ThermoFisher #A11008, 1:1000). Cells were counterstained with 4′,6-diamidino-2-phenylindole (DAPI), mounted with FluorSave reagent (Millipore Sigma #345789), cover-slipped, and imaged on Zeiss Axio Imager M2 with Apotome module or Zeiss LSM 710 confocal microscope. For immunohistochemistry, brains were collected after intracardiac perfusion with ice cold saline and 4% PFA, cryoprotected in 30% sucrose solution, and sectioned at 40µm. Sections were blocked with blocking buffer and incubated with Alexa Fluor 594 or 568-conjugated streptavidin (ThermoFisher #S32356 or #S11226, 1:1000) overnight at 4°C. After washes, sections were counterstained with DAPI and cover-slipped for imaging on Zeiss Axio Imager M2 with Apotome module or Zeiss LSM 710 confocal microscope. Images were processed using Fiji [108].

895

896 **Immunoprecipitation**

897

898 Expression vectors of Myc-DDK-tagged human ORF clones of ANKS1B and SYNGAP1 were
899 purchased from Origene (#RC211877, #RC229432). V5-epitope or GFP-tagged mutants were
900 cloned into the same expression backbone. Truncations of Syngap1 consisted of the following: N-
901 Trunc: Δ a.a. 2-361; C1-Trunc: Δ a.a.730-1343; C2-Trunc: Δ a.a. 848-1343; C3-Trunc: Δ a.a.
902 1181-1343. Mutation of Syngap1 (SYNGAP1-c.2214_2217del) was introduced by site-directed
903 mutagenesis (QuikChange Lightning, Agilent #210518). HEK293T cells were co-transfected with
904 expression vectors using Lipofectamin 3000 (ThermoFisher). Four days following transfection,
905 cells were lysed for Nanobody Trap experiments following the manufacturer's protocol
906 (Chromotek #gta-20, #gtma-20, or #v5tma-20). The bound proteins were eluted by boiling in 2X
907 Western sample buffer and subjected to SDS-PAGE (immunoprecipitated IP fraction). The
908 membrane was probed for Myc-epitope (Santa Cruz #sc-40, 1:250), V5-epitope (Cell Signaling
909 #13202S, 1:1000), or GFP (Cell Signaling #2956S, 1:2000). The lysate was also subjected to SDS-
910 PAGE (input fraction). Here, the membrane was probed for Myc-epitope (Santa Cruz #sc-40,
911 1:250) and GAPDH (Abcam #ab9485 or Cell Signaling #2118, 1:1000). Matching IRDye
912 secondary antibodies (LI-COR, 1:10,000) were used to visualize immuno-signals on an Odyssey
913 FC imager.

914

915 For immunoprecipitation from brain lysate, forebrain tissues were homogenized in T-PER protein
916 extraction reagent (ThermoFisher #78510), cleared by centrifugation following the manufacturer's
917 instruction, and equally divided into replicates. The following antibodies were added to the lysate
918 at a final concentration of 10 ug/mL: mouse anti-Anks1b (Santa Cruz #sc-376610), mouse anti-
919 Scn2a (Antibodiesinc #75-024), or mouse control IgG (Vector labs #I-2000-1) and incubated
920 overnight on a rotator. The next day, 25uL Pierce Protein A/G magnetic beads (ThermoFisher
921 #88802) were added to each immunoprecipitation replicates and incubated for 1 hr under RT.
922 Beads were washed in wash buffer containing 150mM NaCl and boiled in 2X sample buffer to
923 elute the precipitated complexes for label-free LC-MS/MS analysis. Peptide signals were subjected
924 to trimmed-mean normalization and summed on the protein level. Single-peptide detections and
925 contaminants such as mouse IgG were excluded from the analysis. Enrichment was defined as

926 Log2-FC ≥ 1 and *p*-value < 0.05 using the Duke Proteomics and Metabolomics Shared Resource
927 (DPMSR) Proteome Discoverer Data Visualization Tool.
928
929 **AAV / Cas9-mediated expression disruption**
930
931 To disrupt Syngap1 and Anks1b expression, the following genomic sequences were targeted by
932 gRNAs using AAV: Syngap1: acggactcggtctcagcccatgg; Anks1b: attgtcccactgtttggacaggg. AAVs
933 (PHP.eB serotype) were applied to H11-Cas9 primary neuronal cultures, with empty gRNA virus
934 serving as negative control. Effective disruption of Syngap1 and Anks1b expression was
935 confirmed by Western blot (Syngap1: Sigma #SAB2501893 or ThermoFisher #PA5-58362,
936 1:1000; Anks1b: ThermoFisher #PA5-98554, 1:1000).
937
938 **Lentiviral-mediated Scn2a CRISPRa**
939
940 The all-in-one gRNA-Cas9 expression plasmid used for CRISPRa was generated by modifying
941 the hUBC-dSpCas9-2xVP64-T2A-BSD plasmid (Addgene #162333) to remove the T2A-BSD
942 selection marker and include a U6-gRNA scaffold. The non-targeting control gRNA and the
943 gRNAs targeting the *Scn2a* promoter were selected from the Caprano Mouse CRISPR Activation
944 Pooled Library [109] (No_current_500 (non-targeting scramble): tttttagacctaattcgcgc;
945 Scn2a_gRNA1: cagcgattccacttgtggcc; Scn2a_gRNA2: gttgaatgttgctttgccaa; and Scn2a_gRNA3:
946 aattacagcgattccacttg). Individual gRNAs were purchased as oligonucleotides (Integrated DNA
947 Technologies) and cloned into the gRNA expression plasmids using BsmBI sites.
948
949 HEK293T cells were acquired from the American Tissue Collection Center (ATCC). The cells
950 were maintained in DMEM high glucose supplemented with 10% FBS and 1x GlutaMAX
951 Supplement (Gibco #35050061) and cultured at 37°C with 5% CO_2. Lentivirus was produced as
952 previously described [110]: 16 hr before transfection, $7x10^6$ cells were plated in 12ml of transfection
953 media (Opti-MEM I Reduced Serum Medium (Gibco #31985070), 1x GlutaMAX Supplement,
954 5% FBS, 1mM sodium pyruvate (Gibco #11360070), 1x MEM NEAA (Gibco #11140050) in a
955 10cm plate. On the day of transfection, 6mL of transfection media were removed, and the cells
956 were transfected with Lipofectamine 3000 (Invitrogen #L3000008) and 5.4μg pMD2.G (Addgene

957 #12259), 9.9µg psPAX2 (Addgene #12260), and 12µg of the expression vector, according to the
958 manufacturer's instructions. The medium was exchanged with transfection media 6hr after
959 transfection, and the viral supernatant was harvested 24 and 48 hrs after this medium change. The
960 viral supernatant was pooled and passed through a PVDF 0.45 µm filter (Millipore
961 #SLHV033RB), and concentrated to 50x in 1xPBS using Lenti-X Concentrator (Clontech
962 #631232) in accordance with the manufacturer's protocol. The lentivirus was titered by qPCR as
963 previously described [111]. The concentrated lentivirus was snap-frozen and stored at -80°C as
964 single-use aliquots.
965
966 To assess the effect of CRISPRa transcriptional activation, cultured neurons were treated with
967 Scn2a-CRISPRa or non-targeting control lentiviral vectors at DIV0. On DIV11, the cDNA was
968 prepared using Cells-to-cDNA kit (ThermoFisher #AM1723) following the manufacturer's
969 instructions. Predesigned KiCqStart SYBR green primers (Sigma #KSPQ12012) targeting mouse
970 Scn2a and Actb were used for qPCR experiments with PowerUp SYBR green master mix
971 (ThermoFisher #A25742). Specific on-target amplifications were confirmed by gel electrophoresis
972 and TOPO sequencing of the PCR products (ThermoFisher #450030). The gRNA2 was selected
973 for the experiments in this study based upon its superior ability to upregulate Scn2a over gRNA1
974 and gRNA3 in cultured neurons.
975
976 **AAV-mediated expression of SCN1B and FGF12**
977
978 To express additional SCN1B or FGF12, cDNAs (Origene #RC209565, #RC215868) were cloned
979 into an AAV-expression vector downstream of the hSyn promotor. A non-targeting AAV-Flex-
980 GFP vector (from Dr. Il Hwan Kim) was used as a negative control. Cultured neurons were treated
981 with these AAV vectors (PHP.eB serotype) at DIV0 and lysed for Western blot analysis on DIV11.
982 Effective expression was confirmed by Western blot (SCN1B: Cell Signaling #13950S, 1:1000;
983 FGF12: Proteintech #13784-1-AP, 1:1000).
984
985 **Microelectrode Array (MEA)**
986

987 48-well MEA plates (Axion Biosystems #M768-KAP-48 or #M768-tMEA-48W) were coated with
988 1 mg/mL poly-L-lysine in borate buffer (pH 8.5). Forebrain tissue was rapidly isolated from P0-1
989 mice, dissociated with papain, and spotted at a density of 150,000 cells per the inner growth area
990 of each well. For experiments that required genotyping, brain tissue was temporarily stored in
991 Hibernate A solution (ThermoFisher #A1247501) at 4°C following the manufacturer's instructions
992 until ready for dissociation and plating. Viral treatments were applied at the day of plating.
993 Recordings were conducted on a Maestro MEA system (Axion Biosystems) on DIV 8, 11, and 14
994 for 10 min for each session, after 10 min of acclimation to the recording chamber (37°C, 5% CO_2
995 environment). After each recording, a half-change of growth media (Neurobasal A supplemented
996 with B27, GlutaMax, and 10 µg/mL Gentamicin) was performed. Recording data were analyzed
997 using the Axion Neural Metric Tool. Single electrode bursts were defined as a minimum of 5
998 spikes, separated by an inter-spike interval (ISI) of no more than 100 msec. Network bursts were
999 defined as a minimum of 10 spikes, separated by an ISI of no more than 100 msec with at least
1000 25% of the electrodes active. Statistical analyses (one-way ANOVA followed by pair-wise Tukey
1001 HSD *post-hoc* tests) were performed using JMP Pro (SAS).
1002
1003 **Behavioral Tests**
1004
1005 *Elevated zero maze:* Anxiety-like behaviors were assessed in the elevated zero maze as described
1006 under 40-60 lux illumination [112]. Mice were housed overnight in the test room and tested
1007 individually the next day. Animals were placed into a closed area of the maze and provided 5 min
1008 of free exploration. Videos were scored by trained observers blinded to the genotype and sex of
1009 the animals using the Noldus Observer XT15 program (Leesburg, VA) for the percent time in the
1010 open areas and the distance traveled.
1011
1012 *Hole-board test for repetitive behaviors:* Mice were housed in the test room overnight and the next
1013 day were examined in the hole-board test as described [112]. Individual mice were placed into a 42
1014 x 42 x 30 cm open field (Omnitech Electronics, Columbus, OH) and given free exploration of the
1015 apparatus for 10 min under 180 lux illumination. The hole-board apparatus consisted of a white
1016 Plexiglas floor with 16 equally spaced holes (3 cm in diameter) arranged in 4 rows. Head-dips

1017 into the holes were filmed and the videos were scored with the TopScan program (CleverSys,
1018 Reston, VA) for the numbers of head-dips and the location of each head-dip.
1019
1020 *Self-grooming:* Individual mice were housed in the test room overnight and the next day were
1021 habituated to clean home-cages for 10 min prior to testing [113]. Mice were filmed for 10 min for
1022 self-induced grooming. Subsequently, the videos were converted for analysis using Noldus
1023 MediaRecorder2. Grooming behavior was scored using TopScan software (CleverSys, Reston,
1024 VA) for the duration of self-grooming.
1025
1026 *Ultrasonic vocalizations (USVs):* Male WT and Scn2a$^{+/R102Q}$ mice were housed individually 1
1027 week before testing. Initially, males were primed twice with soiled bedding from estrous
1028 C57BL/6J females for 2 days. Subsequently, males were placed on clean bedding for 1 day, then
1029 on soiled bedding for another 2 days, and finally were returned to clean bedding overnight. Males
1030 were tested the next day. They were acclimated to the recording chambers for 2 min and then were
1031 introduced to an unfamiliar C57BL/6J female (12-16 weeks of age) for 8 min. Ultrasonic calls
1032 were recorded over the entire 10 min test as waveform audio files. The data were analyzed by
1033 scorers blinded to the genotypes of the mice using Avisoft SASLab Pro (Glienicke/Nordbahn,
1034 Germany) for the numbers of calls, call duration, and USV frequencies.
1035
1036 *Social behavior tests:* Social behavior in male WT and Scn2a$^{+/R102Q}$ mice was assessed in the
1037 resident-intruder and social dyadic assays [114]. The Scn2a males were housed individually on the
1038 same bedding for 14 days prior to testing; the partner C3H/HeJ mice (Jackson Laboratory, Bar
1039 Harbor, ME) were group-housed at 3-4 mice/cage. Both social tests were conducted with C3H/HeJ
1040 males matched for body weight with the Scn2a males. Note, the C3H/HeJ mice provide high
1041 amounts of social investigation without initiating unprovoked agonistic or attack behaviors [115].
1042 Social testing began within two hr after the lights had extinguished and was conducted under red
1043 light. Prior to testing, the chow, water bottle, and metal frame holding the water bottle were
1044 removed. The filter was removed from the top of the cage so behaviors could be filmed and the
1045 mouse could not escape. Tests were terminated if attacks by either Scn2a or C3H/HeJ males
1046 occurred for more than 1 min or if a mouse was injured. All behaviors were tested in the Social
1047 StereoScan apparatus (Cleversys) where behaviors can be filmed simultaneously from the top and

1048 sides of the test chamber. All videos were scored using Noldus Observer (version 15) by trained
1049 personnel blinded to the genotypes of the mice.
1050
1051 Mice were tested first in the resident-intruder assay. Here, a C3H/HeJ male was introduced into
1052 the home-cage of the WT or Scn2a$^{+/R102Q}$ male. Animals were allowed to interact for 5 min, after
1053 which the C3H/HeJ male was removed to its home-cage. Following this testing, the cages housing
1054 the individual Scn2a mice were replaced with new cages and bedding. Seven days later dyadic
1055 testing began where a WT or Scn2a$^{+/R102Q}$ male was paired with an unfamiliar C3H/HeJ male in a
1056 novel clear Plexiglas chamber (32 x 20 x 20 cm). Mice were placed at opposite ends of the
1057 chamber divided in half with a white polyfoam partition. Following a 5 min habituation, the
1058 partition was removed and the mice were permitted to interact for 5 min. All behaviors in both
1059 social tests were calculated as a rate per 5 min [(numbers of incidences/total test time in sec) x 300
1060 sec] and were analyzed over four response domains [114]. Mild-social investigation consisted of
1061 approaching, sniffing or nosing (ano-genital region), climbing onto the side or back, and/or
1062 grooming the face of the partner. Reactivity referred to boxing, holding, kicking, startling, and/or
1063 jumping in the presence of the partner. Agonistic behaviors denoted tail rattling to the partner
1064 and/or feinting, chasing, lunging, biting, climb-grooming, and/or attacking the partner. Withdrawal
1065 behaviors (no acknowledgement of partner) included walking-away, turning-away (without
1066 leaving proximity of the partner), or digging in the bedding when the partner contacts or attempts
1067 to interact.
1068
1069 *Statistics:* The data were presented as means and standard errors of the mean (SEMs). The zero
1070 maze, hole-board, self-grooming, and USV data were analyzed by independent-samples t-tests and
1071 the social behavior data were analyzed by repeated-measures ANOVA followed by Bonferroni
1072 corrected pair-wise comparisons. A $p < 0.05$ was considered significant. All statistical analyses
1073 were performed with IBM SPSS Statistics 28 programs (IBM, Chicago, IL) and the data were
1074 graphed using GraphPad Prism (Boston, MA).
1075

1076 **Figures and Legends**

1077

1078 **Fig. 1. HiUGE-iBioID reveals endogenous interactomes of 14 autism risk proteins.**

1079 (**A**) Schematic illustration of HiUGE-iBioID and its workflow. GS-sgRNA: gene-specific-gRNA.
1080 DS-sgRNA: donor-specific-gRNA. Strategies to preserve C-term PDZ-binding motifs of Syngap1,
1081 Ctnnb1, Iqsec2, and Lrrc4c are detailed. (**B**) Overview of 14 interactomes that segregates
1082 according to expected bait functions. (**C**) Enrichment analysis of overlapping SFARI genes using
1083 hypergeometric probability. (**D**) Interactome clustering based on a similarity matrix. (**E**) Core
1084 interactome between Syngap1 and Anks1b that show highly significant overlaps with SFARI
1085 genes. (**F**) Core interactome amongst Ank3, Scn2a, and Scn8a that are clustered based on
1086 similarity. Modules of proteins were isolated by MCL clustering or GO analysis.

1087

1088 **Fig. 2. Proteomic co-perturbation and functional convergence of Syngap1 and Anks1b**

1089 (**A**) Schematic illustration of the quantitative proteomic characterization of Syngap1-Het
1090 synaptosomes. (**B)** Proteomic alterations identified in the Syngap1-Het synaptosome. Proteins that
1091 overlap with Syngap1 interactome are underlined. (**C**) Co-immunoprecipitation result showing
1092 loss of interaction with ANKS1B in frame-shifting c.2214_2217del SYNGAP1 mutation. (**D**)
1093 HiUGE labeling of truncated Syngap1 at exon 13 shows synaptic localization (boxed region) and
1094 aberrant somatic mis-localization (arrowhead). Scale bar in the enlarged view represents 2μm.
1095 (**E**) Schematic illustration of labeling truncated Syngap1 with TurboID by targeting exon 13. (**F**)
1096 Western blot showing TurboID-HA labeled Syngap1 truncation at the expected molecular mass.
1097 (**G**) Proximity interactome network showing conserved and neomorphic interactions in Syngap1
1098 truncation. Note that interaction with Anks1b is no longer detected. (**H**) Schematics assessing
1099 phenotypes of the Syngap1-Anks1b functional interaction. (**I**) Western blot confirming disruption
1100 of Syngap1 and Anks1b expression. (**J**) Representative raster plots of neural activities at DIV-08,
1101 11, and 14. (**K-M**) Neurometrics showing further depletion of Anks1b exacerbates the
1102 development of precocious neural activity associated with Syngap1-LOF. *: $p < 0.05$; **: $p < 0.01$;
1103 ***: $p < 0.001$; n.s.: non-significant. One-way ANOVA followed by *post-hoc* Tukey HSD tests (n
1104 = 36 wells). Plots are mean ± SEM.

1105

1106 **Fig. 3. Intersectional proteomics reveal hidden molecular mechanism of a patient-derived**
1107 **Scn2a mutation.**
1108 (**A**) Generation of a mouse model based on a clinically identified Scn2a missense mutation
1109 (R102Q) in autistic individuals. WES: whole exome sequencing. (**B**) Behavioral face-validity of
1110 $Scn2a^{+/R102Q}$ mutants was assessed by (**i**) zero maze as the percent time and distance traveled in
1111 the open areas, (**ii)** hole-board test as numbers of head pokes and repeated head-pokes, (**iii)** self-
1112 grooming, and (**iv**) ultrasonic vocalizations (USVs) as numbers of calls, call durations, and call
1113 frequencies during social interaction. No differences were detected in the metrics of pre-social
1114 (baseline) responses in the USV tests. *: $p < 0.05$, **: $p < 0.01$, WT *vs.* $Scn2a^{+/R102Q}$ mice;
1115 independent samples t-tests, two-tailed. Statistics are summarized in Table S6. (**C**) Spatial
1116 proteomics reveals co-perturbations in $Scn2a^{+/R102Q}$ mutants. MCL analysis discovered a key
1117 cluster associated with voltage-gated channel activity that is down-regulated, including three
1118 targets that intersect with the Scn2a HiUGE-iBioID interactome (underlined). (**D**) $Scn2a^{+/R102Q}$
1119 mutant neurons show attenuated activity with the MEA. Scn2a-CRISPRa treatment and a
1120 "Combo" treatment with additional expression of SCN1B and FGF12 show differential efficacy
1121 in restoring neural activity deficits. *: $p < 0.05$; **: $p < 0.01$; ***: $p < 0.001$; n.s.: non-significant.
1122 One-way ANOVA followed by *post-hoc* Tukey HSD tests (n = 48 wells). Plots are mean ± SEM.
1123
1124

1125 **Supplementary Materials**

1126

1127 **Fig. S1. HiUGE labeling of 14 high-risk autism proteins.**

1128 (**A**) Representative images showing wide-spread TurboID-mediated biotinylation across the brain
1129 following labeling Tubb3 with HiUGE. (**B-O**) Representative images showing correct localization
1130 (arrowheads) of 14 high-risk autism proteins labeled with a highly antigenic "spaghetti monster"
1131 fluorescent protein (smFP), with boxed regions enlarged in (**Q**) to show colocalization with a
1132 synaptic marker Homer1. PDZ-binding motifs were preserved using #: intron-targeting strategy
1133 and §: modified donor incorporating native PDZ-binding motif. (**P**) Representative image of the
1134 negative control. Scale bar in the enlarged view represents 2μm.

1135

1136 **Fig. S2. Immunofluorescence detection of representative bait proteins with HiUGE labeling.**

1137 (**A-D**) Representative images showing colocalization of smFP-labeled proteins with
1138 immunofluorescence detected by specific antibodies against native proteins (Syngap1, Shank2,
1139 Ank3, Scn2a). Scale bar in the enlarged view represents 2μm.

1140

1141 **Fig. S3. Western blot of HiUGE-iBioID purified samples following streptavidin pulldown.**

1142 (**A**) Schematic illustration of enriching biotinylated proteins by streptavidin pulldown. (**B-H**)
1143 Western blot images showing detection of TurboID-HA fusion proteins at the expected molecular
1144 masses following purifications, (**B, C, H**) detection of an expected synaptic interactor (PSD95) is
1145 also confirmed. (**G, H**) Western blot images showing detection of soluble TurboID-HA (as a
1146 survey for background) by multiplexed insertion of IRES-TurboID-HA donor near 3'UTR.

1147

1148 **Fig. S4. Reciprocal validation and comparison with immunoprecipitation.**

1149 (**A**) Network graph showing extensive reciprocal identifications amongst autism risk protein baits.
1150 (**B-D**) Immunofluorescence and Western blot validation of HiUGE-iBioID for Homer1 and Wasf1,
1151 two exemplary proteomic "hubs" detected by many baits. (**E, F**) Network graphs showing
1152 reciprocal identifications of the initial baits by these "hubs". (**G, H**) Hypergeometric analyses of
1153 overlap between the HiUGE-iBioID proteomes of the initial baits and the "hubs" show highly
1154 significant overlaps. No significant overlap is detected when comparing to the Hnrnpu dataset. **(I,**
1155 **J)** Comparison of HiUGE-iBioID results with proteomic detections following

1156 immunoprecipitation using monoclonal antibodies. Western blot images of brain lysate samples
1157 using these antibodies are shown. Genes that overlap with HiUGE-iBioID are highlighted on the
1158 volcano plot, and a few genes related to synaptic and ion channel functions are labeled.
1159 Significance of overlap is determined by hypergeometric test. (**K, L**) Comparative GO analyses of
1160 the gene sets that are exclusive to either the immunoprecipitation or the HiUGE-iBioID datasets.
1161 The statistical domain is the cumulative proteomic detections of brain-derived samples in our lab
1162 (Table S5).
1163
1164 **Fig. S5. Overlap of HiUGE-iBioID interactomes with published datasets.**
1165 (**A**) Significance of interactome overlap with differentially expressed genes (DEGs) found in
1166 autistic individuals across excitatory neurons, interneurons, and non-neuronal cell populations. (**B**)
1167 Significance of interactome overlap with autism risk genes identified by Satterstrom et al. [3], and
1168 Fu et al. [7]. Thresholds for statistical significance were delineated on the graphs.
1169
1170 **Fig. S6. Structure-function analysis of SYNGAP1-ANKS1B interaction.**
1171 (**A**) Schematic illustration of assessing the ANKS1B interaction with SYNGAP1 truncations using
1172 human cDNA constructs expressed in HEK293T cells. (**B**) Co-immunoprecipitation results
1173 showing the interaction with ANKS1B ablated in C1- and C2- SYNGAP1 truncations while
1174 retained in C3- and N- truncations.
1175
1176 **Fig. S7. Additional social behavior data for the Scn2a$^{+/R102Q}$ mice.**
1177 (**A**) Scn2a$^{+/R102Q}$ males initiated more overall social events in the dyadic assay with C3H/HeJ males
1178 than WT males (p = 0.013). (**B**) No genotype effect was detected for the percent of mild social
1179 interactions (MSI). (**C**) No genotype effect was detected for the percent of reactivity events. (**D**)
1180 The numbers of agonistic events were very low and were not distinguished by social test or
1181 genotype. (**E**) The percent of withdrawal events from C3H/HeJ partners was lower in the
1182 Scn2a$^{+/R102Q}$ males than WT males (genotype effect, p = 0.020). (**F**) No genotype effect was
1183 detected for the self-focused behaviors. The data are presented as means ± SEMs and were
1184 analyzed with RMANOVA with Bonferroni corrections, n = 8 mice / genotype. *: $p < 0.05$, WT
1185 vs. Scn2a$^{+/R102Q}$ mice. Additional statistics are summarized in Table S6.
1186

1187 **Fig. S8. Additional data of the Scn2a$^{+/R102Q}$ phenotypic rescue experiment.**
1188 (**A**) Quantitative PCR screening of three different CRISPRa gRNAs targeting Scn2a *in vitro*. The
1189 gRNA2 shows the best performance in upregulating Scn2a expression, and is used for subsequent
1190 experiments (ANOVA followed by Dunnett's test, n = 3 wells). Specificity of the qPCR assay is
1191 validated by sequencing the amplicon. (**B**) mRNA expression levels of Scn2a, Scn1b, and Fgf12
1192 in cultured Scn2a$^{+/R102Q}$ mutant neurons are comparable to that of WT (two-tailed *t*-test, n = 4
1193 wells). (**C**) MEA neurometrics following overexpression of SCN1B, FGF12, or combined showing
1194 ineffective rescue of the Scn2a$^{+/R102Q}$ phenotype, One-way ANOVA followed by *post-hoc* Tukey
1195 HSD tests (n= 36 or 48 wells). (**D**) Additional neurometrics from the MEA recording of the
1196 "Combo" treatment experiment. One-way ANOVA followed by *post-hoc* Tukey HSD tests (n= 48
1197 wells). *: $p < 0.05$; **: $p < 0.01$; ***: $p < 0.001$; n.s.: non-significant. Plots are mean ± SEM.
1198
1199 **Fig. S9. Comparative GO analysis with a recently published autism risk protein**
1200 **immunoprecipitation dataset using human iPSC-derived neurons.**
1201 (**A-D**) Comparative GO analyses of genes that are exclusive to either the immunoprecipitation
1202 dataset using human iPSC-derived neurons [28] or the HiUGE-iBioID dataset for Syngap1, Shank3,
1203 Scn2a and Ctnnb1. The human genes were converted to mouse orthologs before intersecting with
1204 HiUGE-iBioID dataset. Bait self-IDs were excluded for this analysis. Due to the lack of a
1205 consensus statistical domain, mouse genome was used as a non-biased background. Top molecular
1206 function GO terms are shown.
1207
1208 **Fig. S10. Comparative GO analysis with a recently published autism risk protein**
1209 **recombinant BioID dataset using cultured neurons.**
1210 (**A-C**) Comparative GO analyses of genes that are exclusive to either the recombinant BioID
1211 expression dataset using primary mouse neurons [27] or the HiUGE-iBioID dataset for Syngap1,
1212 Shank3, and Lrrc4c. Bait self-IDs were excluded for this analysis. Due to the lack of a consensus
1213 statistical domain, mouse genome was used as a non-biased background. Top molecular function
1214 GO terms are shown.
1215
1216 **Fig. S11-S26. Individual interactome networks of 14 autism risk proteins and the additional**
1217 **2 "hub" proteins.**

1218 Interactome network associated with the bait protein is shown in each Figure. Blue lines denote
1219 STRING interactions and red lines signify identified HiUGE-iBioID interactions. Yellow nodes
1220 highlight proteins encoded by SFARI gene orthologs. Annotations denote exemplary significant
1221 gene ontology (GO) terms associated with the protein clusters segregated by MCL. Unless
1222 otherwise specified, the Biological Process pathway database was used. CC: Cellular Component
1223 pathway database. Charts of GO results of the overall bait interactomes using the Molecular
1224 Function (MF) pathway database are shown as well, below each network plot.
1225
1226 **Fig. S27. SynGO analyses of the synaptic bait interactomes versus the nucleus bait**
1227 **interactome.**
1228 SynGO analyses showing the expected functions of the synaptic bait interactomes mainly within
1229 the domains of "synapse organization" and "process in the postsynapse". In contrast, no significant
1230 SynGO enrichment was detected for the nucleus Hnrnpu interactome.
1231
1232 **Table S1. Proteomic results and statistics of HiUGE-iBioID experiments.**
1233 Proteomic results and statistics of HiUGE-iBioID experiments are shown. Batch-1: Anks1b,
1234 Shank2, Nckap1; Batch-2: Nbea; Batch-3: Ank3, Scn2a, Scn8a; Batch-4: Arhgef9, Hnrnpu; Batch-
1235 5: Shank3; Batch-6: Syngap1-Trunc; Batch-7: Soluble TurboID; Batch-8: Syngap1, Ctnnb1,
1236 Iqsec2, Lrrc4c (modified strategies to preserve PDZ-binding motifs); Batch-9: Homer1, Wasf1.
1237
1238 **Table S2. HiUGE-iBioID interactomes and their overlaps with autism gene lists.**
1239 Filtered gene lists of the detected interactomes associated with 14 high-risk autism targets are
1240 shown. The genes that overlap with the SFARI database, Satterstrom et al. [3], and Fu et al. [7] gene
1241 lists are shown in a separate tab.
1242
1243 **Table S3. Proteomic detection following antibody immunoprecipitations.**
1244 Proteomic results and statistics of Anks1b and Scn2a immunoprecipitation experiments.
1245
1246 **Table S4. Proteomic results and statistics of spatial co-perturbation experiments.**

1247 Proteomic results and statistics of spatial co-perturbation experiments are shown, including
1248 comparisons of Syngap1-Het synaptosome proteome with WT in the cortex and striatum, and
1249 comparison of Scn2a$^{+/R102Q}$ LOPIT-DC fraction-5 proteome with WT.
1250
1251 **Table S5. Statistical domain for GO analyses.**
1252 Statistical domain for GO analyses compiled from cumulative proteomic detections of brain-
1253 derived samples in our lab.
1254
1255 **Table S6. Statistics for behavioral characterization of Scn2a$^{+/R102Q}$ mice.**
1256 Metrics and statistic summaries for the elevated zero maze, hole-board, self-grooming, USV,
1257 resident-intruder, and social dyadic tests are reported in this Table. For the USV test, no
1258 statistically significant differences were detected in the following pre-social (baseline) responses:
1259 Number of calls: WT (8.0 ± 1.6), Scn2a$^{+/R102Q}$ (5.9 ± 2.8) [t(22)=0.693, p=0.496]; and Call
1260 frequency (kHz): WT (30.4 ± 2.7), Scn2a$^{+/R102Q}$ (20.0 ± 5.5) [t(22)=1.858, p=0.077]. Difference
1261 in call duration (msec) was marginal: WT (6.8 ± 0.8), Scn2a$^{+/R102Q}$ (4.0 ± 1.2) [t(22)=2.070,
1262 p=0.050]; n = 14 WT males, n = 10 Scn2a$^{+/R102Q}$ males; data presented as means ± SEM,
1263 independent samples t-tests, two-tailed.
1264
1265 **Table S7. Results of the enrichment analyses between the HiUGE-iBioID interactomes and**
1266 **an autism GWAS study.**
1267 Results of the enrichment analyses between the HiUGE-iBioID and Grove et al., 2019, autism
1268 genome-wide association meta-analysis (GWAS) using MAGMA.
1269
1270

References and Notes

1 Lord, C. *et al.* Autism spectrum disorder. *Nat Rev Dis Primers* **6**, 5, doi:10.1038/s41572-019-0138-4 (2020).

2 Banerjee-Basu, S. & Packer, A. SFARI Gene: an evolving database for the autism research community. *Dis Model Mech* **3**, 133-135, doi:10.1242/dmm.005439 (2010).

3 Satterstrom, F. K. *et al.* Large-Scale Exome Sequencing Study Implicates Both Developmental and Functional Changes in the Neurobiology of Autism. *Cell* **180**, 568-584 e523, doi:10.1016/j.cell.2019.12.036 (2020).

4 Wang, T. *et al.* Large-scale targeted sequencing identifies risk genes for neurodevelopmental disorders. *Nat Commun* **11**, 4932, doi:10.1038/s41467-020-18723-y (2020).

5 Zoghbi, H. Y. Postnatal neurodevelopmental disorders: meeting at the synapse? *Science* **302**, 826-830, doi:10.1126/science.1089071 (2003).

6 Ayhan, F. & Konopka, G. Regulatory genes and pathways disrupted in autism spectrum disorders. *Prog Neuropsychopharmacol Biol Psychiatry* **89**, 57-64, doi:10.1016/j.pnpbp.2018.08.017 (2019).

7 Fu, J. M. *et al.* Rare coding variation provides insight into the genetic architecture and phenotypic context of autism. *Nat Genet*, doi:10.1038/s41588-022-01104-0 (2022).

8 Velmeshev, D. *et al.* Single-cell genomics identifies cell type-specific molecular changes in autism. *Science* **364**, 685-689, doi:10.1126/science.aav8130 (2019).

9 Menashe, I., Grange, P., Larsen, E. C., Banerjee-Basu, S. & Mitra, P. P. Co-expression profiling of autism genes in the mouse brain. *PLoS Comput Biol* **9**, e1003128, doi:10.1371/journal.pcbi.1003128 (2013).

10 Voineagu, I. *et al.* Transcriptomic analysis of autistic brain reveals convergent molecular pathology. *Nature* **474**, 380-384, doi:10.1038/nature10110 (2011).

11 Quesnel-Vallieres, M., Weatheritt, R. J., Cordes, S. P. & Blencowe, B. J. Autism spectrum disorder: insights into convergent mechanisms from transcriptomics. *Nat Rev Genet* **20**, 51-63, doi:10.1038/s41576-018-0066-2 (2019).

12 O'Roak, B. J. *et al.* Sporadic autism exomes reveal a highly interconnected protein network of de novo mutations. *Nature* **485**, 246-250, doi:10.1038/nature10989 (2012).

13 Li, T. *et al.* A scored human protein-protein interaction network to catalyze genomic interpretation. *Nat Methods* **14**, 61-64, doi:10.1038/nmeth.4083 (2017).

14 Neale, B. M. *et al.* Patterns and rates of exonic de novo mutations in autism spectrum disorders. *Nature* **485**, 242-245, doi:10.1038/nature11011 (2012).

15 Sakai, Y. *et al.* Protein interactome reveals converging molecular pathways among autism disorders. *Sci Transl Med* **3**, 86ra49, doi:10.1126/scitranslmed.3002166 (2011).

16 Donato, A., Kagias, K., Zhang, Y. & Hilliard, M. A. Neuronal sub-compartmentalization: a strategy to optimize neuronal function. *Biol Rev Camb Philos Soc* **94**, 1023-1037, doi:10.1111/brv.12487 (2019).

17 Terenzio, M., Schiavo, G. & Fainzilber, M. Compartmentalized Signaling in Neurons: From Cell Biology to Neuroscience. *Neuron* **96**, 667-679, doi:10.1016/j.neuron.2017.10.015 (2017).

18 De Rubeis, S. *et al.* Synaptic, transcriptional and chromatin genes disrupted in autism. *Nature* **515**, 209-215, doi:10.1038/nature13772 (2014).

1316 19 Santini, E. & Klann, E. Reciprocal signaling between translational control pathways and
1317 synaptic proteins in autism spectrum disorders. *Sci Signal* **7**, re10,
1318 doi:10.1126/scisignal.2005832 (2014).
1319 20 Grant, S. G. Synaptopathies: diseases of the synaptome. *Curr Opin Neurobiol* **22**, 522-
1320 529, doi:10.1016/j.conb.2012.02.002 (2012).
1321 21 Fujitani, M., Otani, Y. & Miyajima, H. Pathophysiological Roles of Abnormal Axon
1322 Initial Segments in Neurodevelopmental Disorders. *Cells* **10**, doi:10.3390/cells10082110
1323 (2021).
1324 22 Kruth, K. A., Grisolano, T. M., Ahern, C. A. & Williams, A. J. SCN2A channelopathies
1325 in the autism spectrum of neuropsychiatric disorders: a role for pluripotent stem cells?
1326 *Mol Autism* **11**, 23, doi:10.1186/s13229-020-00330-9 (2020).
1327 23 Uezu, A. *et al.* Identification of an elaborate complex mediating postsynaptic inhibition.
1328 *Science* **353**, 1123-1129, doi:10.1126/science.aag0821 (2016).
1329 24 Hamdan, H. *et al.* Mapping axon initial segment structure and function by multiplexed
1330 proximity biotinylation. *Nat Commun* **11**, 100, doi:10.1038/s41467-019-13658-5 (2020).
1331 25 Bayes, A. *et al.* Characterization of the proteome, diseases and evolution of the human
1332 postsynaptic density. *Nat Neurosci* **14**, 19-21, doi:10.1038/nn.2719 (2011).
1333 26 Distler, U. *et al.* In-depth protein profiling of the postsynaptic density from mouse
1334 hippocampus using data-independent acquisition proteomics. *Proteomics* **14**, 2607-2613,
1335 doi:10.1002/pmic.201300520 (2014).
1336 27 Murtaza, N. *et al.* Neuron-specific protein network mapping of autism risk genes
1337 identifies shared biological mechanisms and disease-relevant pathologies. *Cell Rep* **41**,
1338 111678, doi:10.1016/j.celrep.2022.111678 (2022).
1339 28 Pintacuda, G. *et al.* Protein interaction studies in human induced neurons indicate
1340 convergent biology underlying autism spectrum disorders. *Cell Genom* **3**, 100250,
1341 doi:10.1016/j.xgen.2022.100250 (2023).
1342 29 Piersimoni, L., Kastritis, P. L., Arlt, C. & Sinz, A. Cross-Linking Mass Spectrometry for
1343 Investigating Protein Conformations and Protein-Protein Interactions - A Method for All
1344 Seasons. *Chem Rev* **122**, 7500-7531, doi:10.1021/acs.chemrev.1c00786 (2022).
1345 30 Geladaki, A. *et al.* Combining LOPIT with differential ultracentrifugation for high-
1346 resolution spatial proteomics. *Nat Commun* **10**, 331, doi:10.1038/s41467-018-08191-w
1347 (2019).
1348 31 Gao, Y. *et al.* Plug-and-Play Protein Modification Using Homology-Independent
1349 Universal Genome Engineering. *Neuron* **103**, 583-597 e588,
1350 doi:10.1016/j.neuron.2019.05.047 (2019).
1351 32 Branon, T. C. *et al.* Efficient proximity labeling in living cells and organisms with
1352 TurboID. *Nat Biotechnol* **36**, 880-887, doi:10.1038/nbt.4201 (2018).
1353 33 Zhong, H. *et al.* High-fidelity, efficient, and reversible labeling of endogenous proteins
1354 using CRISPR-based designer exon insertion. *Elife* **10**, doi:10.7554/eLife.64911 (2021).
1355 34 Szklarczyk, D. *et al.* The STRING database in 2021: customizable protein-protein
1356 networks, and functional characterization of user-uploaded gene/measurement sets.
1357 *Nucleic Acids Res* **49**, D605-D612, doi:10.1093/nar/gkaa1074 (2021).
1358 35 Snel, B., Lehmann, G., Bork, P. & Huynen, M. A. STRING: a web-server to retrieve and
1359 display the repeatedly occurring neighbourhood of a gene. *Nucleic Acids Res* **28**, 3442-
1360 3444, doi:10.1093/nar/28.18.3442 (2000).

36 Beyreli, I., Karakahya, O. & Cicek, A. E. DeepND: Deep multitask learning of gene risk for comorbid neurodevelopmental disorders. *Patterns* **3**, doi:10.1016/j.patter.2022.100524 (2022).
37 Seiffert, S. *et al.* Modulating effects of FGF12 variants on NaV1.2 and NaV1.6 associated with Developmental and Epileptic Encephalopathy and Autism Spectrum Disorder. *bioRxiv* doi:10.1101/2021.12.03.471090 (2021).
38 Zhou, X. *et al.* Integrating de novo and inherited variants in 42,607 autism cases identifies mutations in new moderate-risk genes. *Nat Genet*, doi:10.1038/s41588-022-01148-2 (2022).
39 O'Neil, S. D. *et al.* Action potential-coupled Rho GTPase signaling drives presynaptic plasticity. *Elife* **10**, doi:10.7554/eLife.63756 (2021).
40 Stockhammer, A. *et al.* When less is more – Endogenous tagging with TurboID as a tool to study the native interactome of adaptor protein complexes. *bioRxiv*, doi:10.1101/2021.11.19.469212 (2022).
41 pfeliciano@simonsfoundation.org, S. C. E. a. & Consortium, S. SPARK: A US Cohort of 50,000 Families to Accelerate Autism Research. *Neuron* **97**, 488-493, doi:10.1016/j.neuron.2018.01.015 (2018).
42 Simons Vip, C. Simons Variation in Individuals Project (Simons VIP): a genetics-first approach to studying autism spectrum and related neurodevelopmental disorders. *Neuron* **73**, 1063-1067, doi:10.1016/j.neuron.2012.02.014 (2012).
43 Viswanathan, S. *et al.* High-performance probes for light and electron microscopy. *Nat Methods* **12**, 568-576, doi:10.1038/nmeth.3365 (2015).
44 Grove, J. *et al.* Identification of common genetic risk variants for autism spectrum disorder. *Nat Genet* **51**, 431-444, doi:10.1038/s41588-019-0344-8 (2019).
45 Enright, A. J., Van Dongen, S. & Ouzounis, C. A. An efficient algorithm for large-scale detection of protein families. *Nucleic Acids Res* **30**, 1575-1584, doi:10.1093/nar/30.7.1575 (2002).
46 Li, J. *et al.* Long-term potentiation modulates synaptic phosphorylation networks and reshapes the structure of the postsynaptic interactome. *Sci Signal* **9**, rs8, doi:10.1126/scisignal.aaf6716 (2016).
47 Li, J. *et al.* Spatiotemporal profile of postsynaptic interactomes integrates components of complex brain disorders. *Nat Neurosci* **20**, 1150-1161, doi:10.1038/nn.4594 (2017).
48 Wilkinson, B., Li, J. & Coba, M. P. Synaptic GAP and GEF Complexes Cluster Proteins Essential for GTP Signaling. *Sci Rep* **7**, 5272, doi:10.1038/s41598-017-05588-3 (2017).
49 Tindi, J. O. *et al.* ANKS1B Gene Product AIDA-1 Controls Hippocampal Synaptic Transmission by Regulating GluN2B Subunit Localization. *J Neurosci* **35**, 8986-8996, doi:10.1523/JNEUROSCI.4029-14.2015 (2015).
50 Gamache, T. R., Araki, Y. & Huganir, R. L. Twenty Years of SynGAP Research: From Synapses to Cognition. *J Neurosci* **40**, 1596-1605, doi:10.1523/JNEUROSCI.0420-19.2020 (2020).
51 Dosemeci, A., Toy, D., Burch, A., Bayer, K. U. & Tao-Cheng, J. H. CaMKII-mediated displacement of AIDA-1 out of the postsynaptic density core. *FEBS Lett* **590**, 2934-2939, doi:10.1002/1873-3468.12334 (2016).
52 Yang, Y., Tao-Cheng, J. H., Reese, T. S. & Dosemeci, A. SynGAP moves out of the core of the postsynaptic density upon depolarization. *Neuroscience* **192**, 132-139, doi:10.1016/j.neuroscience.2011.06.061 (2011).

1407 53 Araki, Y., Zeng, M., Zhang, M. & Huganir, R. L. Rapid dispersion of SynGAP from
1408 synaptic spines triggers AMPA receptor insertion and spine enlargement during LTP.
1409 *Neuron* **85**, 173-189, doi:10.1016/j.neuron.2014.12.023 (2015).
1410 54 Carbonell, A. U. *et al.* Haploinsufficiency in the ANKS1B gene encoding AIDA-1 leads
1411 to a neurodevelopmental syndrome. *Nat Commun* **10**, 3529, doi:10.1038/s41467-019-
1412 11437-w (2019).
1413 55 Berryer, M. H. *et al.* Mutations in SYNGAP1 cause intellectual disability, autism, and a
1414 specific form of epilepsy by inducing haploinsufficiency. *Hum Mutat* **34**, 385-394,
1415 doi:10.1002/humu.22248 (2013).
1416 56 Kim, J. H., Lee, H.-K., Takamiya, K. & Huganir, R. L. The Role of Synaptic GTPase-
1417 Activating Protein in Neuronal Development and Synaptic Plasticity. *The Journal of*
1418 *Neuroscience* **23**, 1119-1124, doi:10.1523/jneurosci.23-04-01119.2003 (2003).
1419 57 Nakajima, R. *et al.* Comprehensive behavioral analysis of heterozygous Syngap1
1420 knockout mice. *Neuropsychopharmacol Rep* **39**, 223-237, doi:10.1002/npr2.12073
1421 (2019).
1422 58 Komiyama, N. H. *et al.* SynGAP Regulates ERK/MAPK Signaling, Synaptic Plasticity,
1423 and Learning in the Complex with Postsynaptic Density 95 and NMDA Receptor. *The*
1424 *Journal of Neuroscience* **22**, 9721-9732, doi:10.1523/jneurosci.22-22-09721.2002 (2002).
1425 59 Carlin, R. K., Grab, D. J., Cohen, R. S. & Siekevitz, P. Isolation and characterization of
1426 postsynaptic densities from various brain regions: enrichment of different types of
1427 postsynaptic densities. *J Cell Biol* **86**, 831-845, doi:10.1083/jcb.86.3.831 (1980).
1428 60 Schmeisser, M. J. *et al.* Autistic-like behaviours and hyperactivity in mice lacking
1429 ProSAP1/Shank2. *Nature* **486**, 256-260, doi:10.1038/nature11015 (2012).
1430 61 Mignot, C. *et al.* Genetic and neurodevelopmental spectrum of SYNGAP1-associated
1431 intellectual disability and epilepsy. *J Med Genet* **53**, 511-522, doi:10.1136/jmedgenet-
1432 2015-103451 (2016).
1433 62 Kilinc, M. *et al.* Endogenous Syngap1 alpha splice forms promote cognitive function and
1434 seizure protection. *Elife* **11**, doi:10.7554/eLife.75707 (2022).
1435 63 Llamosas, N. *et al.* SYNGAP1 Controls the Maturation of Dendrites, Synaptic Function,
1436 and Network Activity in Developing Human Neurons. *J Neurosci* **40**, 7980-7994,
1437 doi:10.1523/JNEUROSCI.1367-20.2020 (2020).
1438 64 Clement, J. P. *et al.* Pathogenic SYNGAP1 mutations impair cognitive development by
1439 disrupting maturation of dendritic spine synapses. *Cell* **151**, 709-723,
1440 doi:10.1016/j.cell.2012.08.045 (2012).
1441 65 Spratt, P. W. E. *et al.* The Autism-Associated Gene Scn2a Contributes to Dendritic
1442 Excitability and Synaptic Function in the Prefrontal Cortex. *Neuron* **103**, 673-685 e675,
1443 doi:10.1016/j.neuron.2019.05.037 (2019).
1444 66 Ben-Shalom, R. *et al.* Opposing Effects on NaV1.2 Function Underlie Differences
1445 Between SCN2A Variants Observed in Individuals With Autism Spectrum Disorder or
1446 Infantile Seizures. *Biol Psychiatry* **82**, 224-232, doi:10.1016/j.biopsych.2017.01.009
1447 (2017).
1448 67 Sanders, S. J. *et al.* De novo mutations revealed by whole-exome sequencing are strongly
1449 associated with autism. *Nature* **485**, 237-241, doi:10.1038/nature10945 (2012).
1450 68 Wang, T. *et al.* De novo genic mutations among a Chinese autism spectrum disorder
1451 cohort. *Nat Commun* **7**, 13316, doi:10.1038/ncomms13316 (2016).

1452 69 Callaghan, D. B. *et al.* Whole genome sequencing and variant discovery in the ASPIRE
1453 autism spectrum disorder cohort. *Clin Genet* **96**, 199-206, doi:10.1111/cge.13556 (2019).
1454 70 Berecki, G. *et al.* Functional correlates of clinical phenotype and severity in recurrent
1455 SCN2A variants. *Commun Biol* **5**, 515, doi:10.1038/s42003-022-03454-1 (2022).
1456 71 Courtland, J. L. *et al.* Genetic disruption of WASHC4 drives endo-lysosomal dysfunction
1457 and cognitive-movement impairments in mice and humans. *Elife* **10**,
1458 doi:10.7554/eLife.61590 (2021).
1459 72 Brackenbury, W. J. & Isom, L. L. Na Channel beta Subunits: Overachievers of the Ion
1460 Channel Family. *Front Pharmacol* **2**, 53, doi:10.3389/fphar.2011.00053 (2011).
1461 73 Turner, C. A., Watson, S. J. & Akil, H. The fibroblast growth factor family:
1462 neuromodulation of affective behavior. *Neuron* **76**, 160-174,
1463 doi:10.1016/j.neuron.2012.08.037 (2012).
1464 74 Tamura, S. *et al.* CRISPR activation rescues abnormalities in SCN2A haploinsufficiency-
1465 associated autism spectrum disorder. *bioRxiv*, doi:10.1101/2022.03.30.486483 (2022).
1466 75 Wildburger, N. C. *et al.* Quantitative proteomics reveals protein-protein interactions with
1467 fibroblast growth factor 12 as a component of the voltage-gated sodium channel 1.2
1468 (nav1.2) macromolecular complex in Mammalian brain. *Mol Cell Proteomics* **14**, 1288-
1469 1300, doi:10.1074/mcp.M114.040055 (2015).
1470 76 Repetto, D. *et al.* Molecular Dissection of Neurobeachin Function at Excitatory
1471 Synapses. *Front Synaptic Neurosci* **10**, 28, doi:10.3389/fnsyn.2018.00028 (2018).
1472 77 Gromova, K. V. *et al.* Neurobeachin and the Kinesin KIF21B Are Critical for Endocytic
1473 Recycling of NMDA Receptors and Regulate Social Behavior. *Cell Rep* **23**, 2705-2717,
1474 doi:10.1016/j.celrep.2018.04.112 (2018).
1475 78 Wang, X. *et al.* Neurobeachin: A Protein Kinase A-Anchoring,beige/Chediak-Higashi
1476 Protein Homolog Implicated in Neuronal Membrane Traffic. *The Journal of*
1477 *Neuroscience* **20**, 8551-8565, doi:10.1523/jneurosci.20-23-08551.2000 (2000).
1478 79 Nair, R. *et al.* Neurobeachin regulates neurotransmitter receptor trafficking to synapses. *J*
1479 *Cell Biol* **200**, 61-80, doi:10.1083/jcb.201207113 (2013).
1480 80 Mulhern, M. S. *et al.* NBEA: Developmental disease gene with early generalized epilepsy
1481 phenotypes. *Ann Neurol* **84**, 788-795, doi:10.1002/ana.25350 (2018).
1482 81 Castermans, D. *et al.* The neurobeachin gene is disrupted by a translocation in a patient
1483 with idiopathic autism. *J Med Genet* **40**, 352-356, doi:10.1136/jmg.40.5.352 (2003).
1484 82 Farzana, F. *et al.* Neurobeachin Regulates Glutamate- and GABA-Receptor Targeting to
1485 Synapses via Distinct Pathways. *Mol Neurobiol* **53**, 2112-2123, doi:10.1007/s12035-015-
1486 9164-8 (2016).
1487 83 Thompson, A. *et al.* Tandem mass tags: a novel quantification strategy for comparative
1488 analysis of complex protein mixtures by MS/MS. *Anal Chem* **75**, 1895-1904,
1489 doi:10.1021/ac0262560 (2003).
1490 84 Bachor, R., Waliczek, M., Stefanowicz, P. & Szewczuk, Z. Trends in the Design of New
1491 Isobaric Labeling Reagents for Quantitative Proteomics. *Molecules* **24**,
1492 doi:10.3390/molecules24040701 (2019).
1493 85 Takano, T. *et al.* Chemico-genetic discovery of astrocytic control of inhibition in vivo.
1494 *Nature* **588**, 296-302, doi:10.1038/s41586-020-2926-0 (2020).
1495 86 Jumper, J. *et al.* Highly accurate protein structure prediction with AlphaFold. *Nature* **596**,
1496 583-589, doi:10.1038/s41586-021-03819-2 (2021).

87 Lin, Z. *et al.* Evolutionary-scale prediction of atomic-level protein structure with a language model. *Science* **379**, 1123-1130, doi:10.1126/science.ade2574 (2023).
88 Slavov, N. Unpicking the proteome in single cells. *Science* **367**, 512-513, doi:10.1126/science.aaz6695 (2020).
89 Liang, Y. *et al.* Fully Automated Sample Processing and Analysis Workflow for Low-Input Proteome Profiling. *Anal Chem* **93**, 1658-1666, doi:10.1021/acs.analchem.0c04240 (2021).
90 Rosenberger, F. A., Thielert, M. & Mann, M. Making single-cell proteomics biologically relevant. *Nat Methods* **20**, 320-323, doi:10.1038/s41592-023-01771-9 (2023).
91 Lin, Y., Afshar, S., Rajadhyaksha, A. M., Potash, J. B. & Han, S. A Machine Learning Approach to Predicting Autism Risk Genes: Validation of Known Genes and Discovery of New Candidates. *Front Genet* **11**, 500064, doi:10.3389/fgene.2020.500064 (2020).
92 Brueggeman, L., Koomar, T. & Michaelson, J. J. Forecasting risk gene discovery in autism with machine learning and genome-scale data. *Sci Rep* **10**, 4569, doi:10.1038/s41598-020-61288-5 (2020).
93 Schoof, E. M. *et al.* Quantitative single-cell proteomics as a tool to characterize cellular hierarchies. *Nat Commun* **12**, 3341, doi:10.1038/s41467-021-23667-y (2021).
94 Brunner, A. D. *et al.* Ultra-high sensitivity mass spectrometry quantifies single-cell proteome changes upon perturbation. *Mol Syst Biol* **18**, e10798, doi:10.15252/msb.202110798 (2022).
95 Vistain, L. F. & Tay, S. Single-Cell Proteomics. *Trends Biochem Sci* **46**, 661-672, doi:10.1016/j.tibs.2021.01.013 (2021).
96 Walkup, W. G. t. *et al.* Phosphorylation of synaptic GTPase-activating protein (synGAP) by Ca2+/calmodulin-dependent protein kinase II (CaMKII) and cyclin-dependent kinase 5 (CDK5) alters the ratio of its GAP activity toward Ras and Rap GTPases. *J Biol Chem* **290**, 4908-4927, doi:10.1074/jbc.M114.614420 (2015).
97 Walkup, W. G. *et al.* A model for regulation by SynGAP-alpha1 of binding of synaptic proteins to PDZ-domain 'Slots' in the postsynaptic density. *Elife* **5**, doi:10.7554/eLife.16813 (2016).
98 Goldfarb, M. *et al.* Fibroblast growth factor homologous factors control neuronal excitability through modulation of voltage-gated sodium channels. *Neuron* **55**, 449-463, doi:10.1016/j.neuron.2007.07.006 (2007).
99 Johnson, K. W., Herold, K. F., Milner, T. A., Hemmings, H. C., Jr. & Platholi, J. Sodium channel subtypes are differentially localized to pre- and post-synaptic sites in rat hippocampus. *J Comp Neurol* **525**, 3563-3578, doi:10.1002/cne.24291 (2017).
100 Concordet, J. P. & Haeussler, M. CRISPOR: intuitive guide selection for CRISPR/Cas9 genome editing experiments and screens. *Nucleic Acids Res* **46**, W242-W245, doi:10.1093/nar/gky354 (2018).
101 Chan, K. Y. *et al.* Engineered AAVs for efficient noninvasive gene delivery to the central and peripheral nervous systems. *Nat Neurosci* **20**, 1172-1179, doi:10.1038/nn.4593 (2017).
102 Schwammle, V., Hagensen, C. E., Rogowska-Wrzesinska, A. & Jensen, O. N. PolySTest: Robust Statistical Testing of Proteomics Data with Missing Values Improves Detection of Biologically Relevant Features. *Mol Cell Proteomics* **19**, 1396-1408, doi:10.1074/mcp.RA119.001777 (2020).

1542 103 Hallett, P. J., Collins, T. L., Standaert, D. G. & Dunah, A. W. Biochemical fractionation
1543 of brain tissue for studies of receptor distribution and trafficking. *Curr Protoc Neurosci*
1544 **Chapter 1**, Unit 1 16, doi:10.1002/0471142301.ns0116s42 (2008).
1545 104 Shannon, P. *et al.* Cytoscape: a software environment for integrated models of
1546 biomolecular interaction networks. *Genome Res* **13**, 2498-2504, doi:10.1101/gr.1239303
1547 (2003).
1548 105 Ge, S. X., Jung, D. & Yao, R. ShinyGO: a graphical gene-set enrichment tool for animals
1549 and plants. *Bioinformatics* **36**, 2628-2629, doi:10.1093/bioinformatics/btz931 (2020).
1550 106 Koopmans, F. *et al.* SynGO: An Evidence-Based, Expert-Curated Knowledge Base for
1551 the Synapse. *Neuron* **103**, 217-234 e214, doi:10.1016/j.neuron.2019.05.002 (2019).
1552 107 de Leeuw, C. A., Mooij, J. M., Heskes, T. & Posthuma, D. MAGMA: generalized gene-
1553 set analysis of GWAS data. *PLoS Comput Biol* **11**, e1004219,
1554 doi:10.1371/journal.pcbi.1004219 (2015).
1555 108 Schindelin, J. *et al.* Fiji: an open-source platform for biological-image analysis. *Nat*
1556 *Methods* **9**, 676-682, doi:10.1038/nmeth.2019 (2012).
1557 109 Sanson, K. R. *et al.* Optimized libraries for CRISPR-Cas9 genetic screens with multiple
1558 modalities. *Nat Commun* **9**, 5416, doi:10.1038/s41467-018-07901-8 (2018).
1559 110 Schmidt, R. *et al.* CRISPR activation and interference screens decode stimulation
1560 responses in primary human T cells. *Science* **375**, eabj4008, doi:10.1126/science.abj4008
1561 (2022).
1562 111 Gordon, M. G. *et al.* lentiMPRA and MPRAflow for high-throughput functional
1563 characterization of gene regulatory elements. *Nat Protoc* **15**, 2387-2412,
1564 doi:10.1038/s41596-020-0333-5 (2020).
1565 112 Wang, X. *et al.* Synaptic dysfunction and abnormal behaviors in mice lacking major
1566 isoforms of Shank3. *Hum Mol Genet* **20**, 3093-3108, doi:10.1093/hmg/ddr212 (2011).
1567 113 Pappas, A. L. *et al.* Deficiency of Shank2 causes mania-like behavior that responds to
1568 mood stabilizers. *JCI Insight* **2**, doi:10.1172/jci.insight.92052 (2017).
1569 114 Rodriguiz, R. M., Chu, R., Caron, M. G. & Wetsel, W. C. Aberrant responses in social
1570 interaction of dopamine transporter knockout mice. *Behav Brain Res* **148**, 185-198,
1571 doi:10.1016/s0166-4328(03)00187-6 (2004).
1572 115 Nehrenberg, D. L. *et al.* An anxiety-like phenotype in mice selectively bred for
1573 aggression. *Behav Brain Res* **201**, 179-191, doi:10.1016/j.bbr.2009.02.010 (2009).
1574

Figure 1

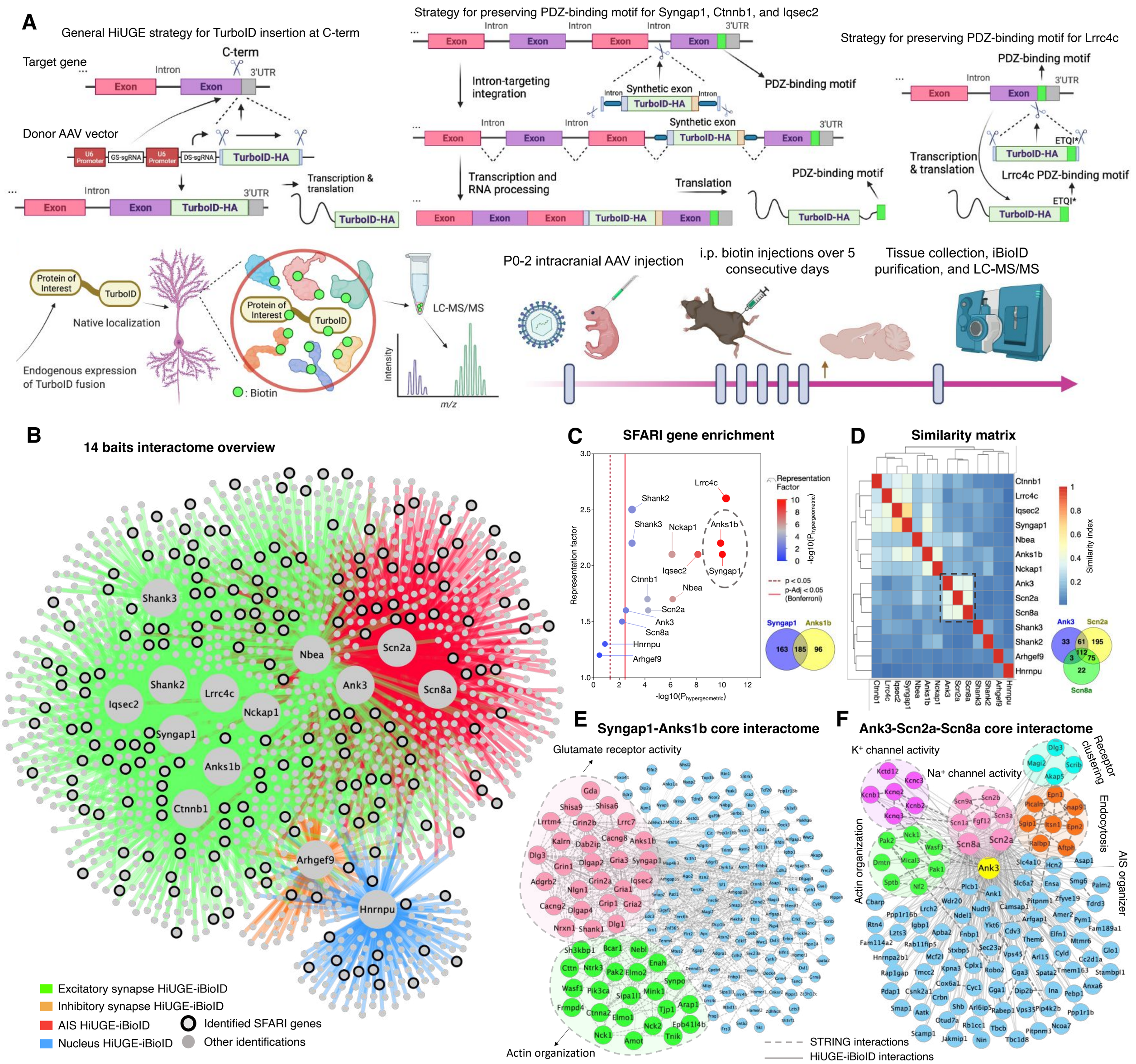
A
General HiUGE strategy for TurboID insertion at C-term
Target gene
C-term
Intron
3'UTR
Exon
Donor AAV vector
U6 Promoter
GS-sgRNA
DS-sgRNA
TurboID-HA
Transcription & translation
Strategy for preserving PDZ-binding motif for Syngap1, Ctnnb1, and Iqsec2
Intron-targeting integration
Synthetic exon
PDZ-binding motif
Transcription and RNA processing
Translation
Strategy for preserving PDZ-binding motif for Lrrc4c
ETQI*
Lrrc4c PDZ-binding motif
Protein of Interest
TurboID
Native localization
Endogenous expression of TurboID fusion
: Biotin
LC-MS/MS
Intensity
m/z
P0-2 intracranial AAV injection
i.p. biotin injections over 5 consecutive days
Tissue collection, iBioID purification, and LC-MS/MS
B
14 baits interactome overview
Shank3
Nbea
Scn2a
Shank2
Lrrc4c
Ank3
Scn8a
Iqsec2
Nckap1
Syngap1
Anks1b
Ctnnb1
Arhgef9
Hnrnpu
Excitatory synapse HiUGE-iBioID
Inhibitory synapse HiUGE-iBioID
AIS HiUGE-iBioID
Nucleus HiUGE-iBioID
Identified SFARI genes
Other identifications
C
SFARI gene enrichment
Representation factor
-log10(P hypergeometric)
Representation Factor
p < 0.05
p-Adj < 0.05 (Bonferroni)
Syngap1
Anks1b
163
185
96
D
Similarity matrix
Similarity index
Ank3
Scn2a
Scn8a
33
61
195
112
3
75
22
E
Syngap1-Anks1b core interactome
Glutamate receptor activity
Actin organization
F
Ank3-Scn2a-Scn8a core interactome
K+ channel activity
Na+ channel activity
Receptor clustering
Endocytosis
AIS organizer
Actin organization
STRING interactions
HiUGE-iBioID interactions

Figure 2

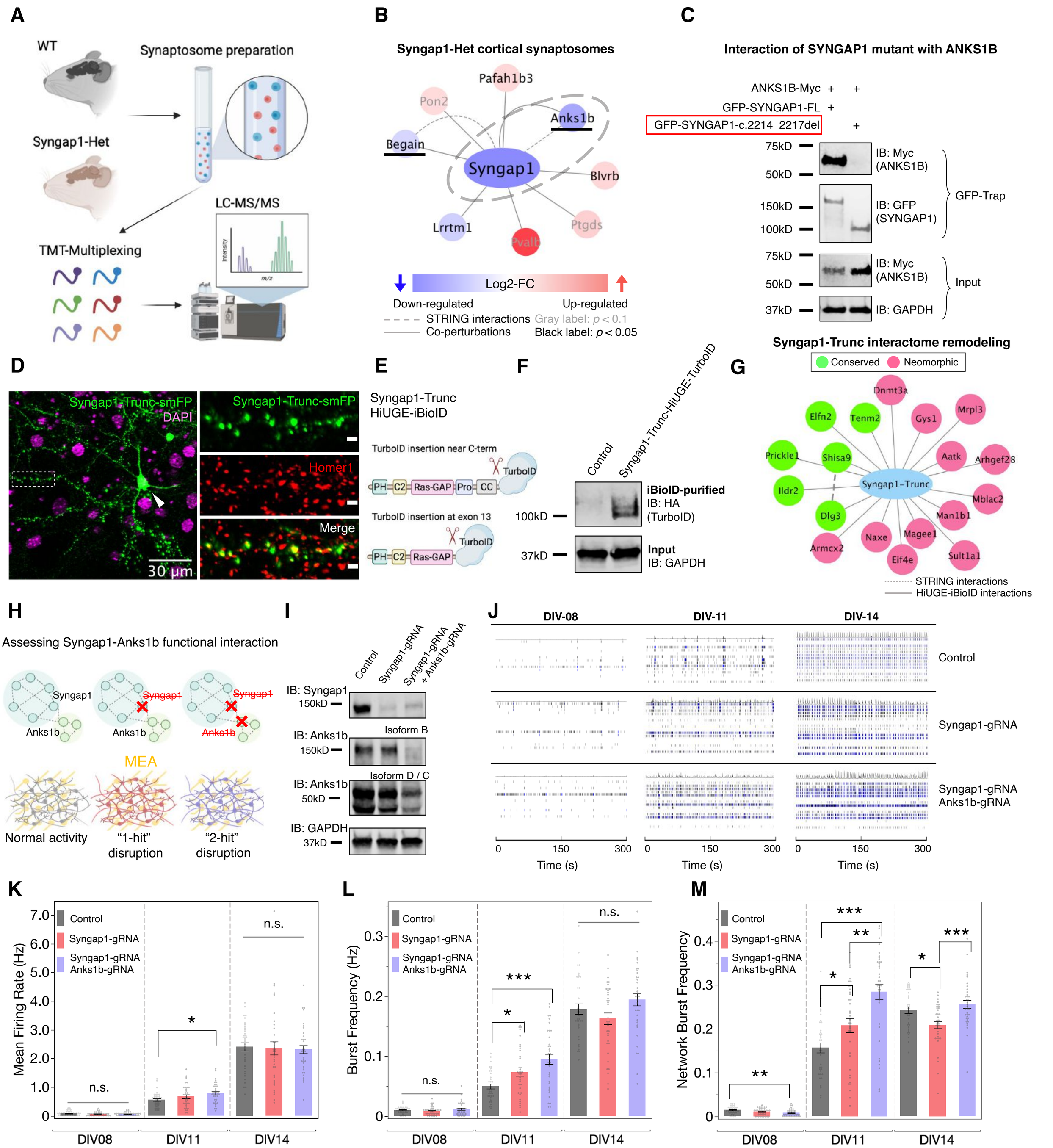
A
WT
Synaptosome preparation
Syngap1-Het
LC-MS/MS
TMT-Multiplexing
B
Syngap1-Het cortical synaptosomes
Pafah1b3
Pon2
Anks1b
Begain
Syngap1
Blvrb
Lrrtm1
Pvalb
Ptgds
Log2-FC
Down-regulated
Up-regulated
STRING interactions
Co-perturbations
Gray label: p < 0.1
Black label: p < 0.05
C
Interaction of SYNGAP1 mutant with ANKS1B
ANKS1B-Myc
GFP-SYNGAP1-FL
GFP-SYNGAP1-c.2214_2217del
75kD
50kD
150kD
100kD
37kD
IB: Myc (ANKS1B)
IB: GFP (SYNGAP1)
IB: GAPDH
GFP-Trap
Input
D
Syngap1-Trunc-smFP
DAPI
Homer1
Merge
30 µm
E
Syngap1-Trunc HiUGE-iBioID
TurboID insertion near C-term
TurboID
PH
C2
Ras-GAP
Pro
CC
TurboID insertion at exon 13
F
Control
Syngap1-Trunc-HiUGE-TurboID
iBioID-purified
IB: HA (TurboID)
Input
IB: GAPDH
G
Syngap1-Trunc interactome remodeling
Conserved
Neomorphic
Dnmt3a
Elfn2
Tenm2
Gys1
Mrpl3
Prickle1
Shisa9
Aatk
Arhgef28
Ildr2
Syngap1-Trunc
Mblac2
Dlg3
Man1b1
Naxe
Magee1
Armcx2
Eif4e
Sult1a1
STRING interactions
HiUGE-iBioID interactions
H
Assessing Syngap1-Anks1b functional interaction
Syngap1
Anks1b
MEA
Normal activity
"1-hit" disruption
"2-hit" disruption
I
Control
Syngap1-gRNA
Syngap1-gRNA + Anks1b-gRNA
IB: Syngap1
150kD
IB: Anks1b
Isoform B
Isoform D / C
50kD
IB: GAPDH
37kD
J
DIV-08
DIV-11
DIV-14
Control
Syngap1-gRNA
Syngap1-gRNA Anks1b-gRNA
0
150
300
Time (s)
K
Mean Firing Rate (Hz)
Control
Syngap1-gRNA
Syngap1-gRNA Anks1b-gRNA
n.s.
*
DIV08
DIV11
DIV14
L
Burst Frequency (Hz)
***
M
Network Burst Frequency
**

Figure 3

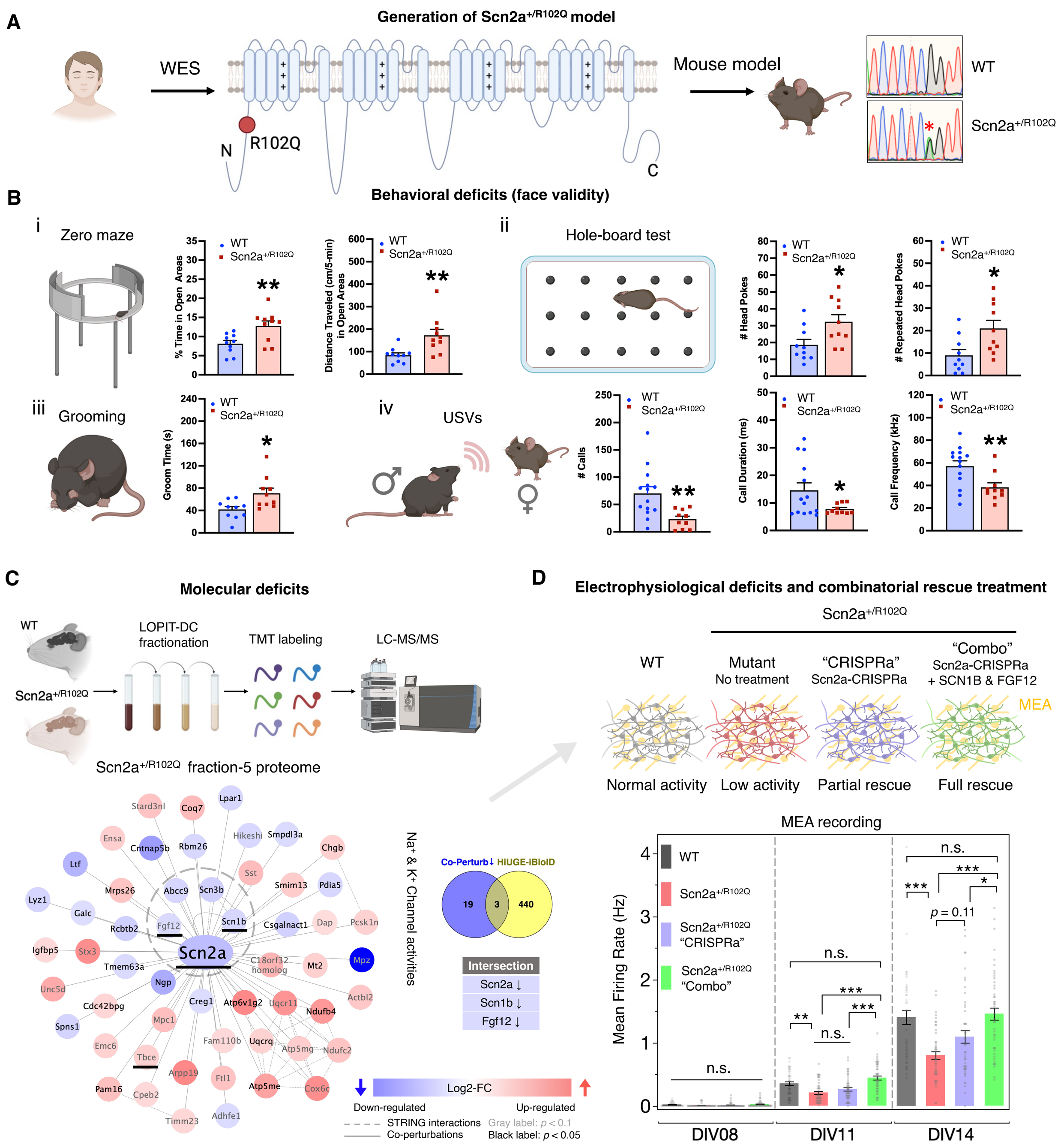
A
Generation of Scn2a+/R102Q model
WES
R102Q
N
C
Mouse model
WT
Scn2a+/R102Q
B
Behavioral deficits (face validity)
i
Zero maze
% Time in Open Areas
Distance Traveled (cm/5-min) in Open Areas
ii
Hole-board test
Head Pokes
Repeated Head Pokes
iii
Grooming
Groom Time (s)
iv
USVs
Calls
Call Duration (ms)
Call Frequency (kHz)
WT
Scn2a+/R102Q
C
Molecular deficits
LOPIT-DC fractionation
TMT labeling
LC-MS/MS
Scn2a+/R102Q fraction-5 proteome
Scn2a
Na+ & K+ Channel activities
Co-Perturb↓ HiUGE-iBioID
19
3
440
Intersection
Scn2a ↓
Scn1b ↓
Fgf12 ↓
Log2-FC
Down-regulated
Up-regulated
STRING interactions
Co-perturbations
Gray label: p < 0.1
Black label: p < 0.05
D
Electrophysiological deficits and combinatorial rescue treatment
Scn2a+/R102Q
WT
Mutant
No treatment
"CRISPRa"
Scn2a-CRISPRa
"Combo"
Scn2a-CRISPRa
+ SCN1B & FGF12
MEA
Normal activity
Low activity
Partial rescue
Full rescue
MEA recording
Mean Firing Rate (Hz)
Scn2a+/R102Q "CRISPRa"
Scn2a+/R102Q "Combo"
n.s.
p = 0.11
DIV08
DIV11
DIV14

Supplementary Fig. S1

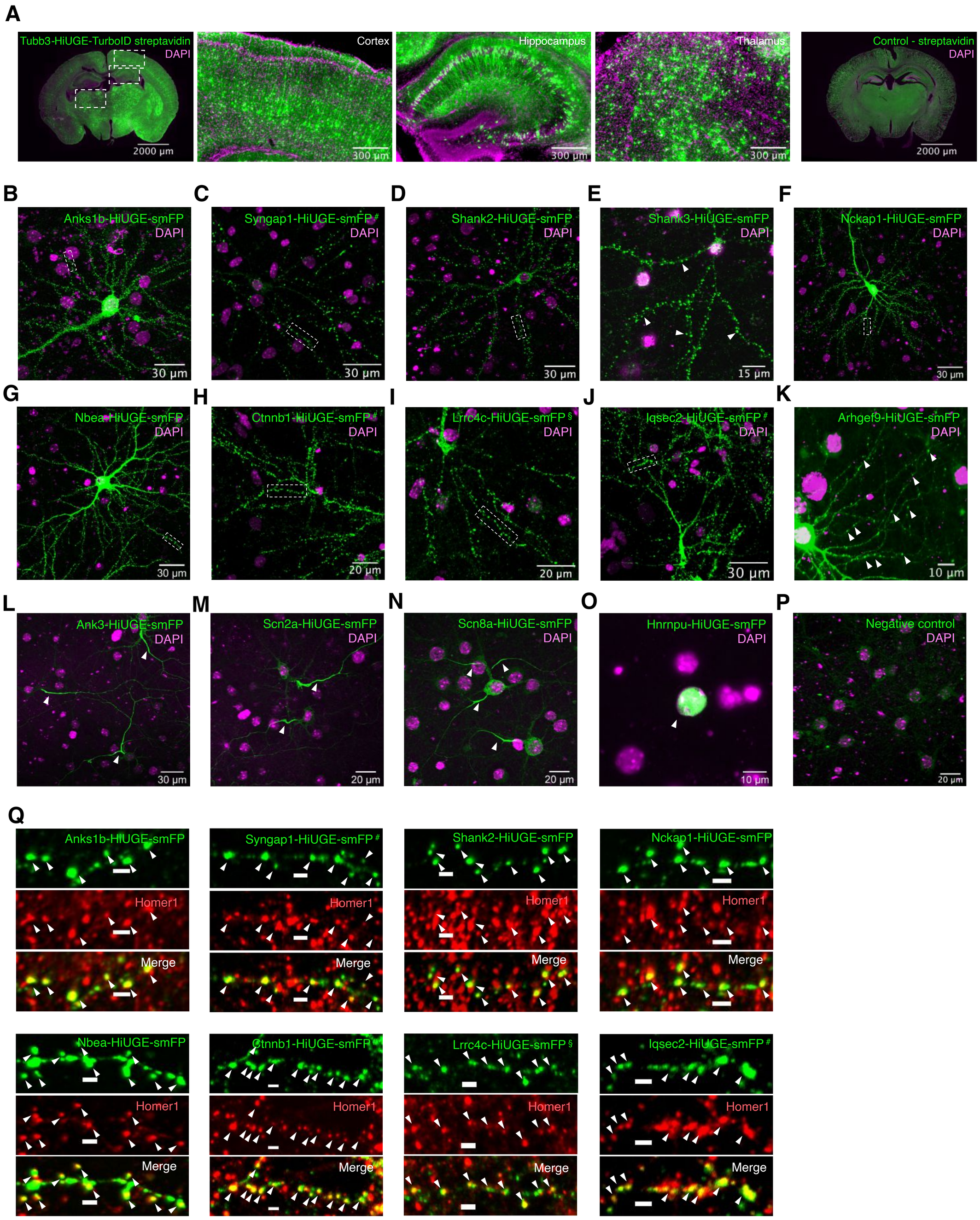

Supplementary Fig. S2

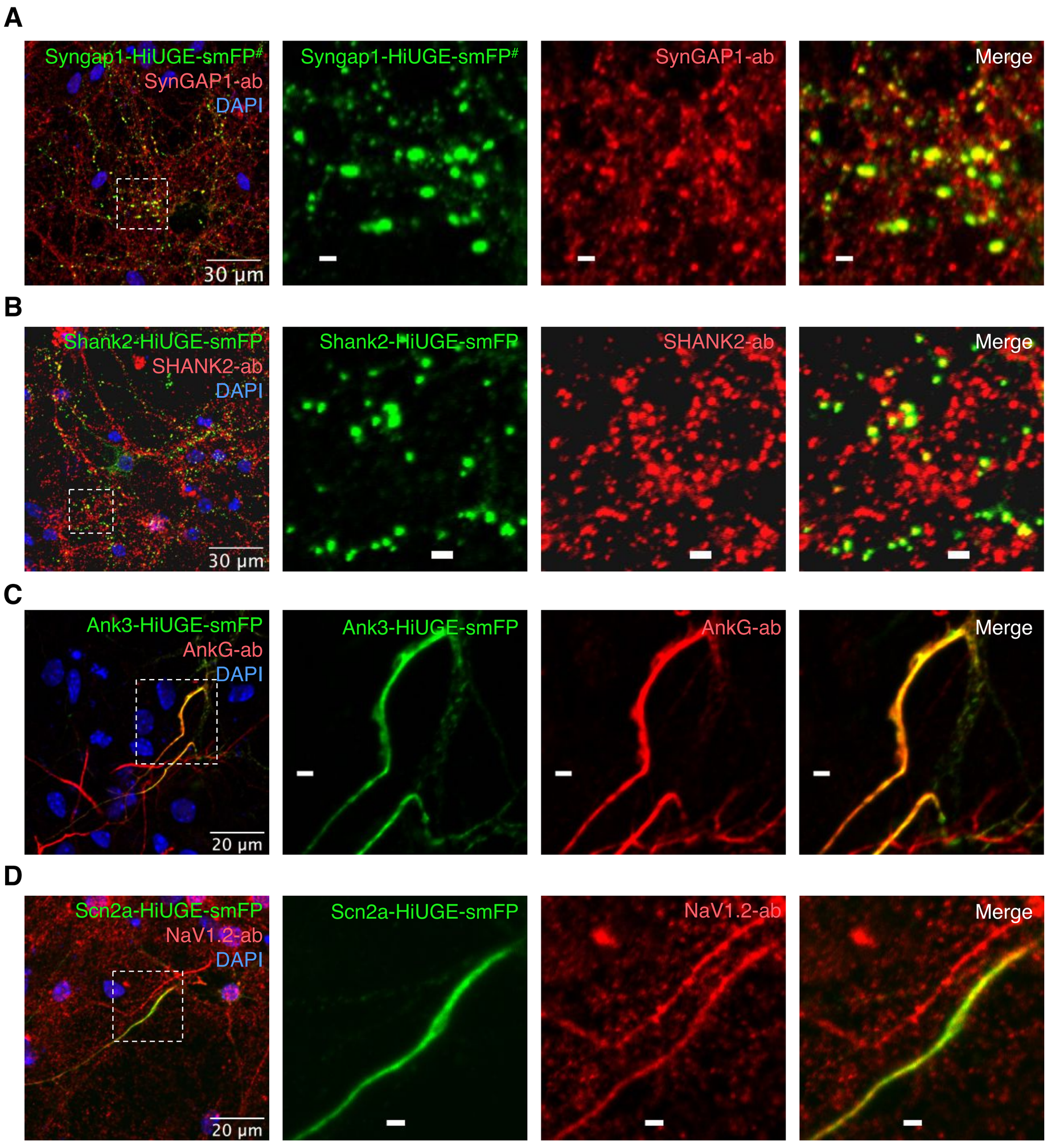

Supplementary Fig. S3

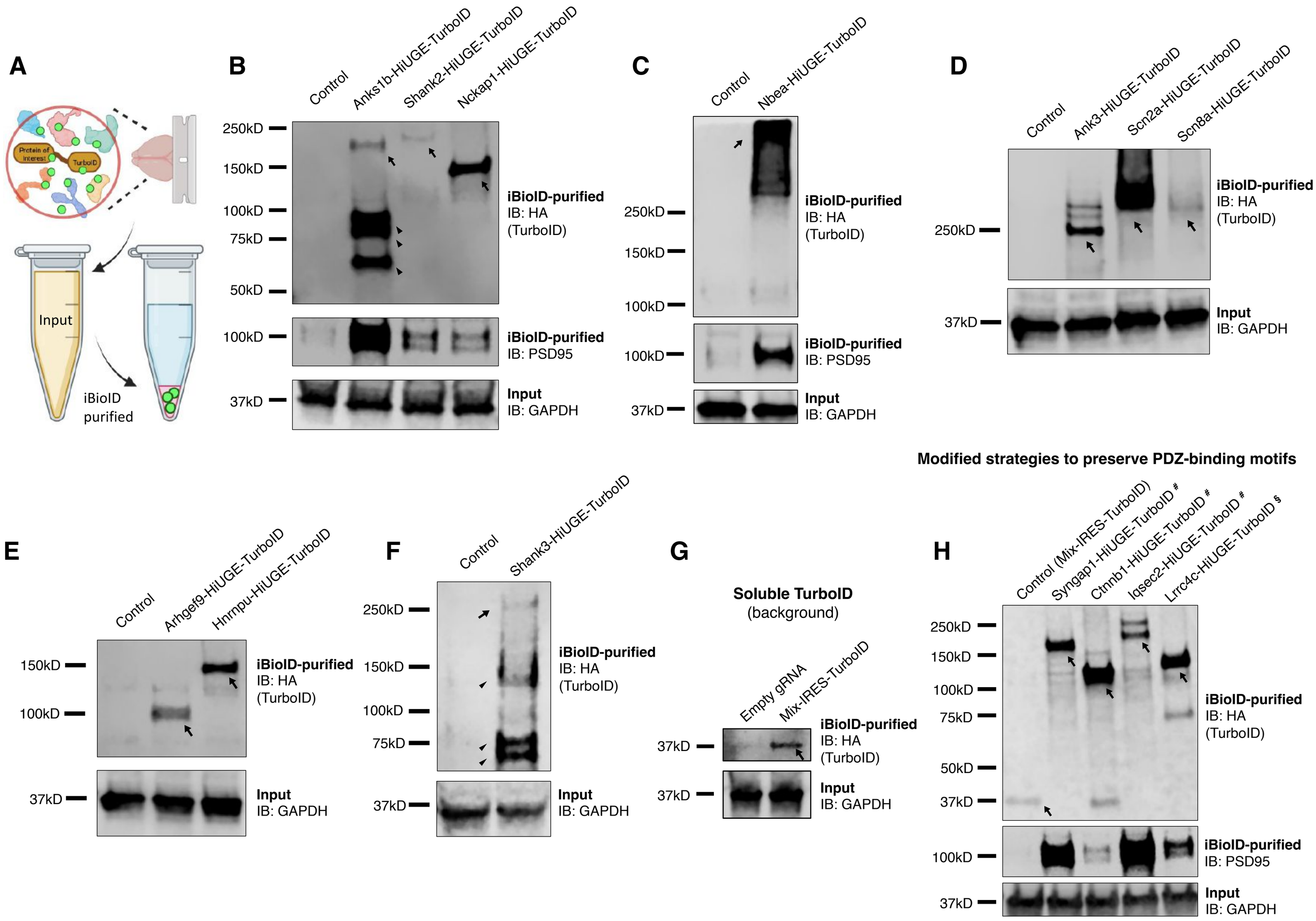

Supplementary Fig. S4

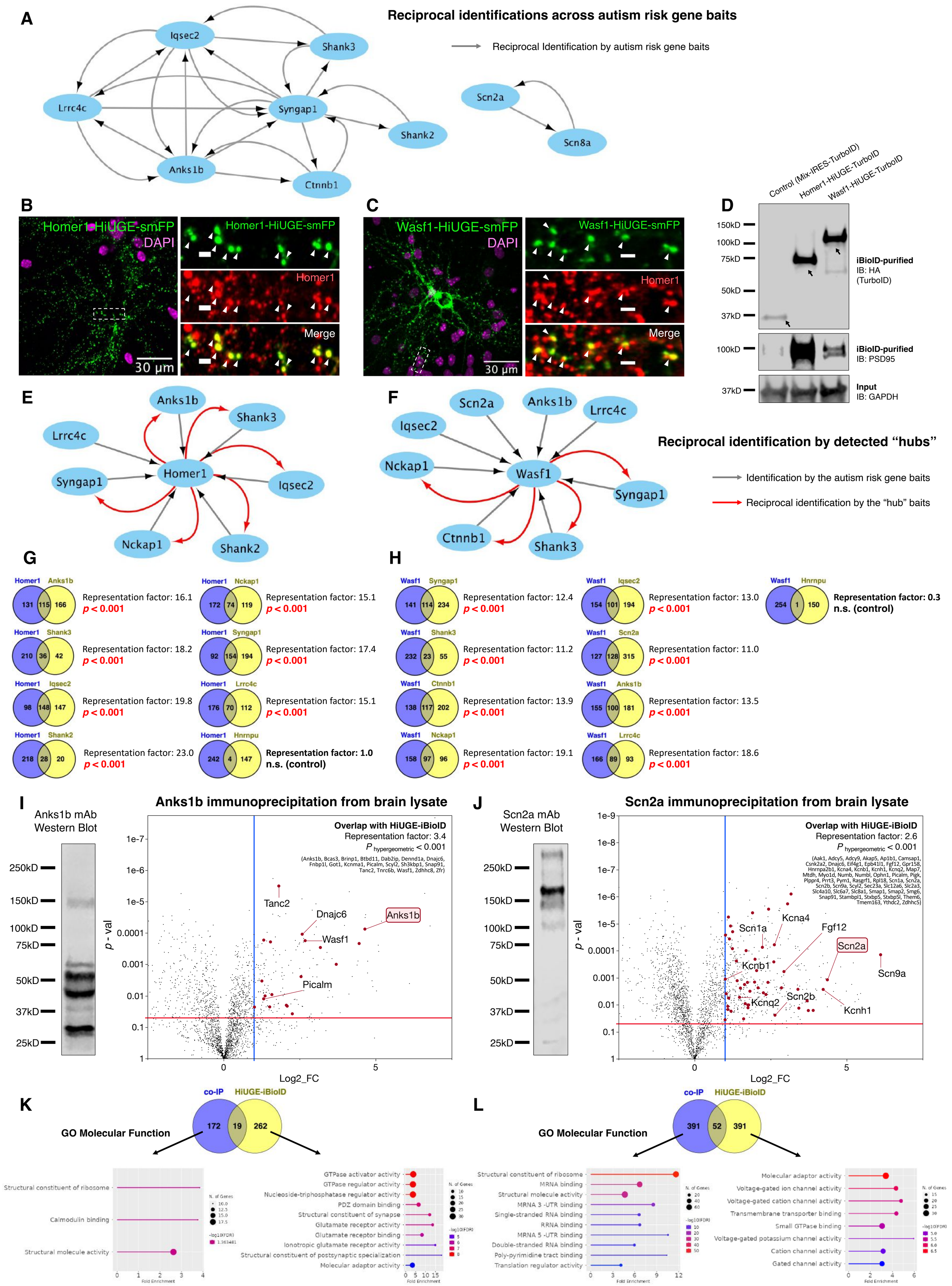

Supplementary Fig. S5

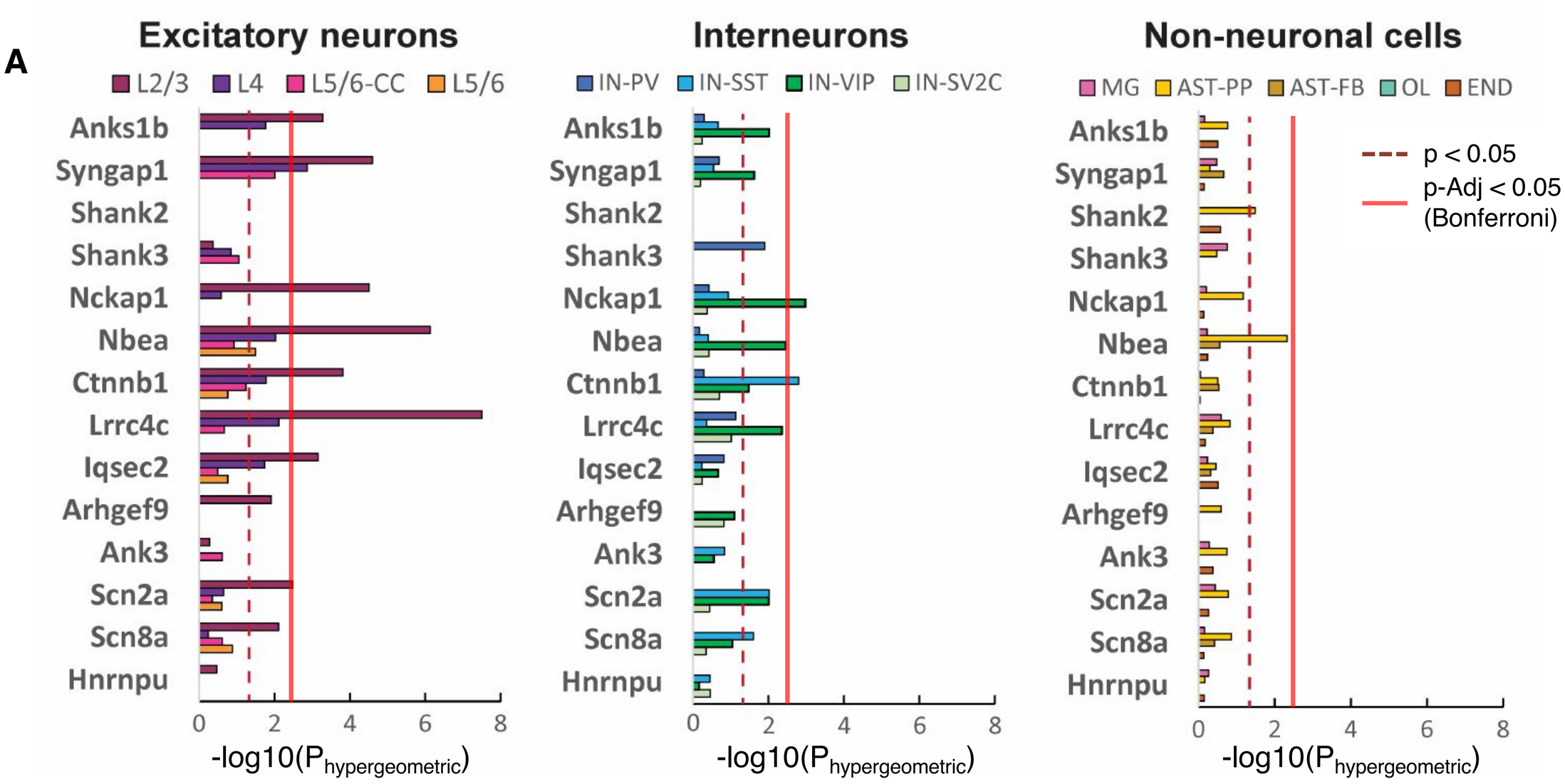

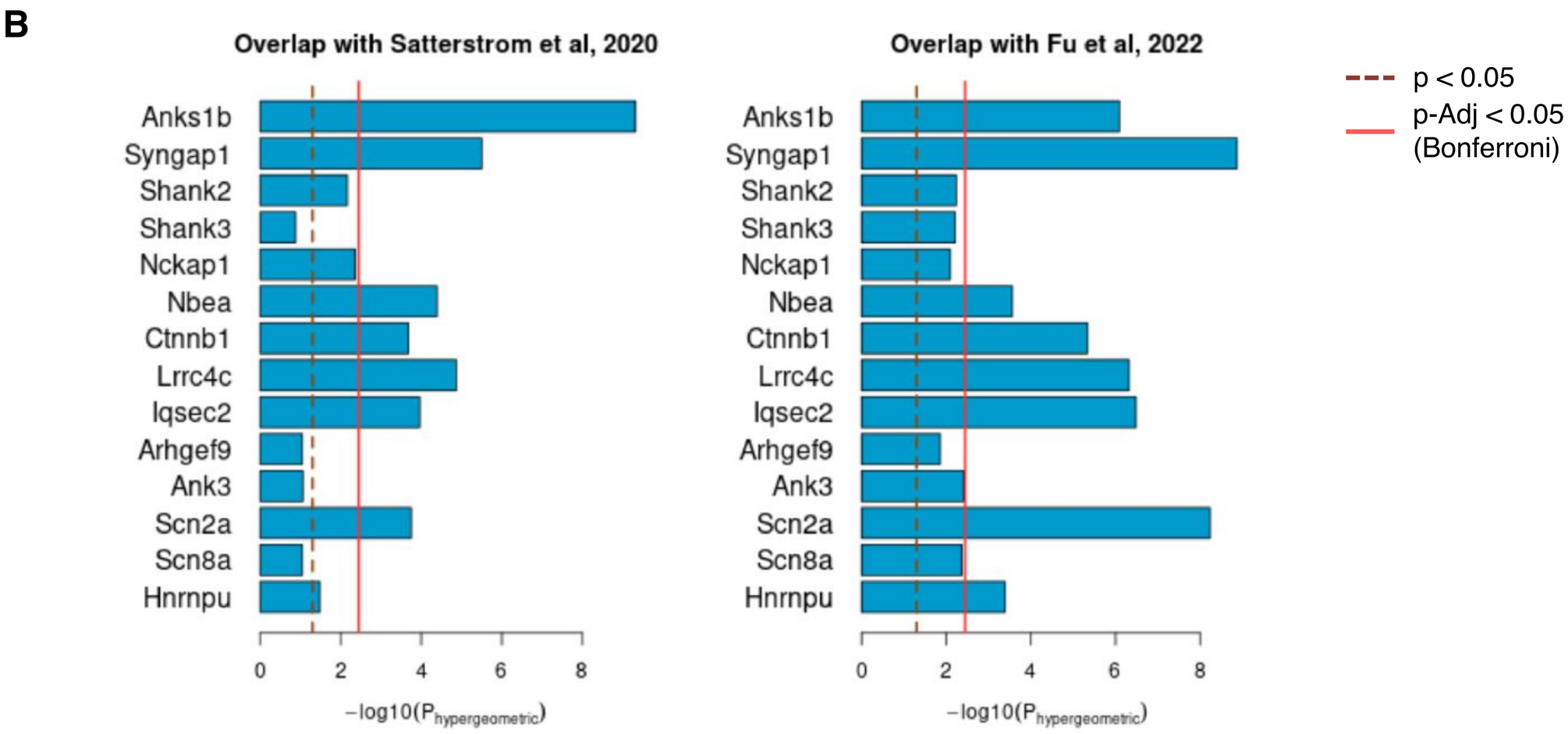

Supplementary Fig. S6

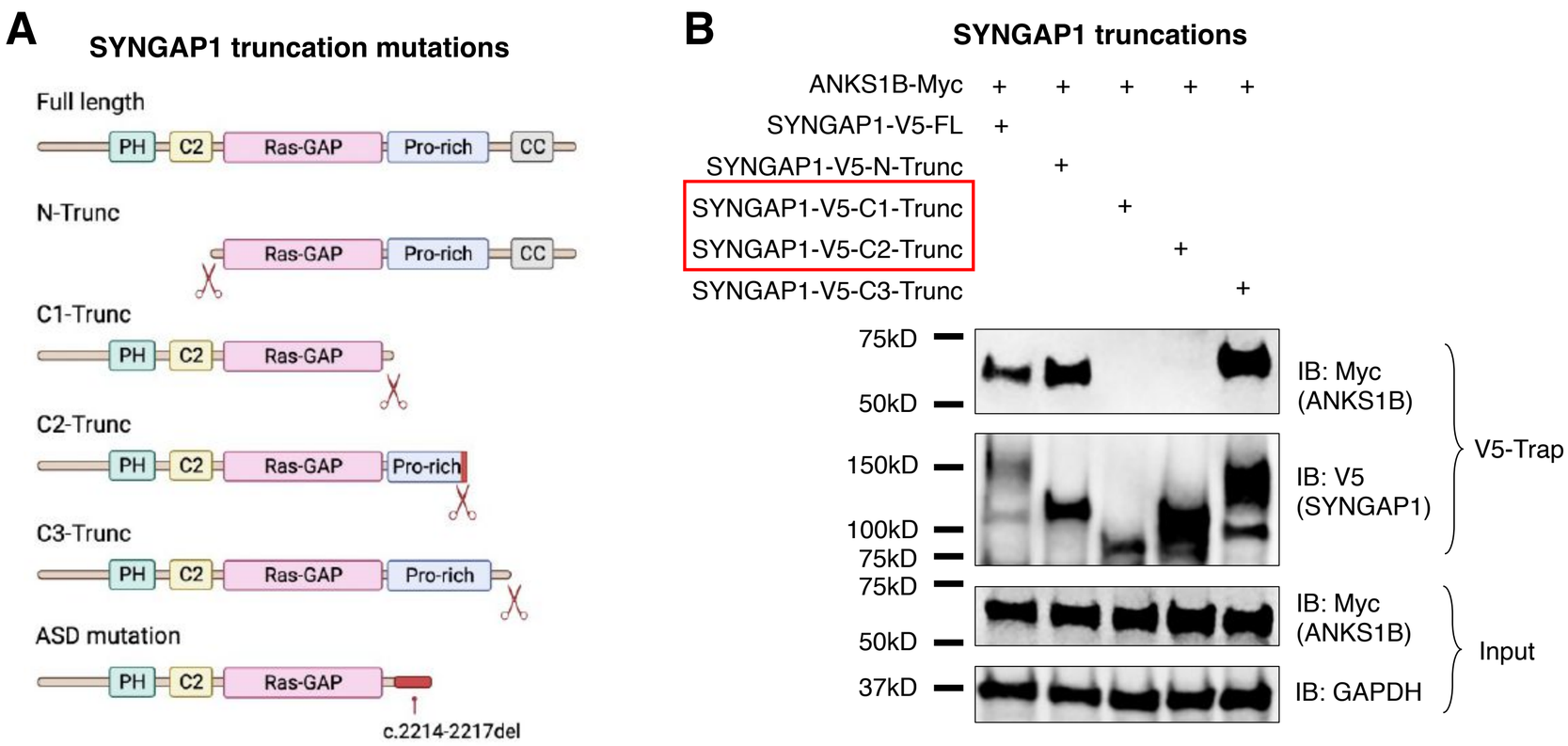

Supplementary Fig. S7

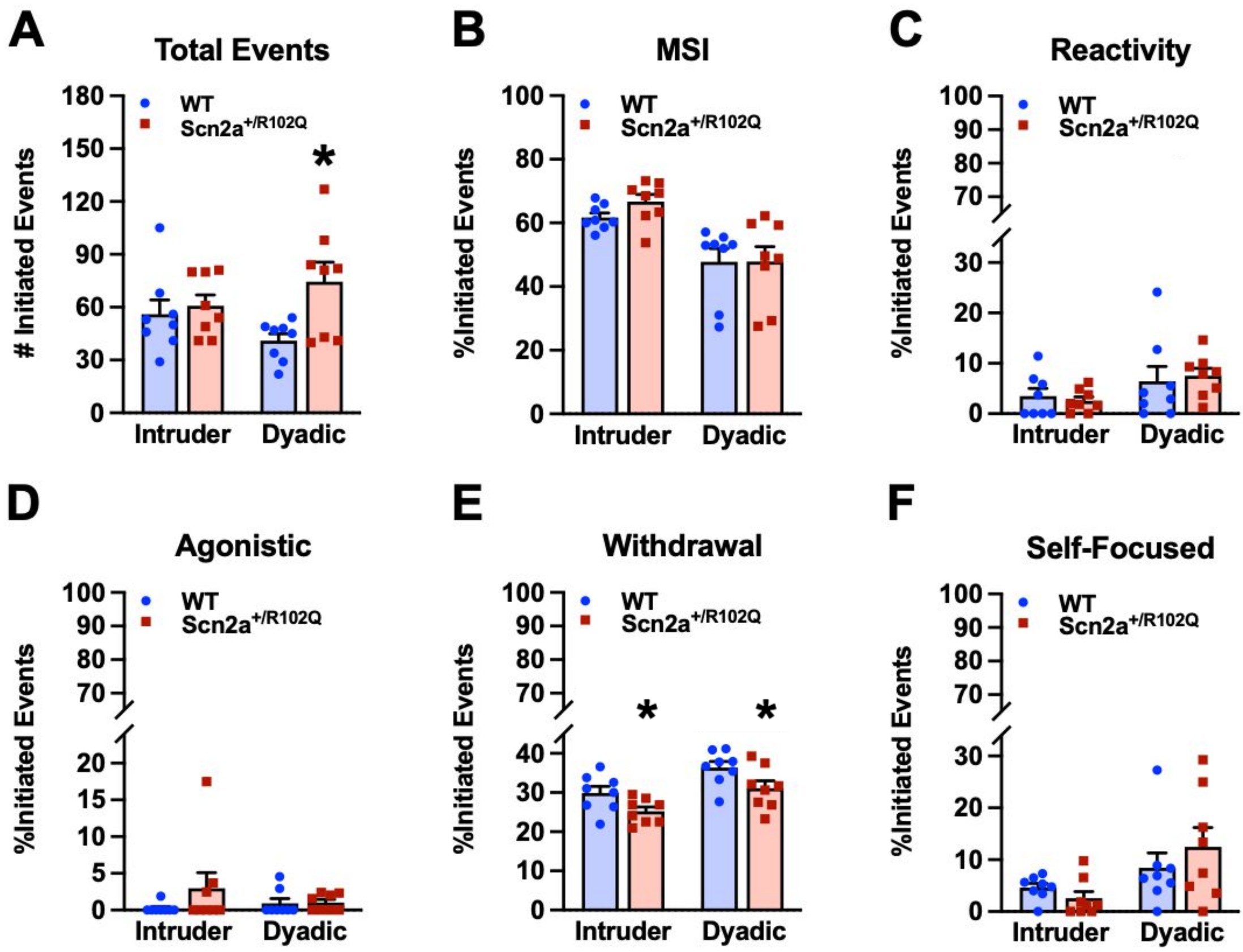

Supplementary Fig. S8

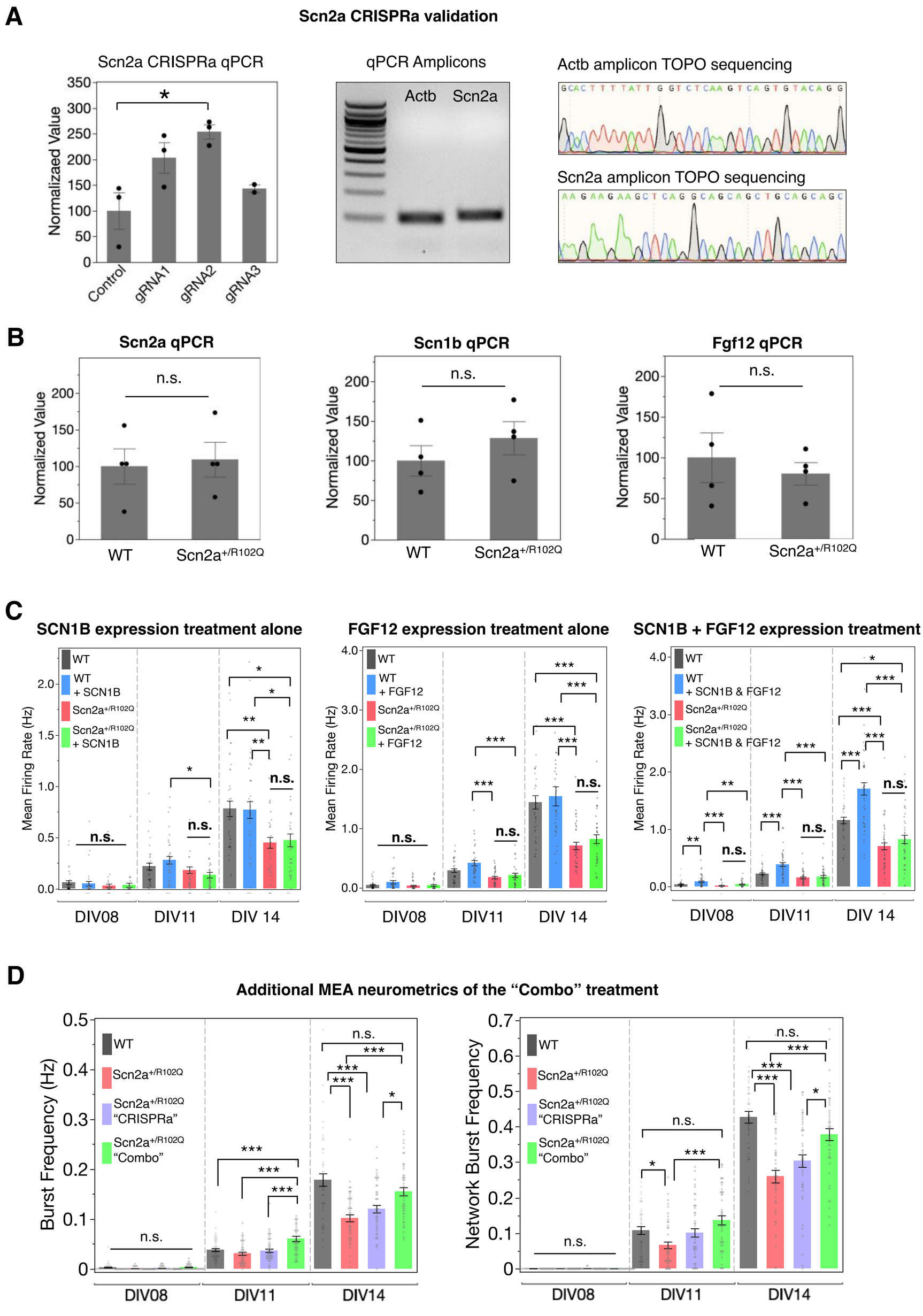

Supplementary Fig. S9

A Comparison to Pintacuda et al. (antibody-dependent immunoprecipitation in human iPSC-derived neurons)

GO Molecular Function

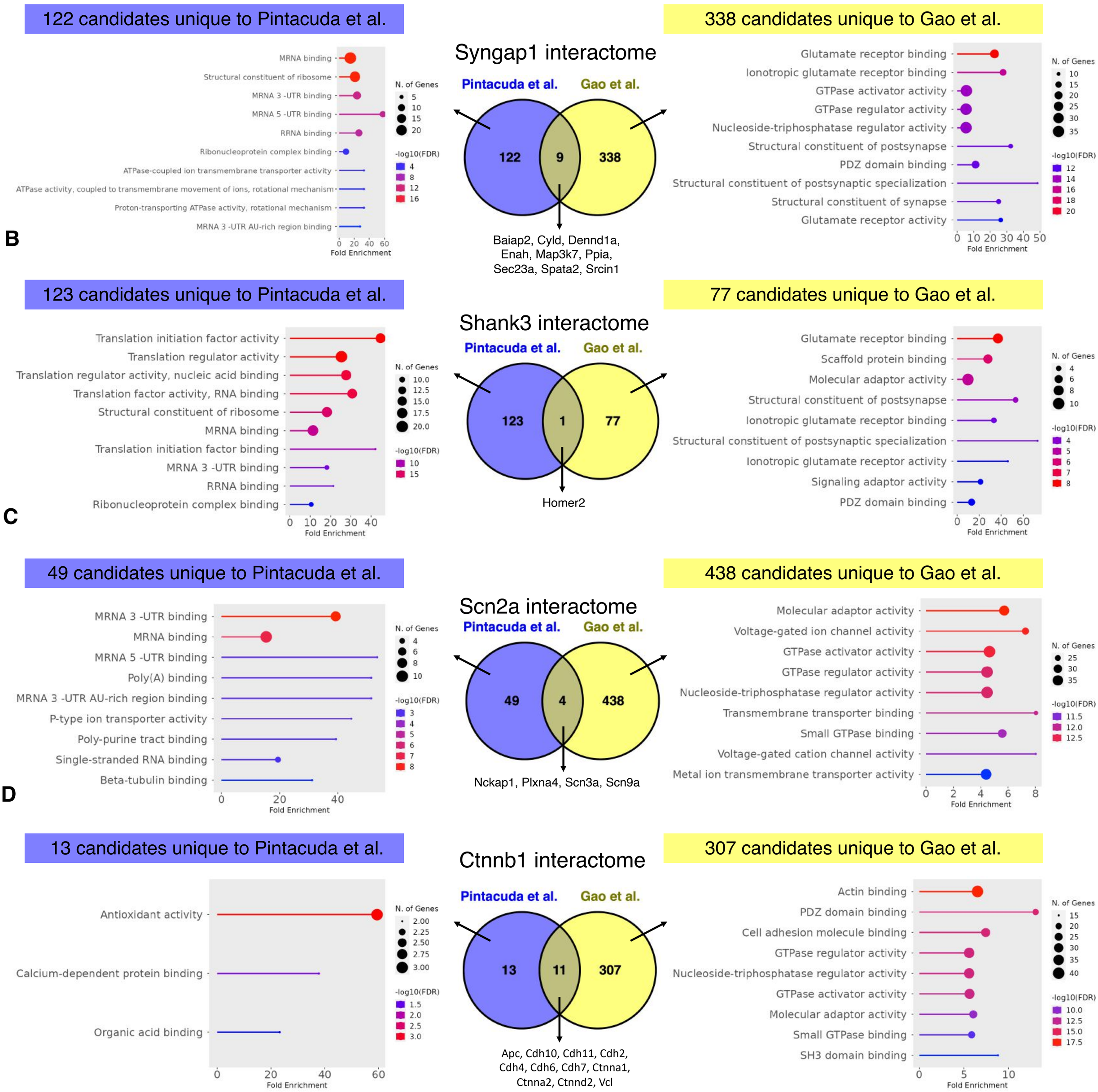

Supplementary Fig. S10

A Comparison to Murtaza et al. (lentiviral-mediated expression of BioID2 fusions in primary mouse neurons)

GO Molecular Function

90 candidates unique to Murtaza et al.

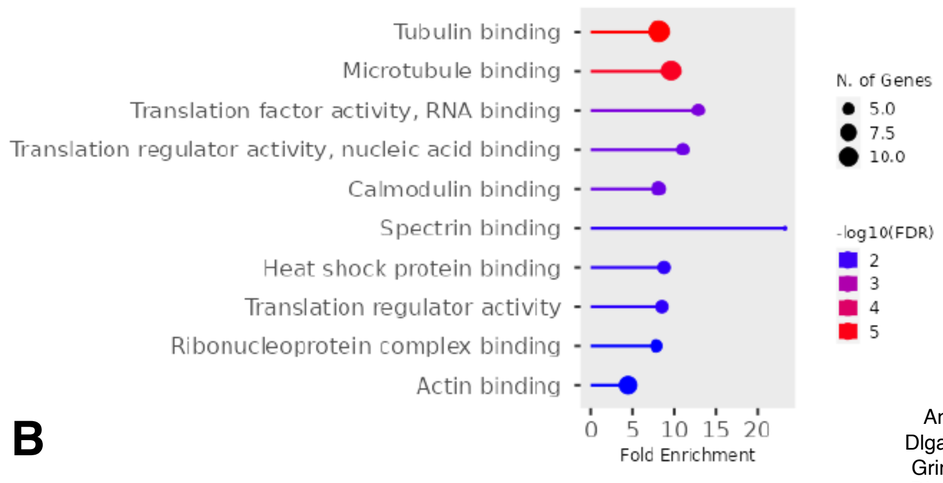

Syngap1 interactome

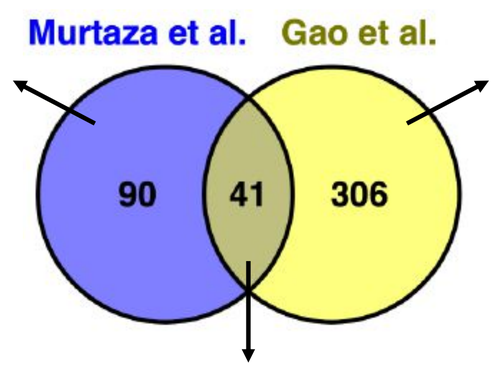

Anks1b, Sh3kbp1, Dlgap3, Dlg4, Lrrc7, Shank2, Dlg2, Grin2b, Dlgap2, Dlgap1, Peak1, Elfn1, Shank1, Begain, Dlg3, Grin1, Ppia, Grin2a, Tanc2, Prickle2, Iqsec1, Iqsec2, Shank3, Kalrn, Homer1, Dlgap4, Ablim1, Adgrl3, Arhgap39, Tnik, Sipa1l1, Mink1, Fbxo41, Dock3, Cyth2, Enah, Agap3, Adgrb3, Atxn2l, Dbnl, Nyap2

306 candidates unique to Gao et al.

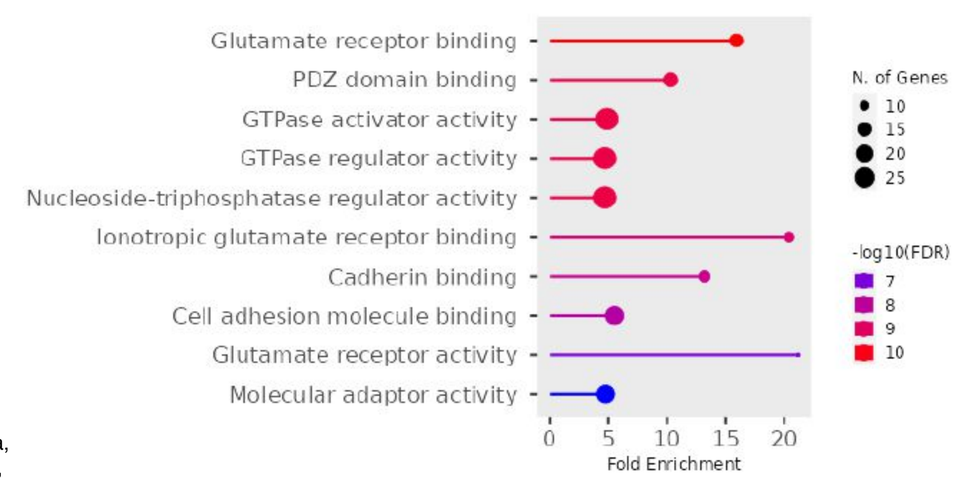

B

98 candidates unique to Murtaza et al.

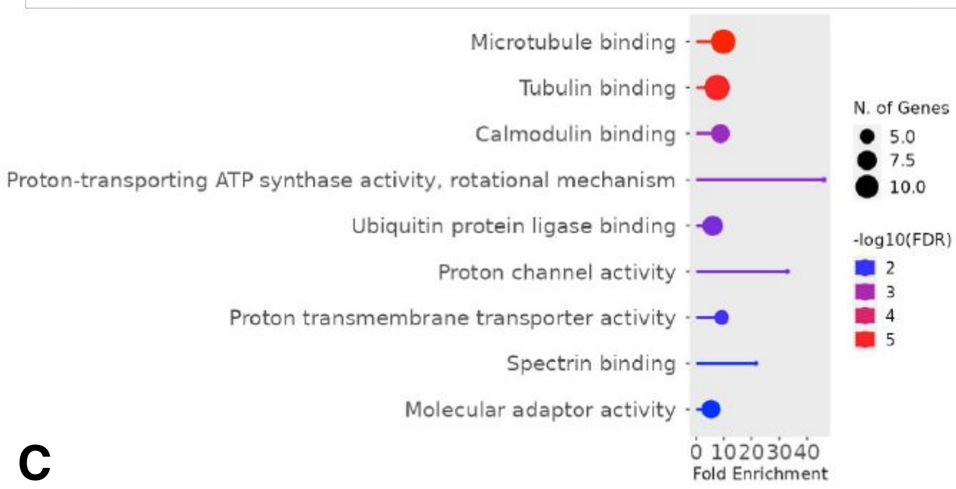

Shank3 interactome

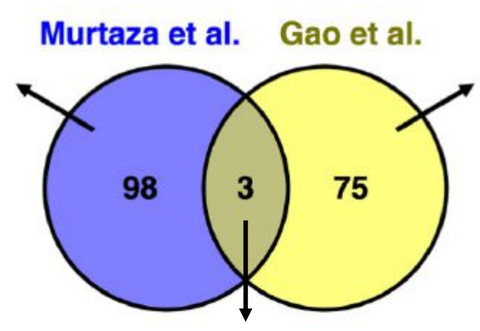

Shank1, Homer1, Dlgap3

75 candidates unique to Gao et al.

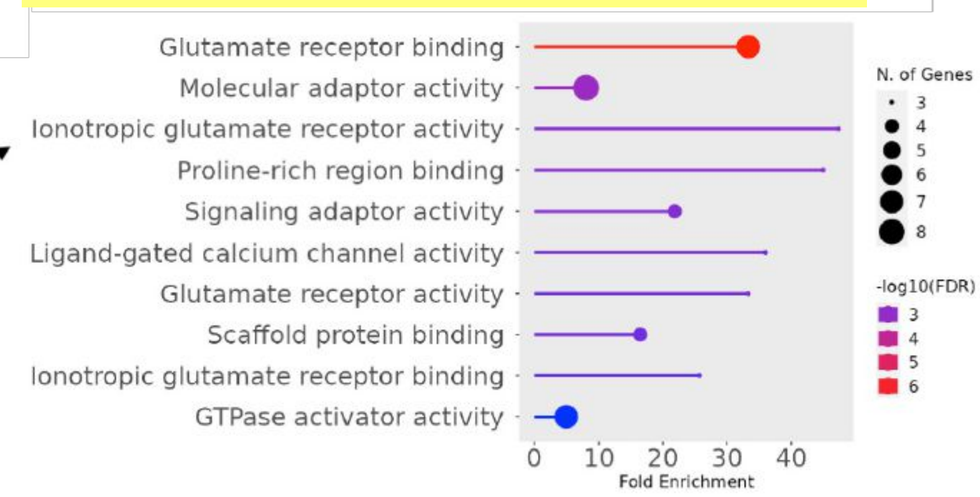

C

31 candidates unique to Murtaza et al.

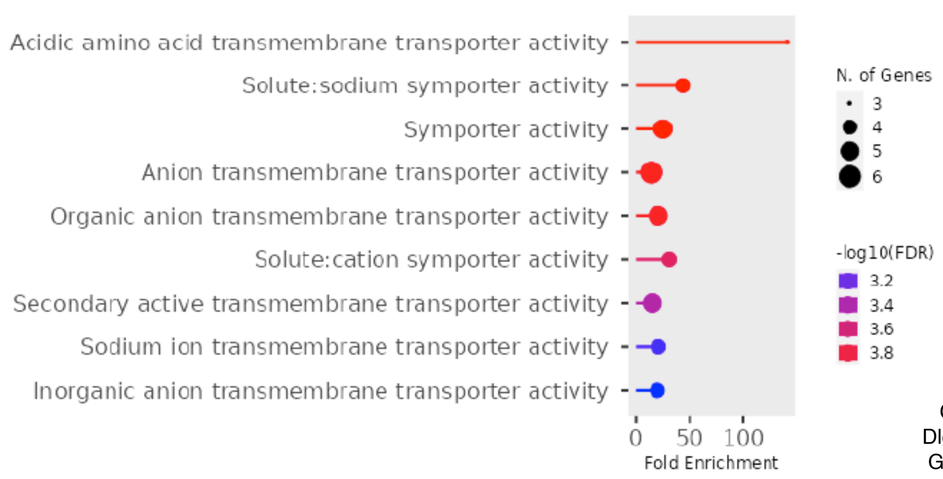

Lrrc4c interactome

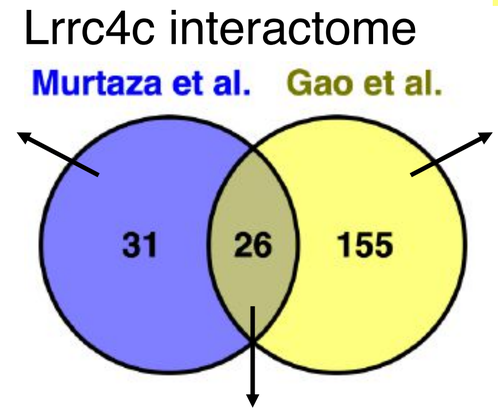

Gabrg2, Adgrb3, Dlgap4, Gabrb2, Gria1, Elfn2, Plppr4, Cxadr, Dlgap3, Gria2, Erbin, Plppr3, Slitrk5, Adgrb1, Lrrc7, Grin2b, Elfn1, Gabrb3, Abi1, Dlg2, Stx1b, Gabbr2, Dlg3, Fam171b, Dlg4, Plcb1

155 candidates unique to Gao et al.

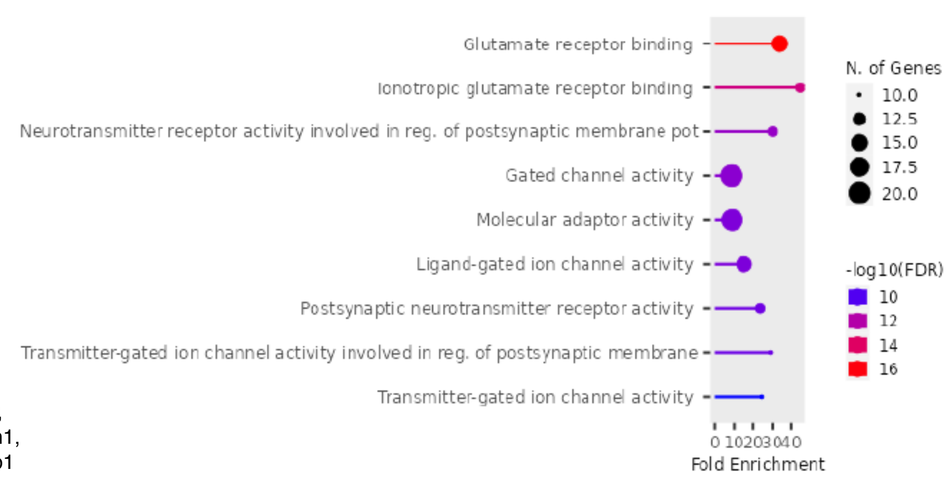

Anks1b interactome

Supplementary Fig. S11

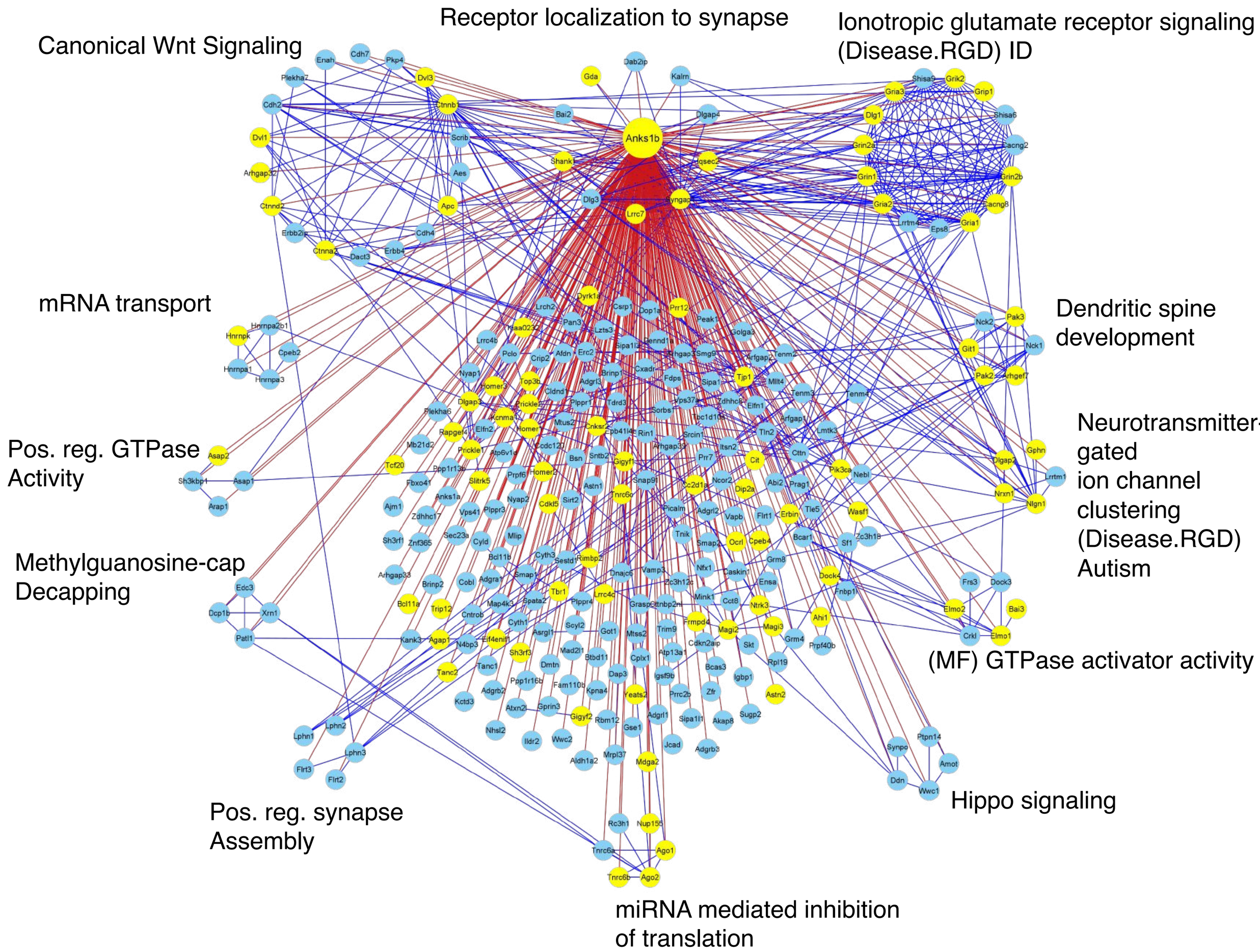

GO : Molecular Function

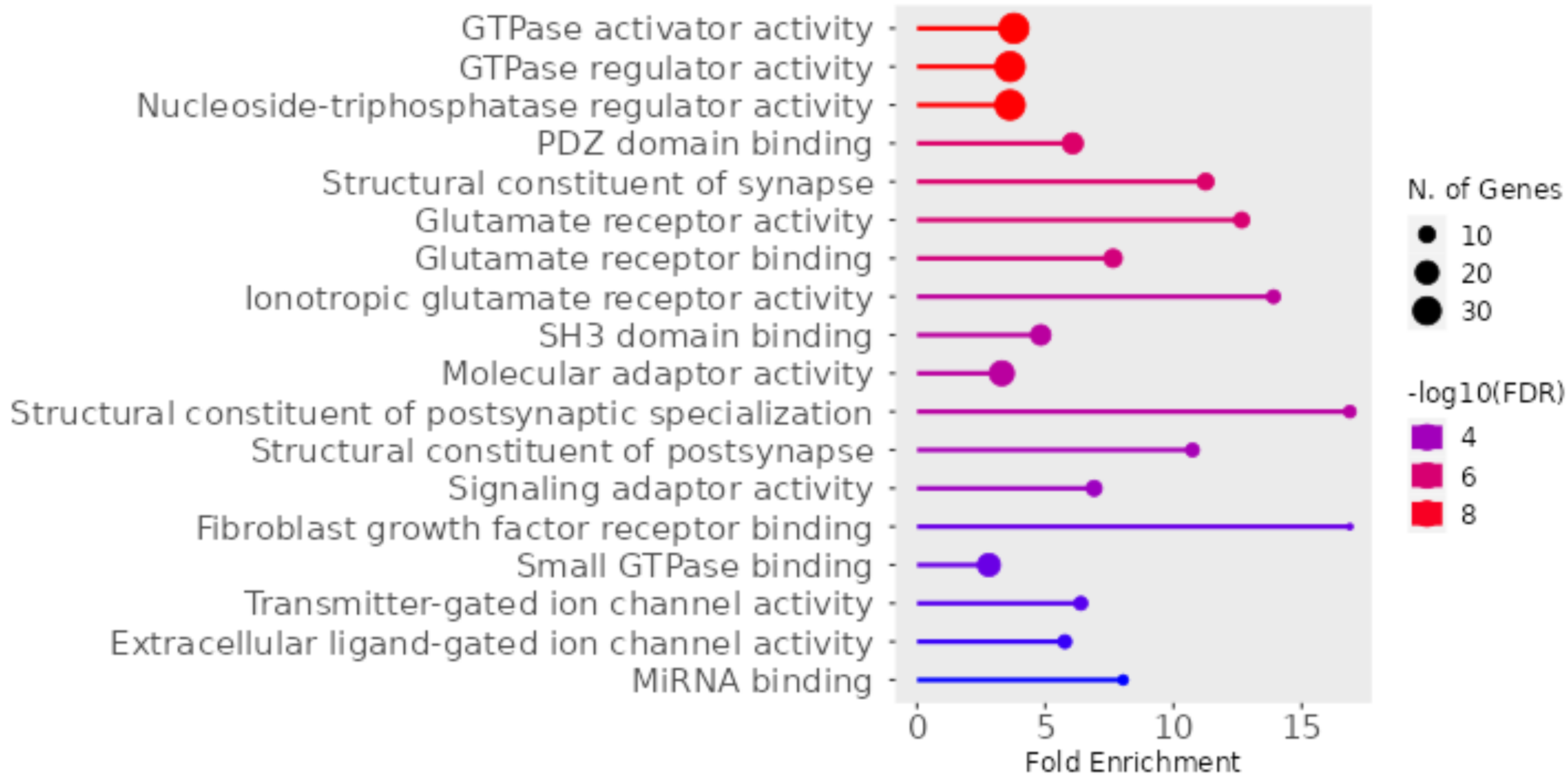

Supplementary Fig. S12

Syngap1 interactome

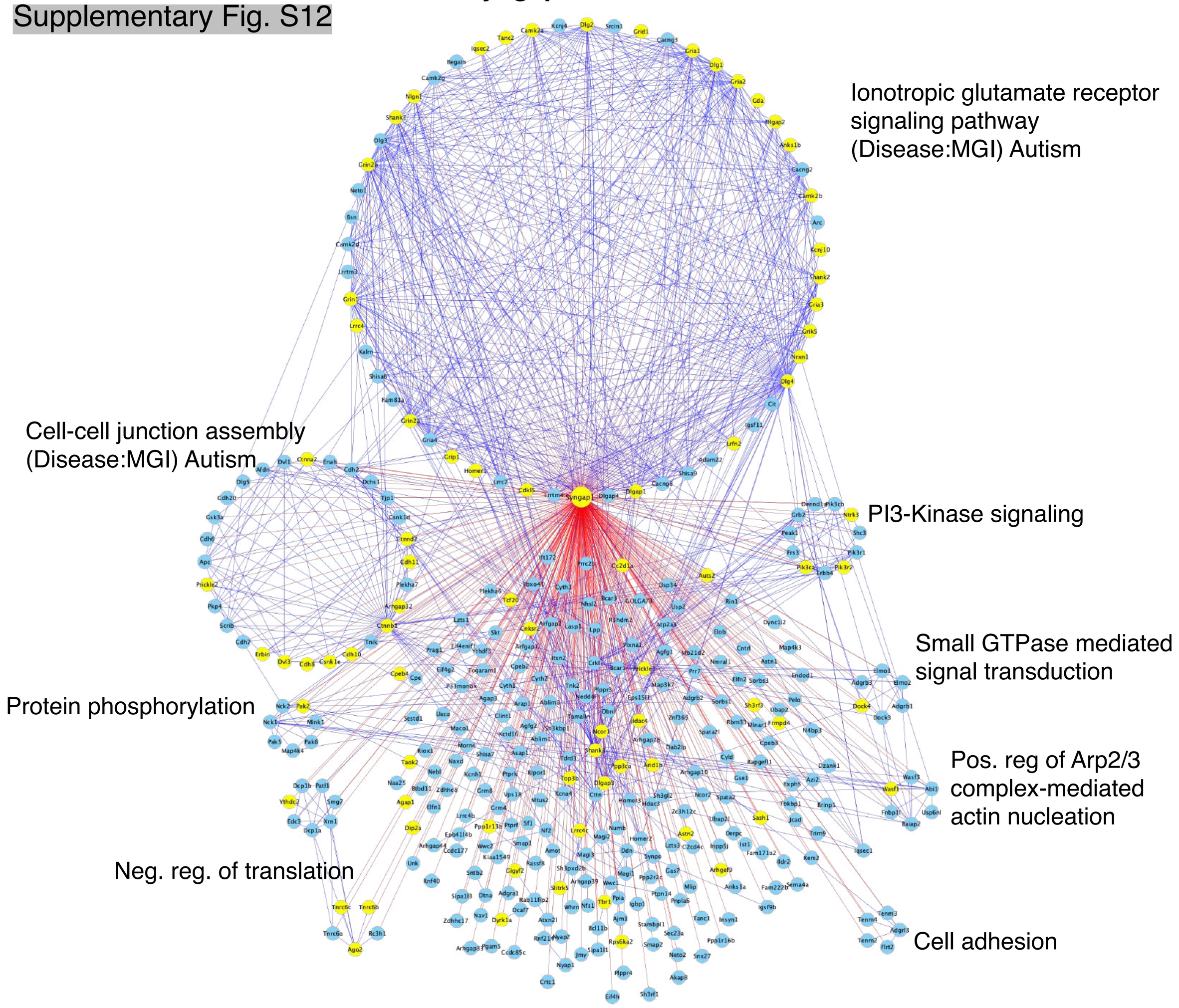

GO : Molecular Function

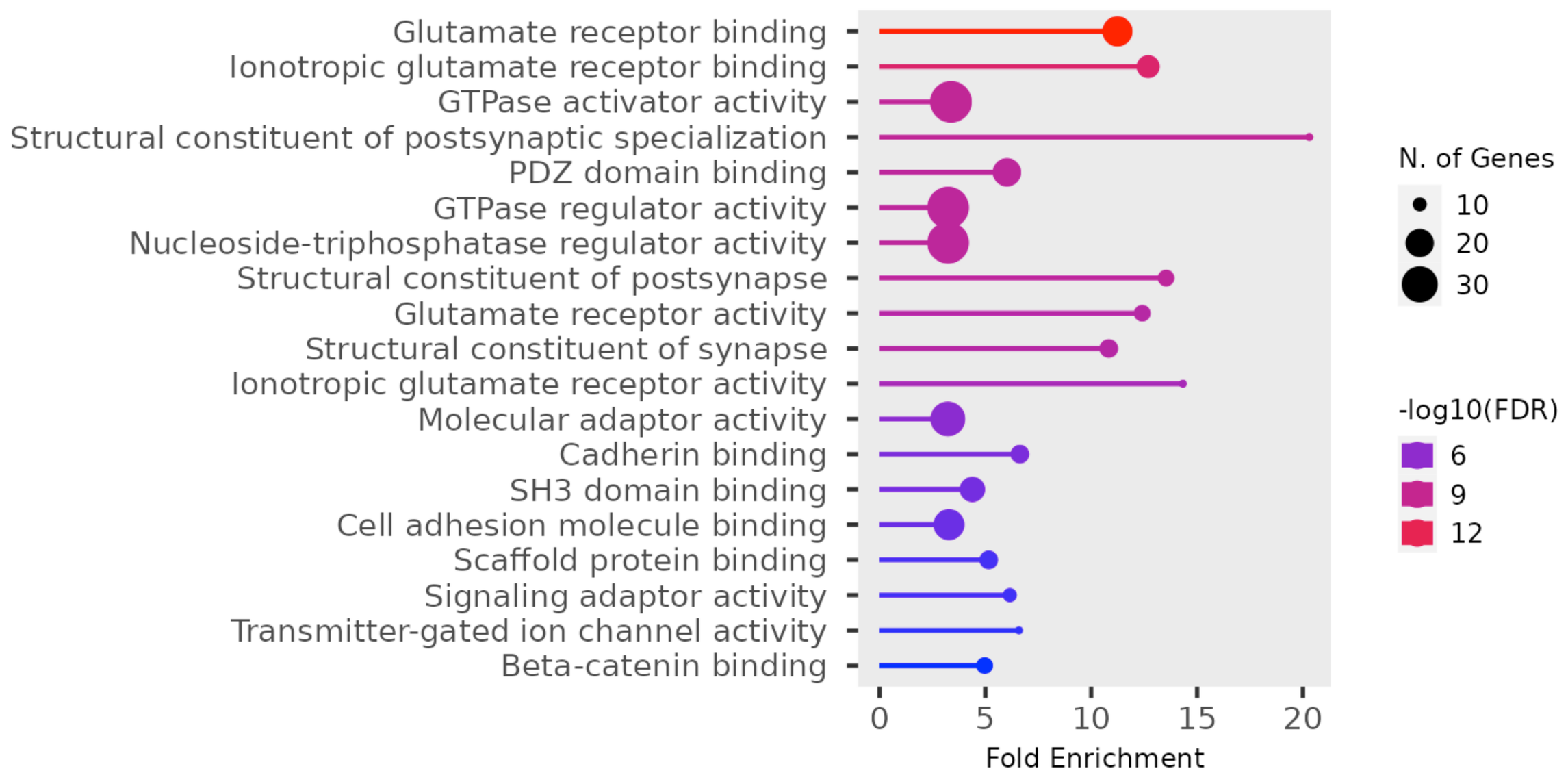

Supplementary Fig. S13

Shank2 interactome

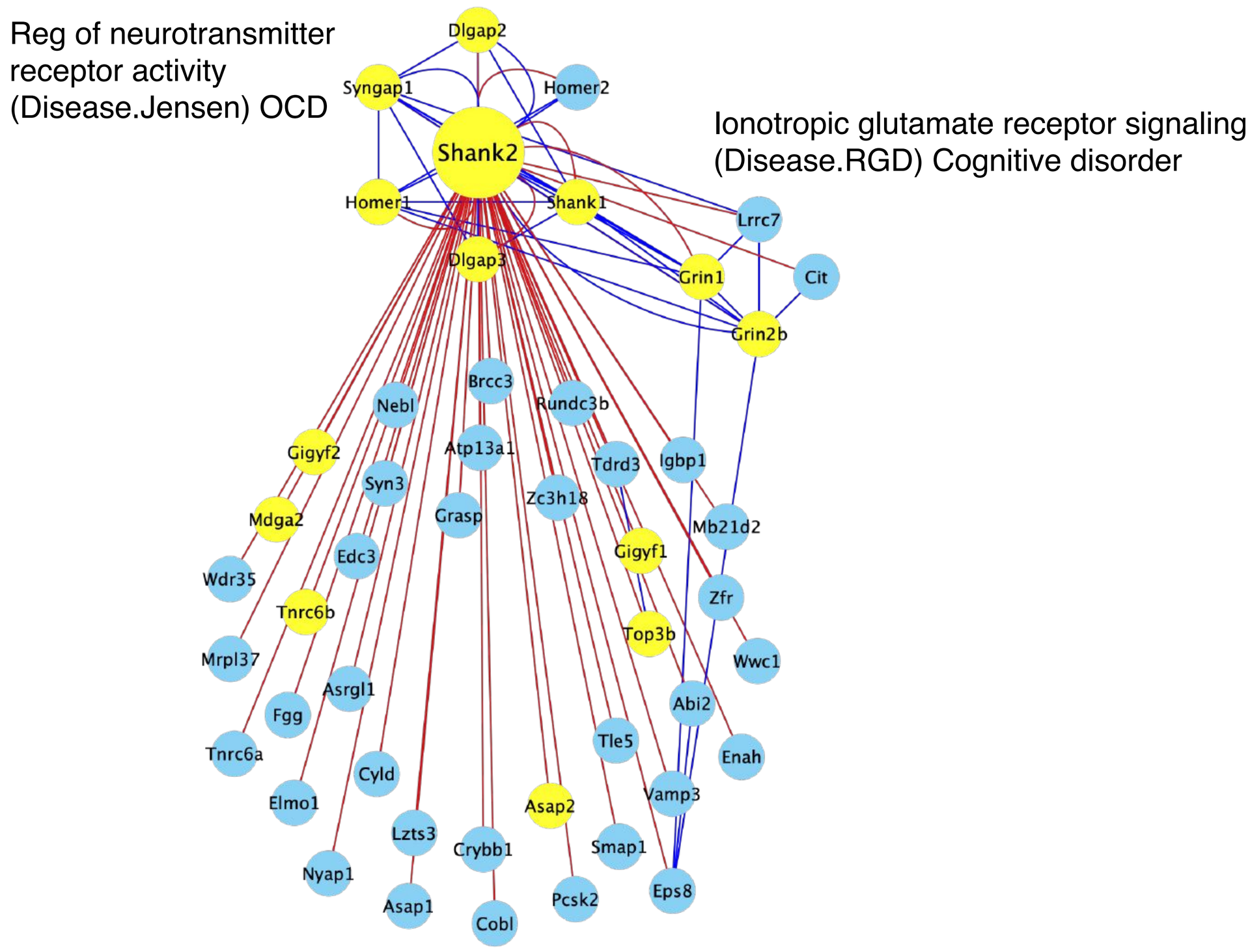

GO : Molecular Function

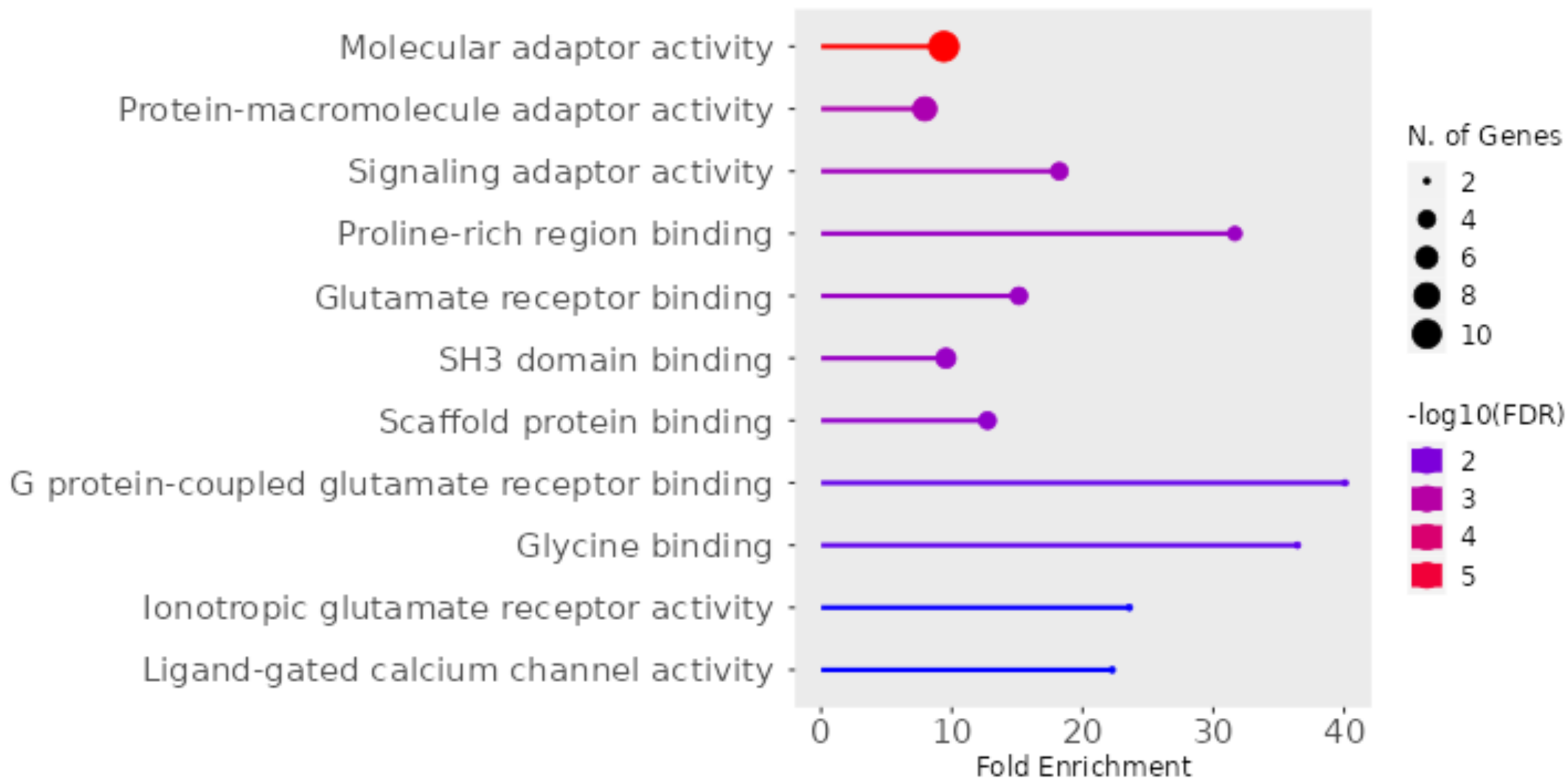

Supplementary Fig. S14

Shank3 interactome

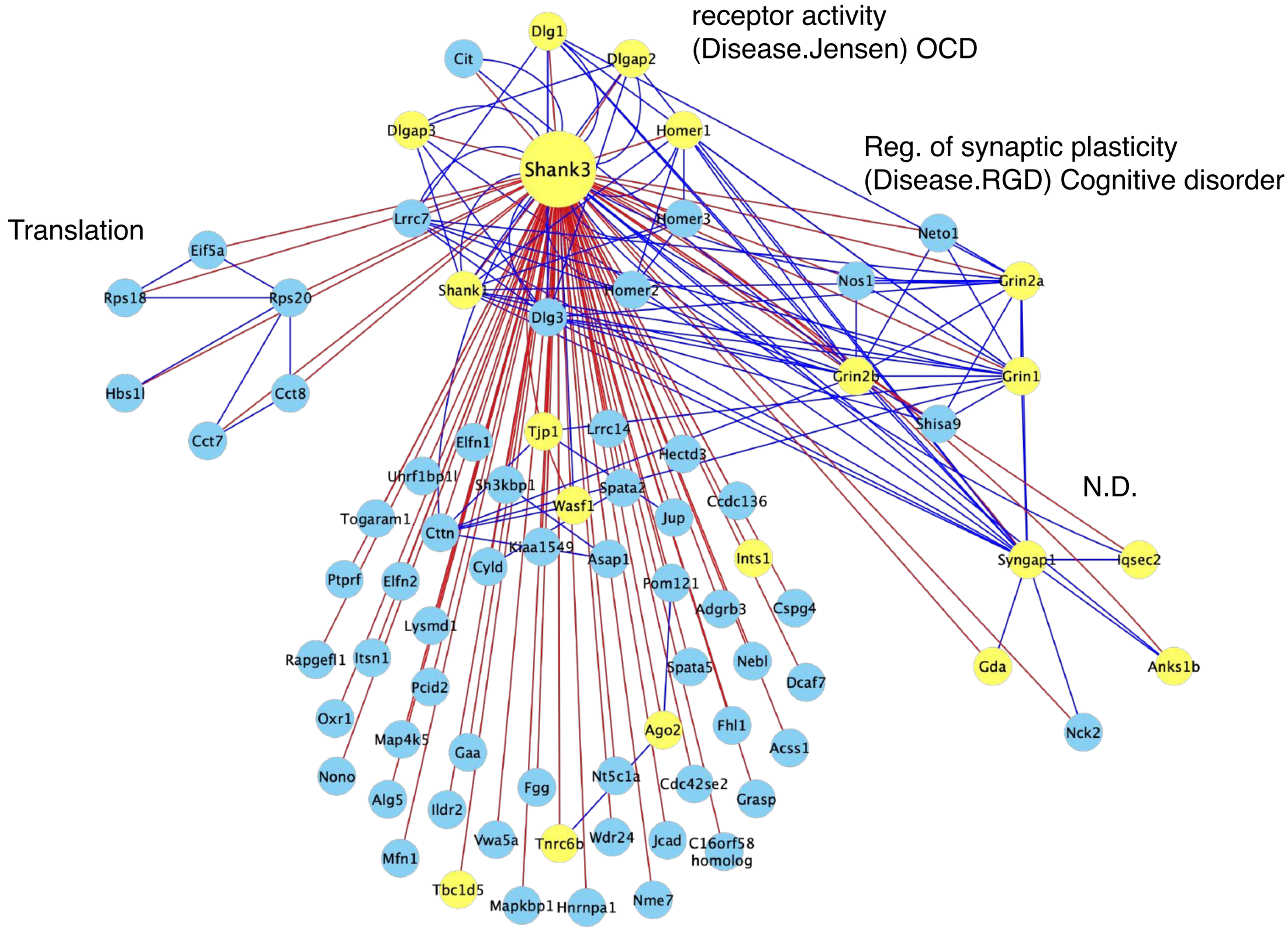

GO : Molecular Function

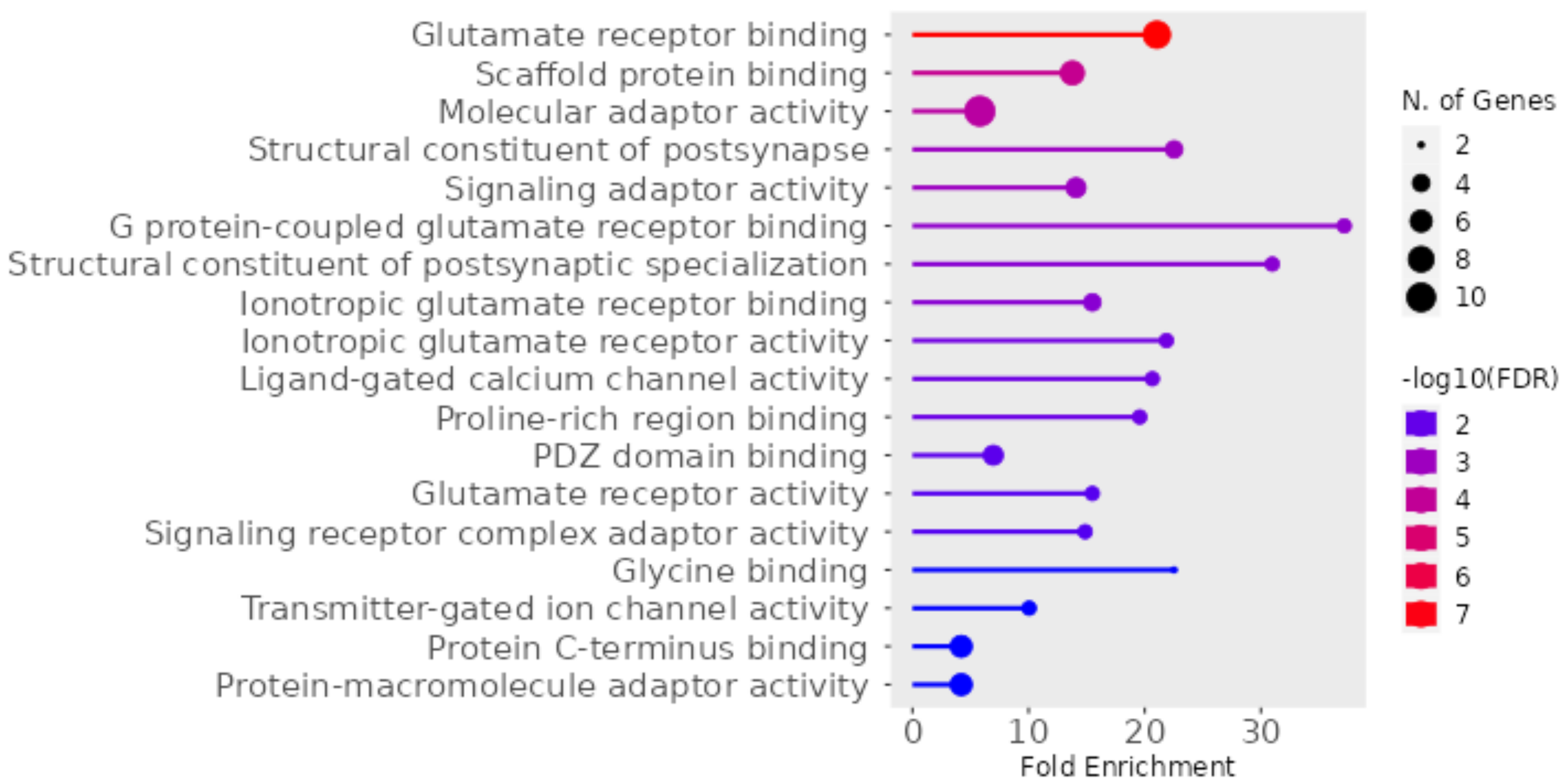

Nckap1 interactome

Supplementary Fig. S15

Glutamate receptor signaling (Disease.RGD) ID, schizophrenia

Pos. reg. of Arp2/3 actin nucleation

Gi-coupled glutamate receptor signaling

N.D.

Synaptic membrane adhesion

Glutamate receptor signaling (Disease.RGD) ID

GO : Molecular Function

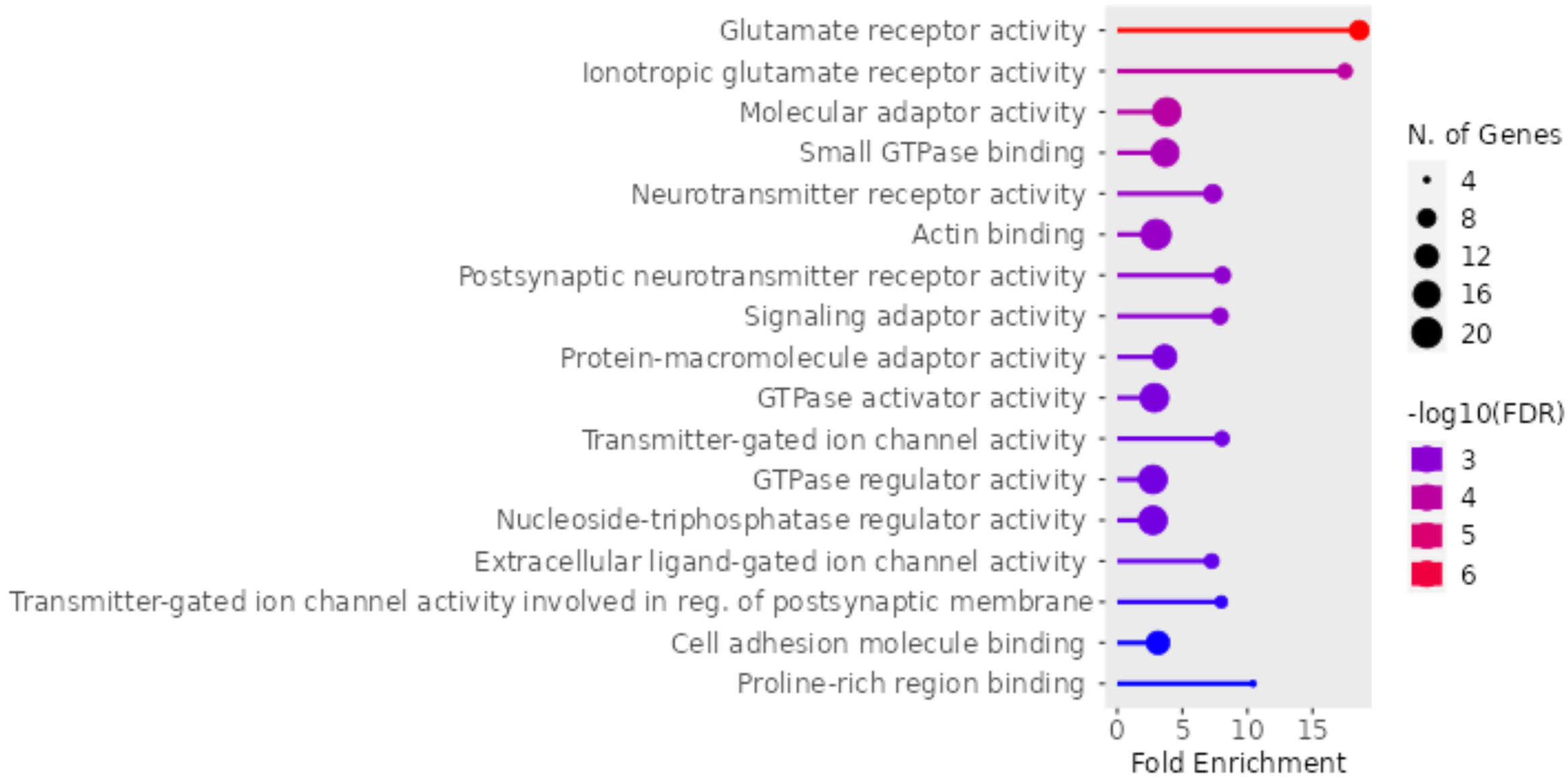

Nbea interactome

Supplementary Fig. S16

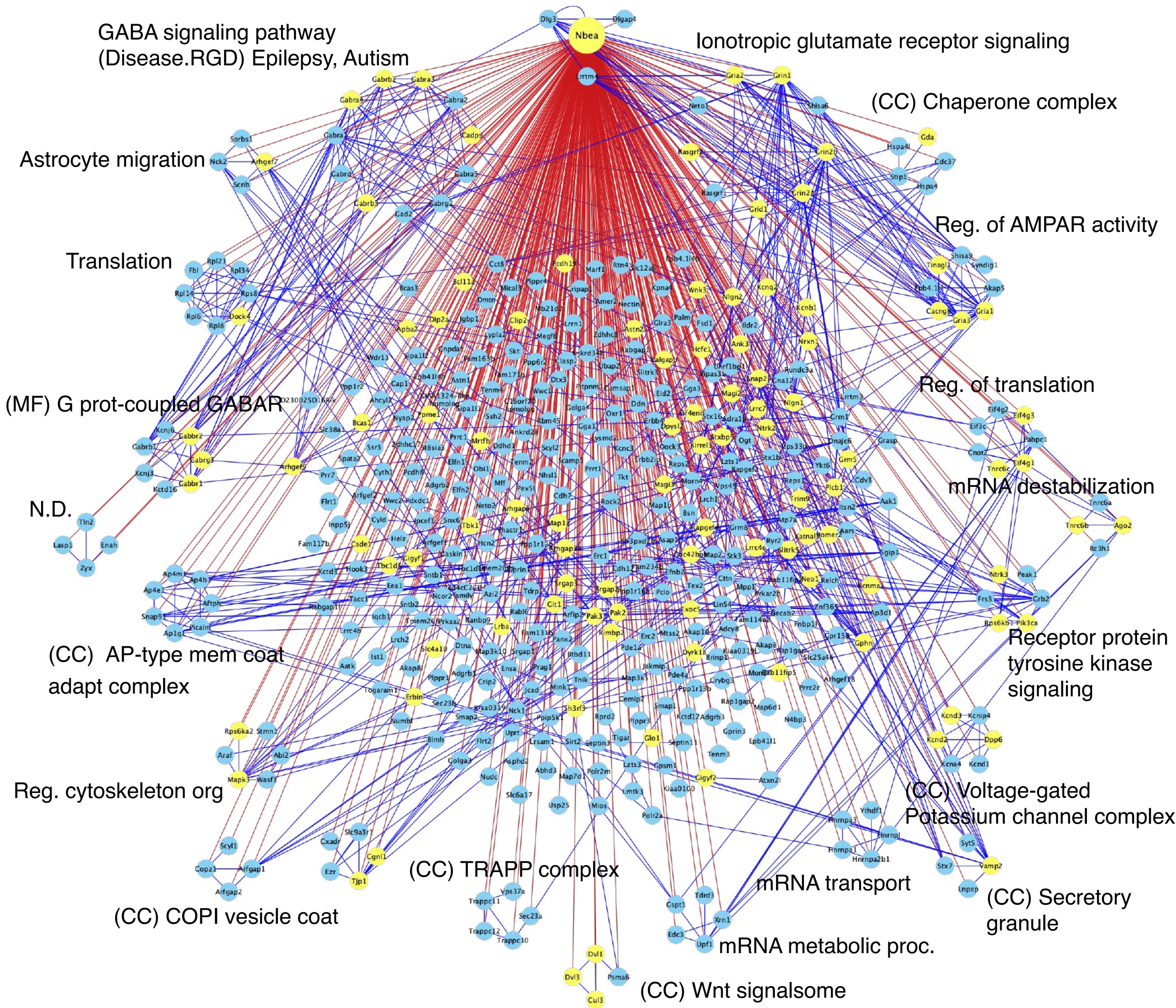

GO : Molecular Function

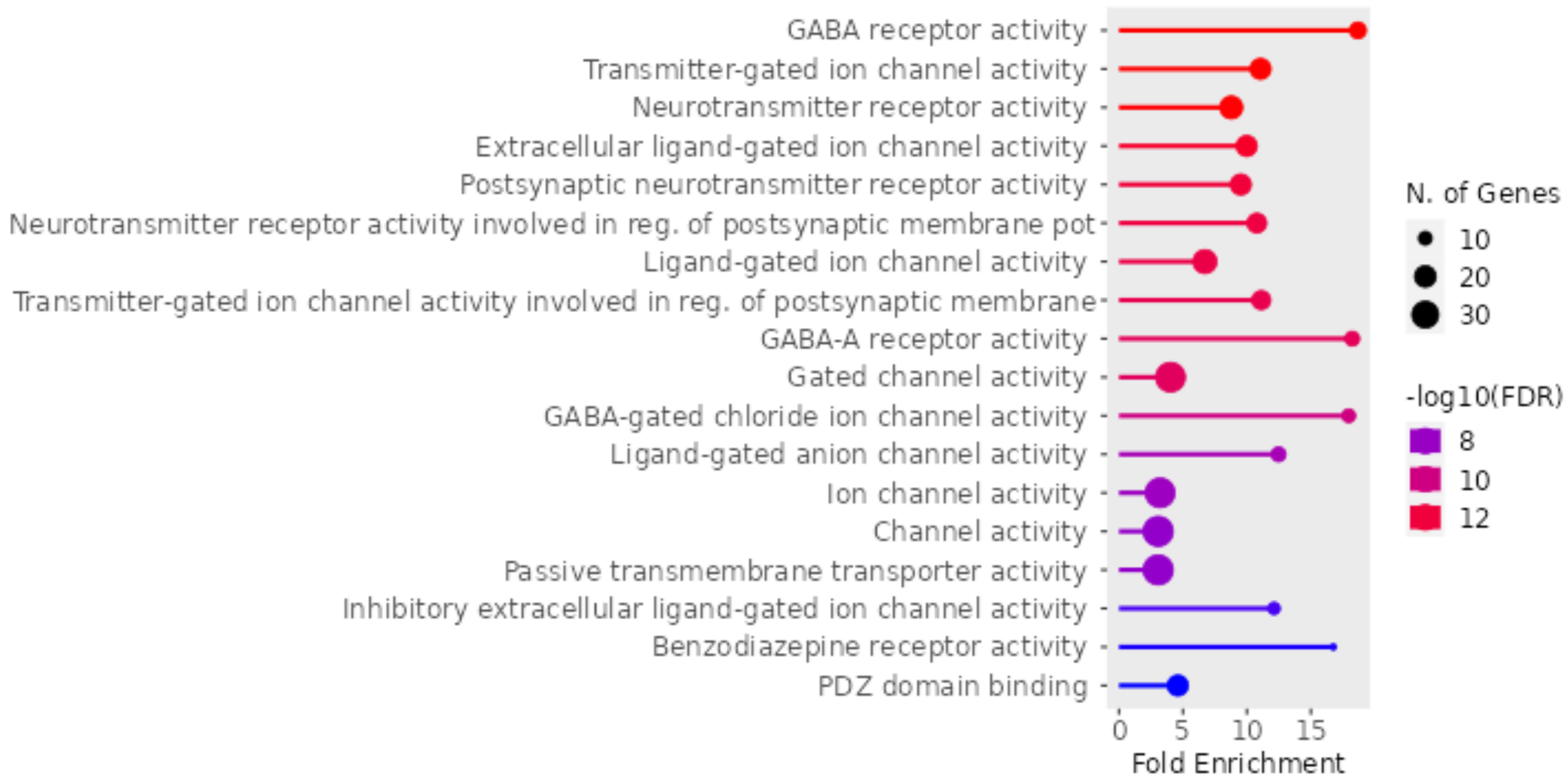

Supplementary Fig. S17

Ctnnb1 interactome

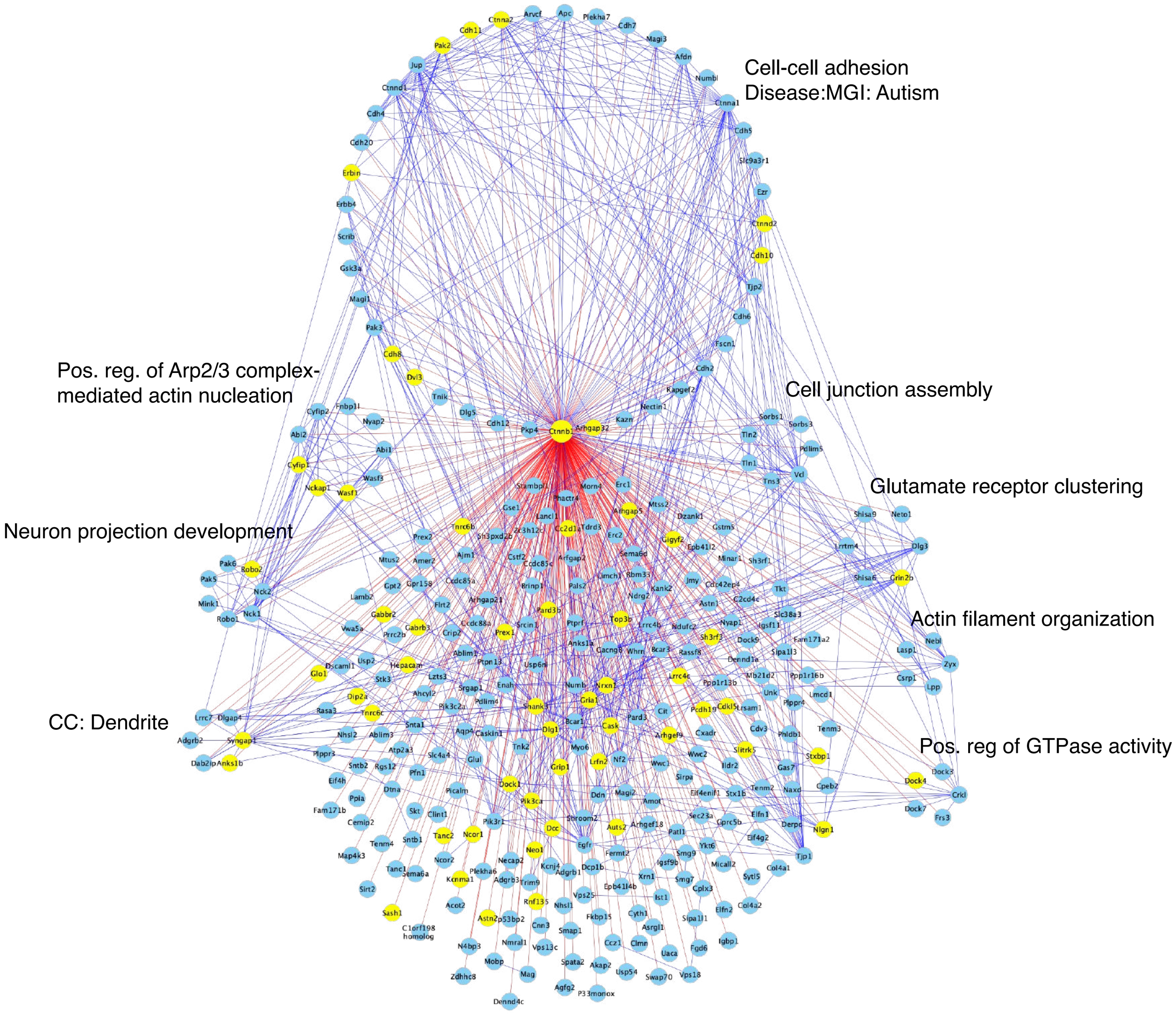

GO : Molecular Function

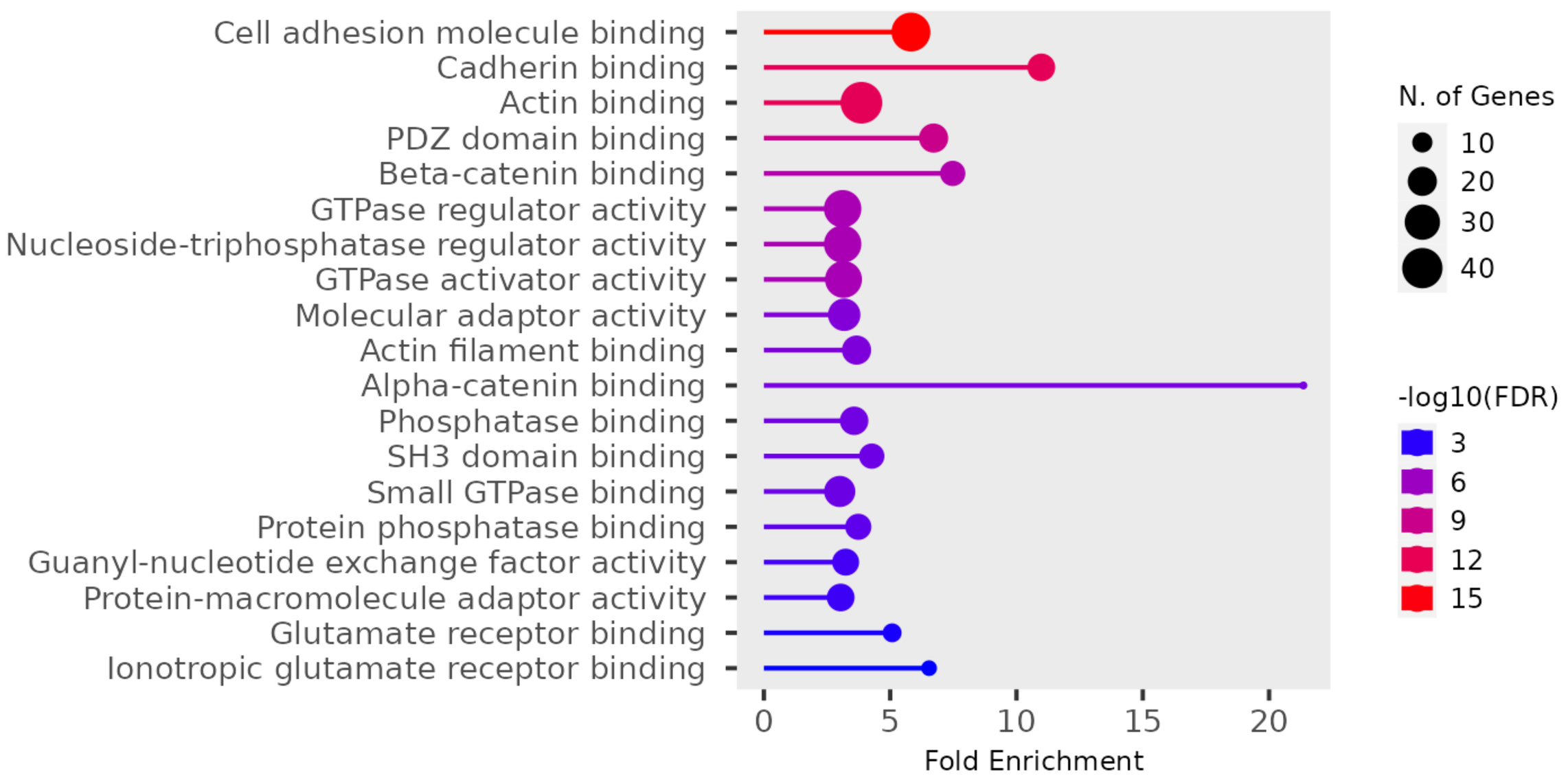

Supplementary Fig. S18

Lrrc4c interactome

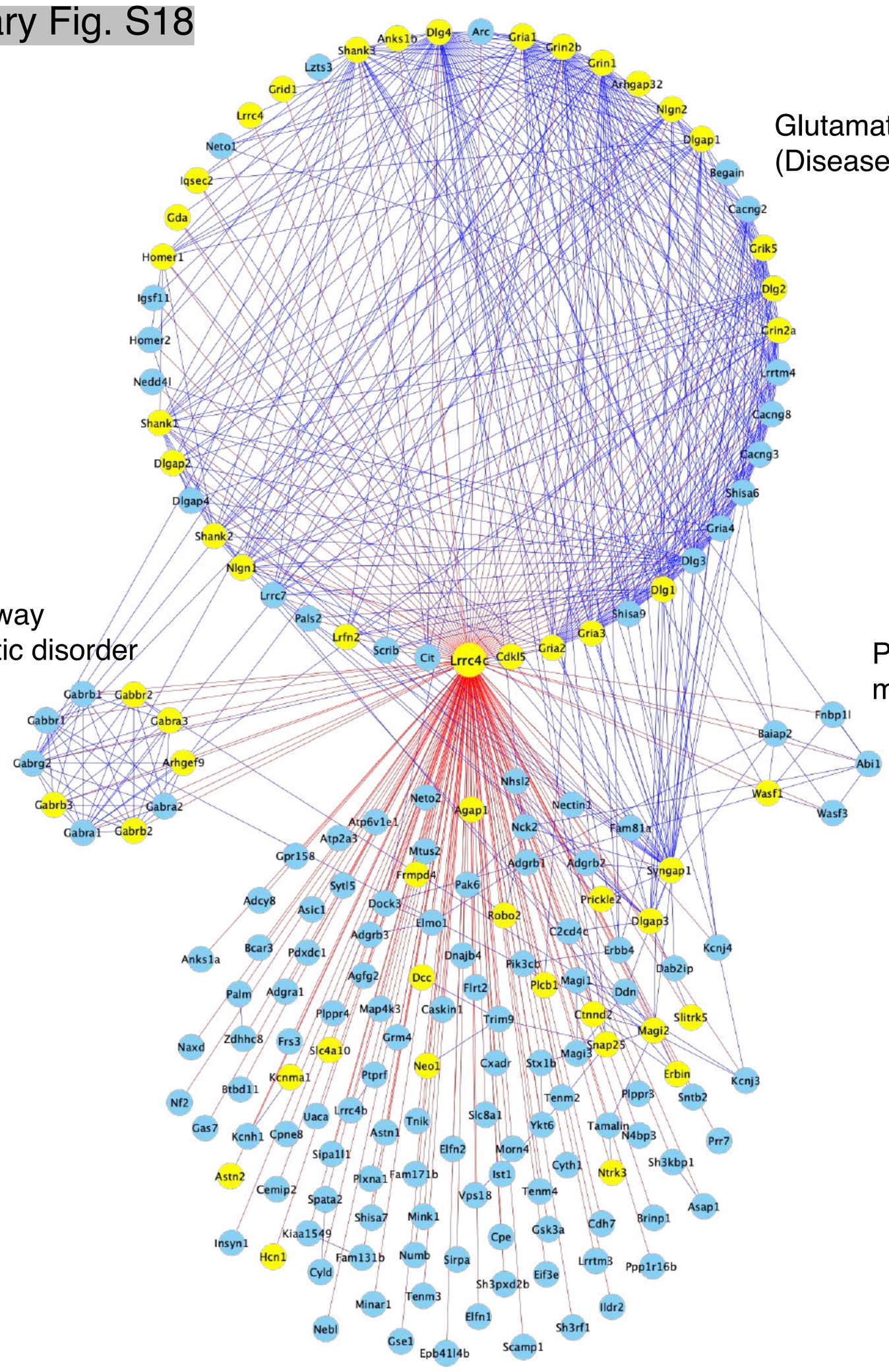

GO : Molecular Function

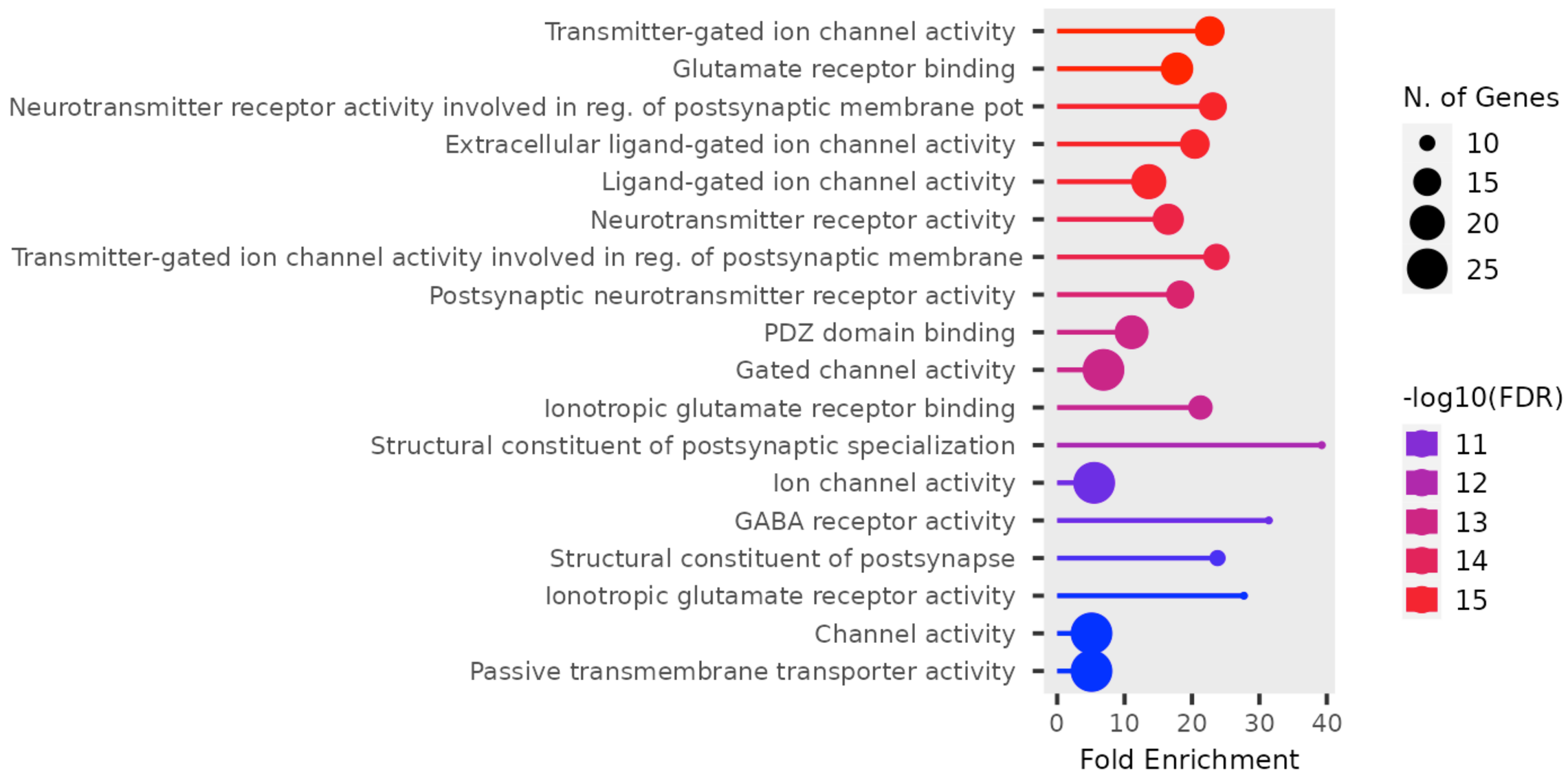

Supplementary Fig. S19

Iqsec2 interactome

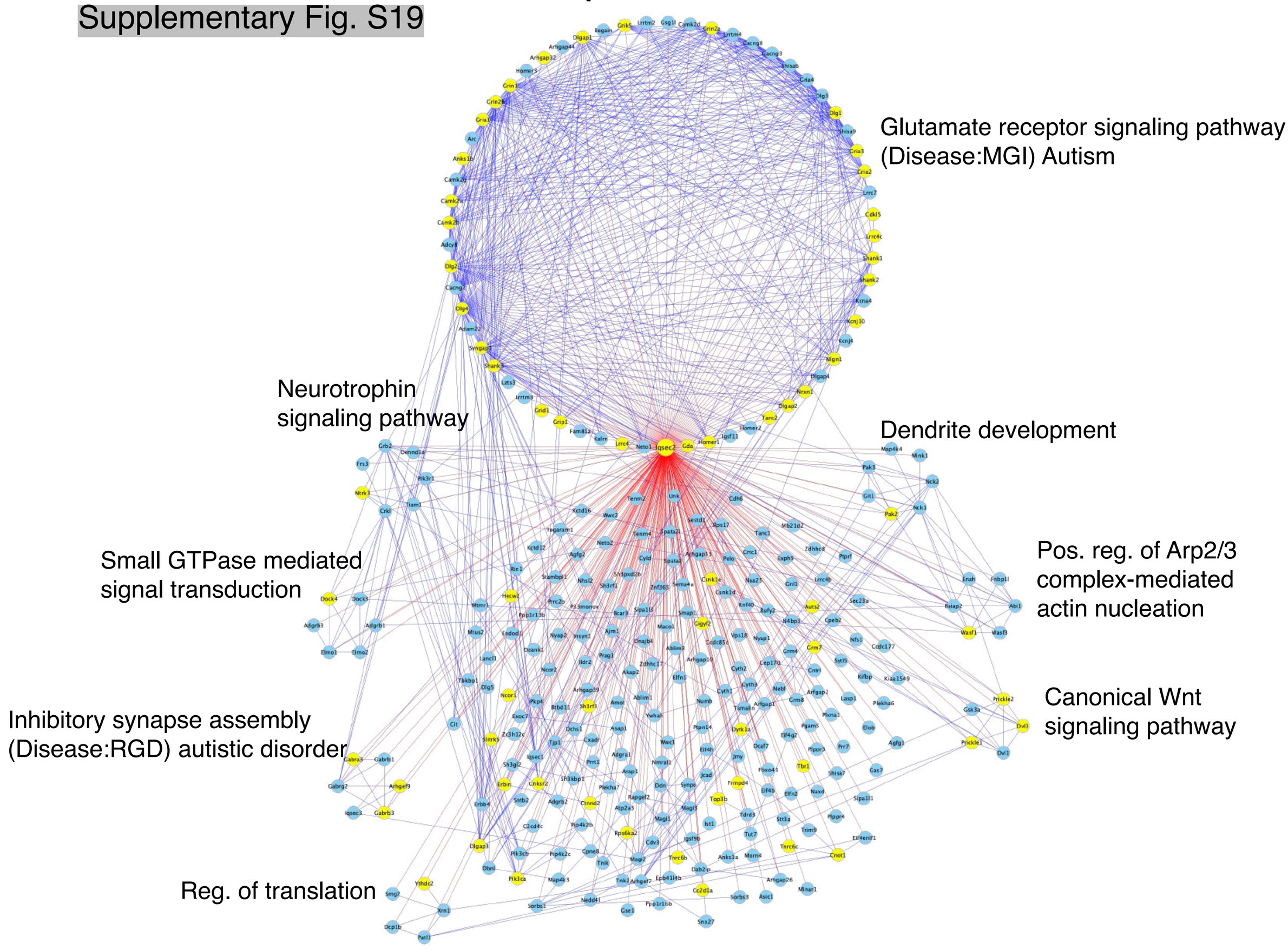

GO : Molecular Function

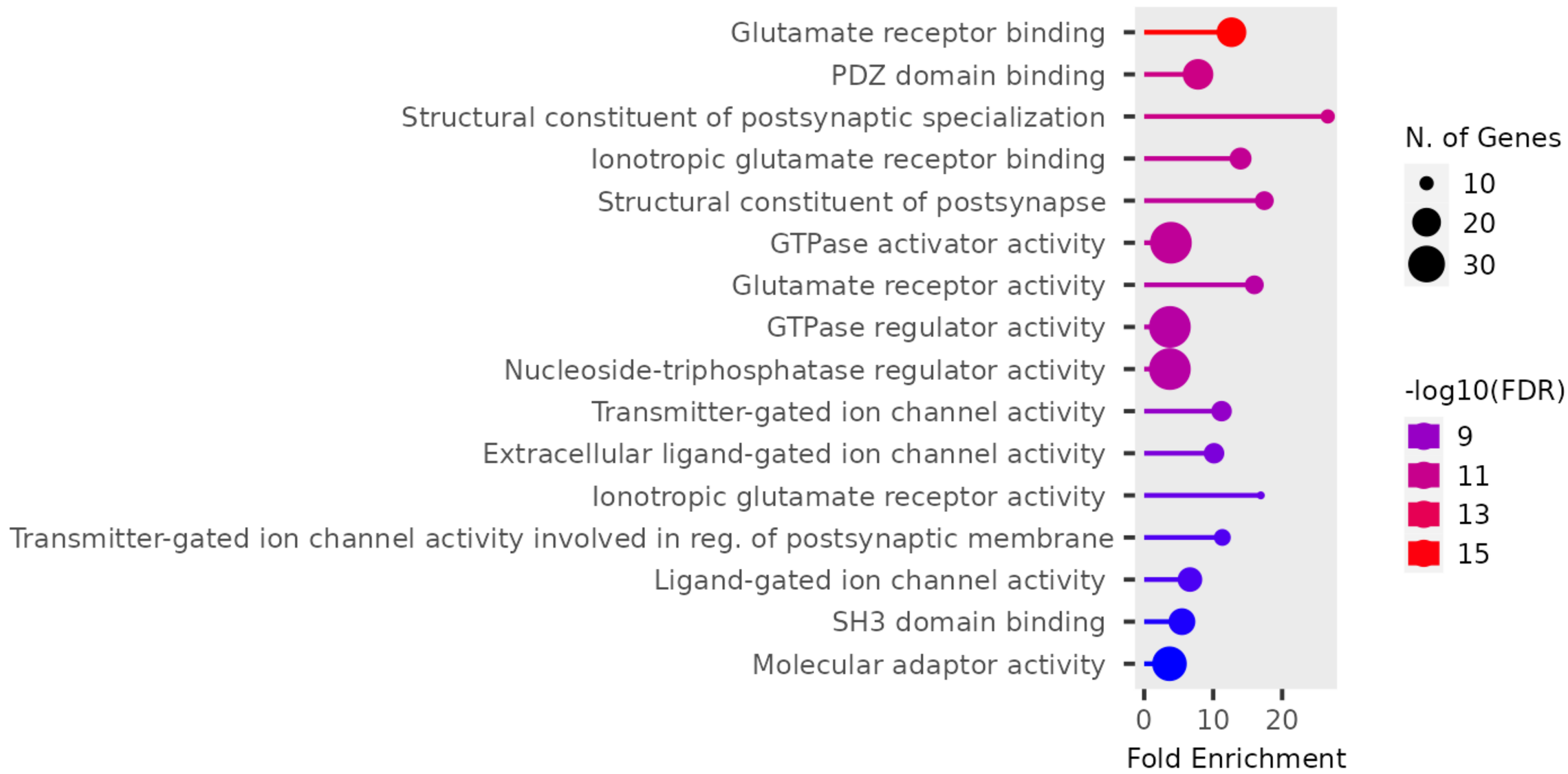

Supplementary Fig. S20

Arhgef9 interactome

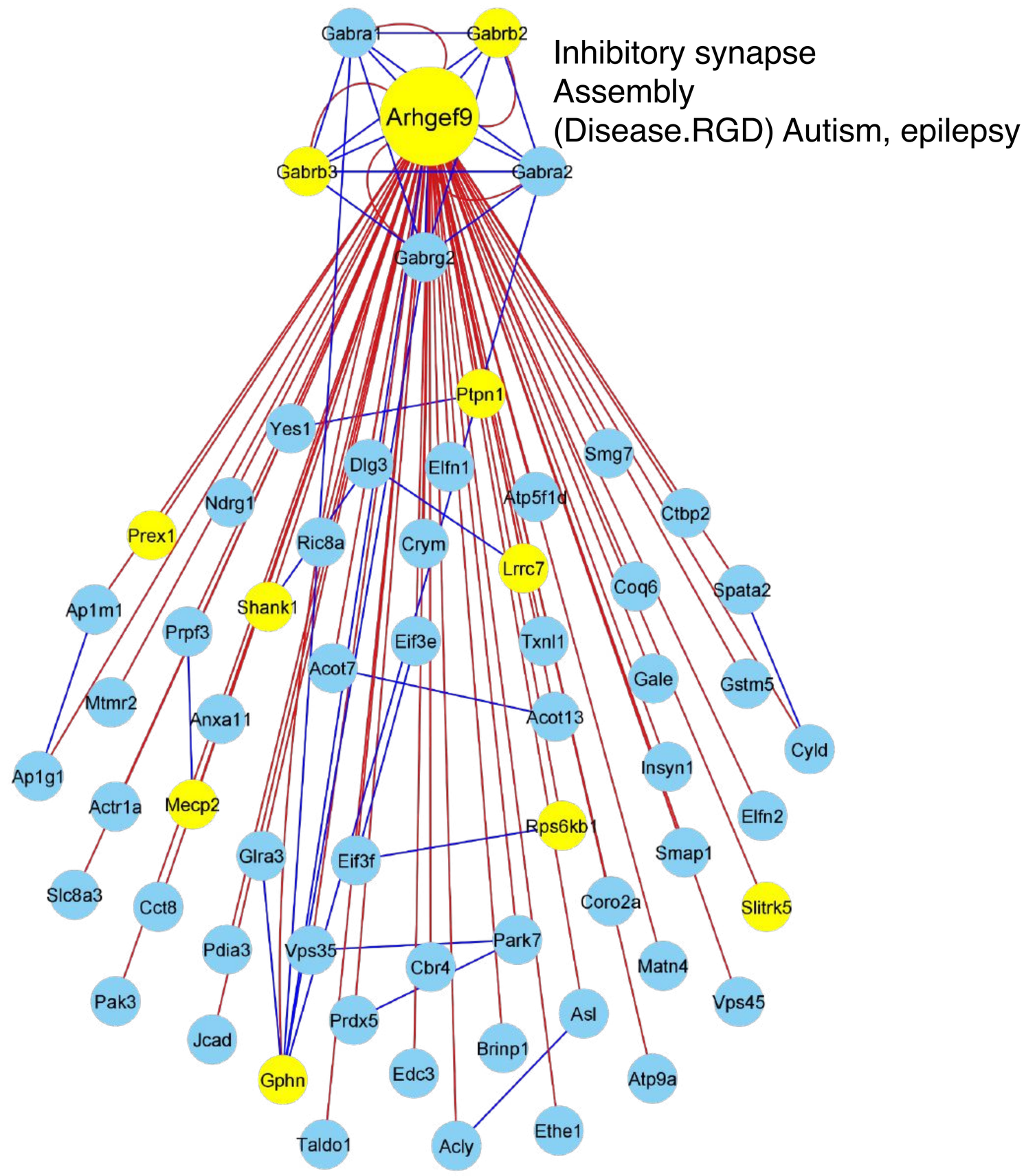

GO : Molecular Function

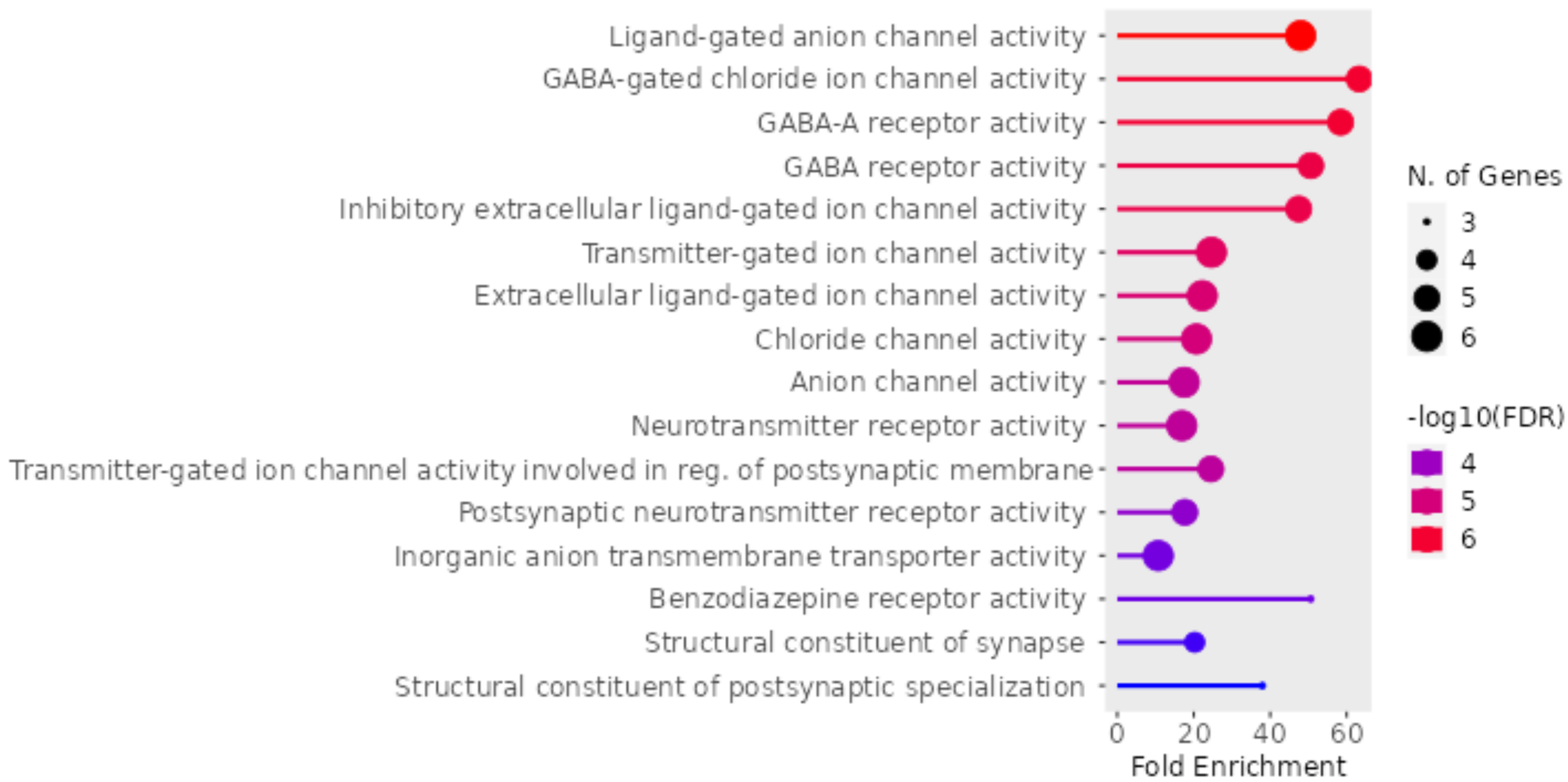

Ank3 interactome

Supplementary Fig. S21

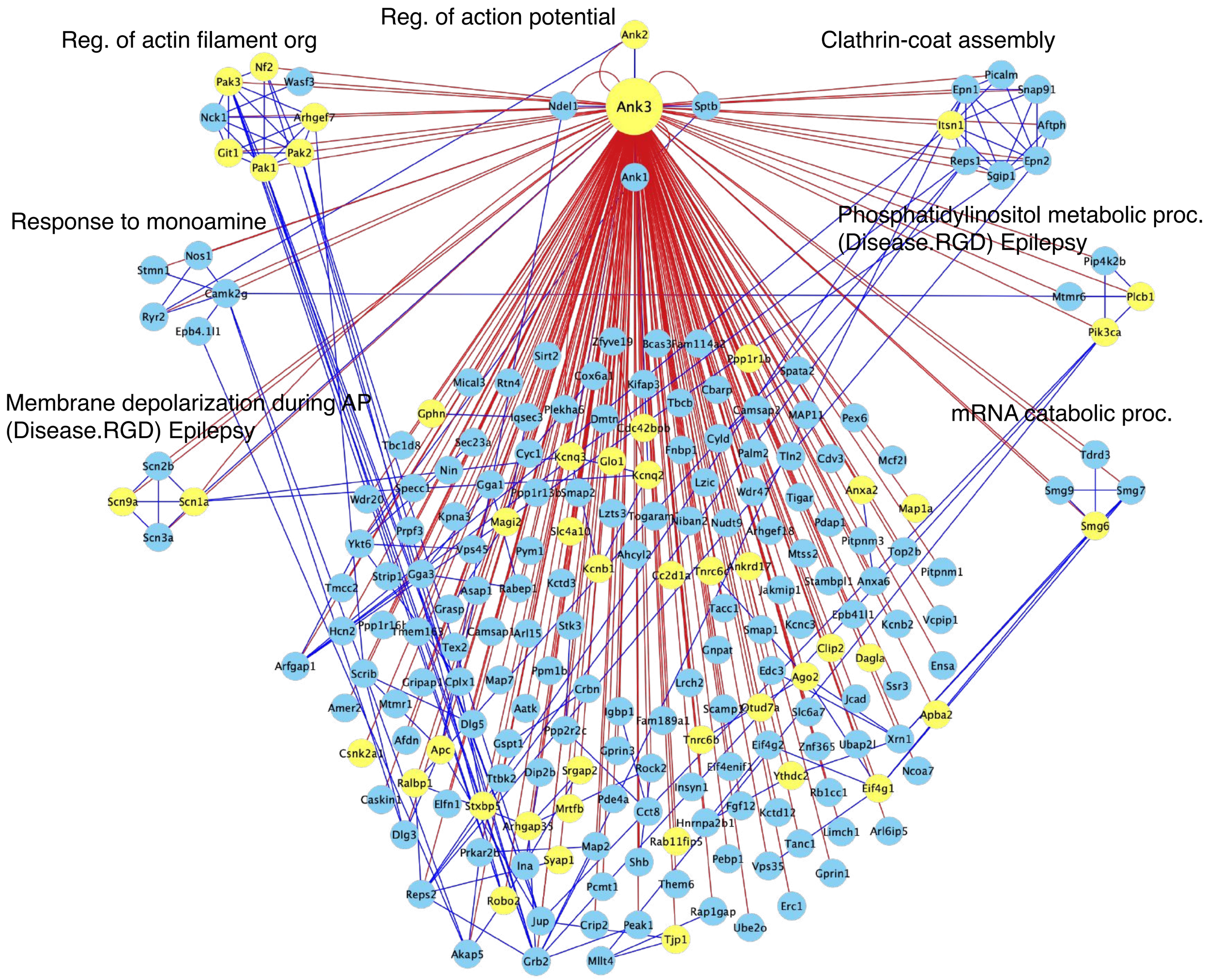

GO : Molecular Function

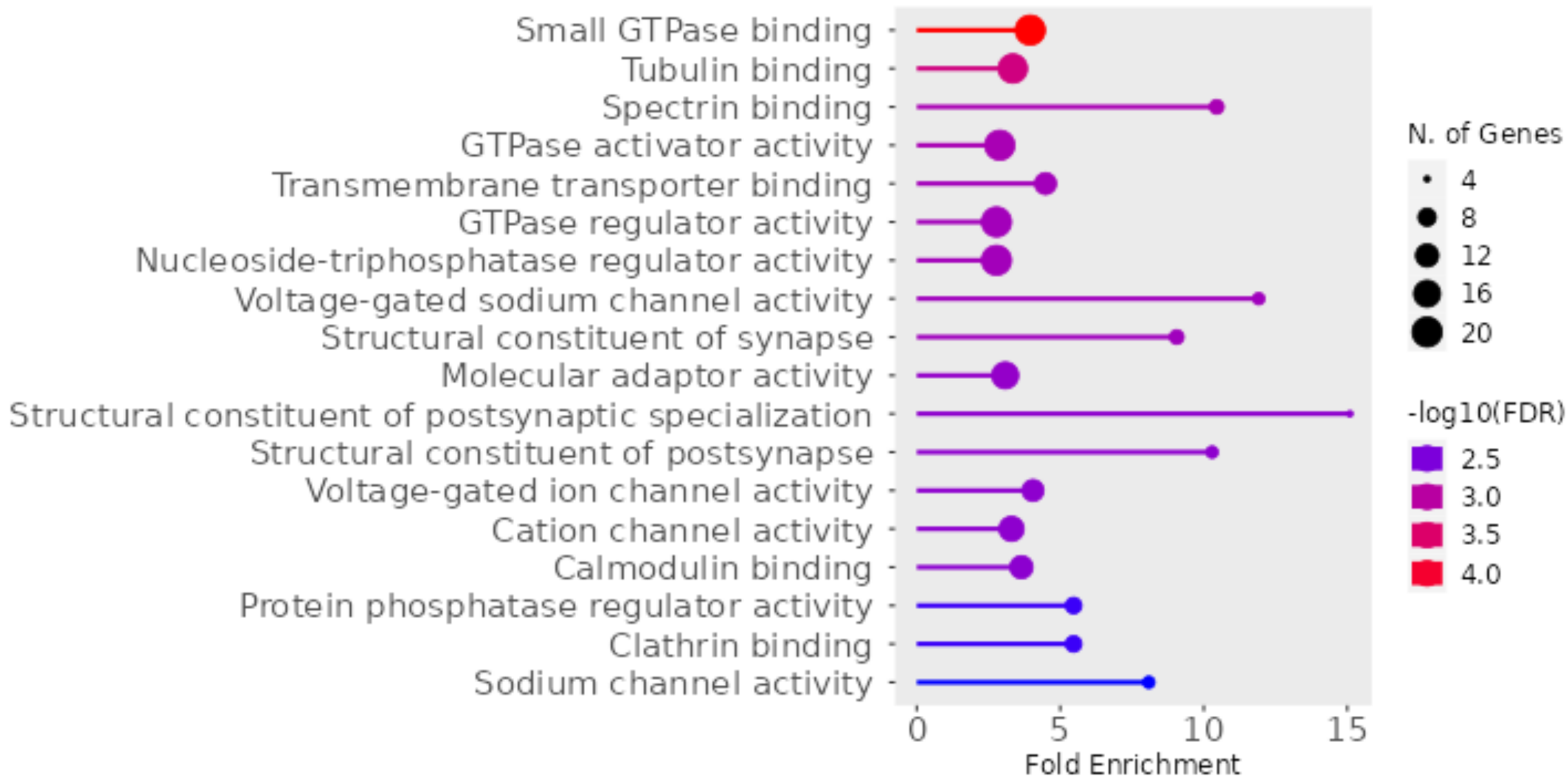

Scn2a interactome

Supplementary Fig. S22

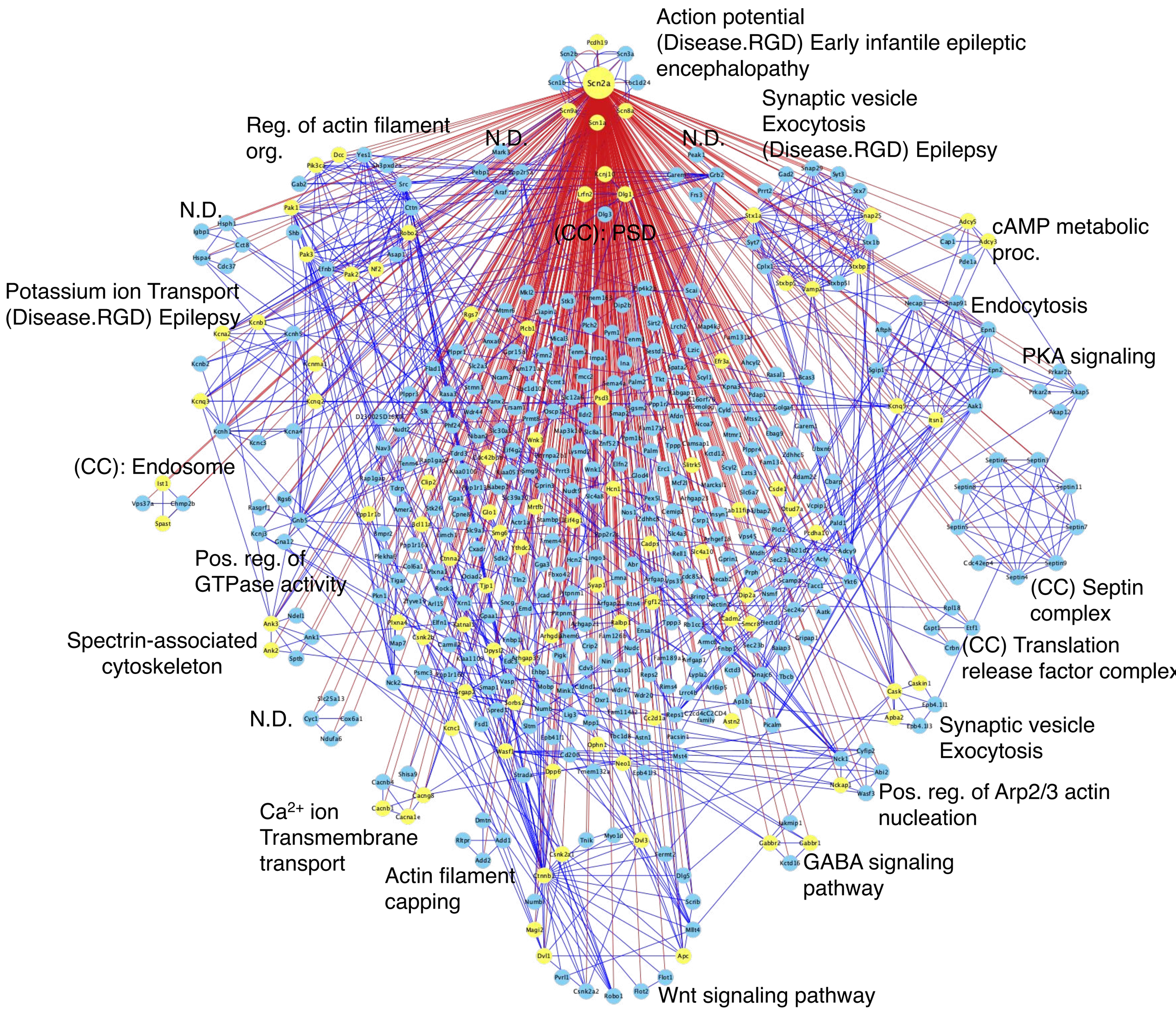

GO : Molecular Function

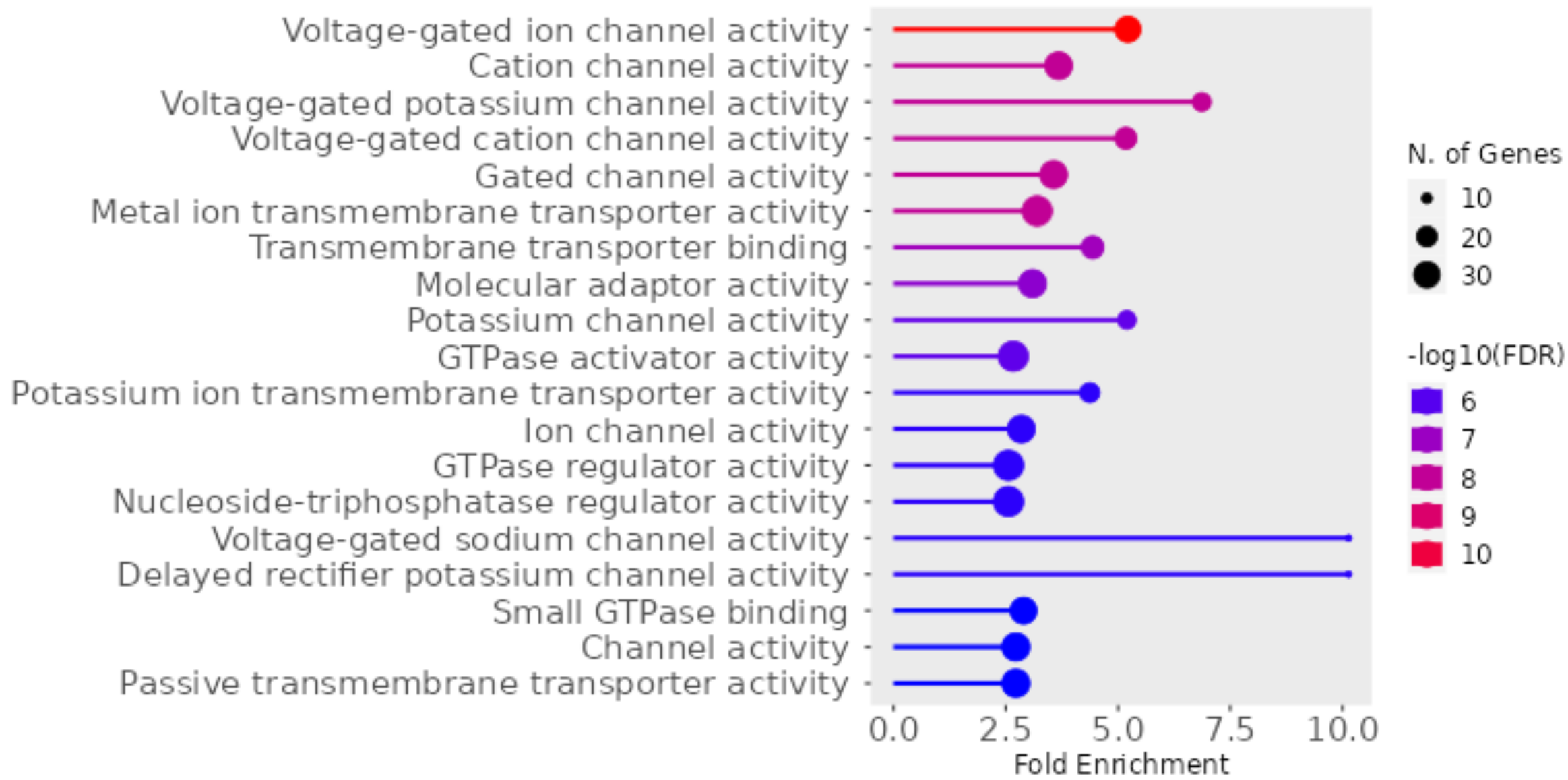

Scn8a interactome

Supplementary Fig. S23

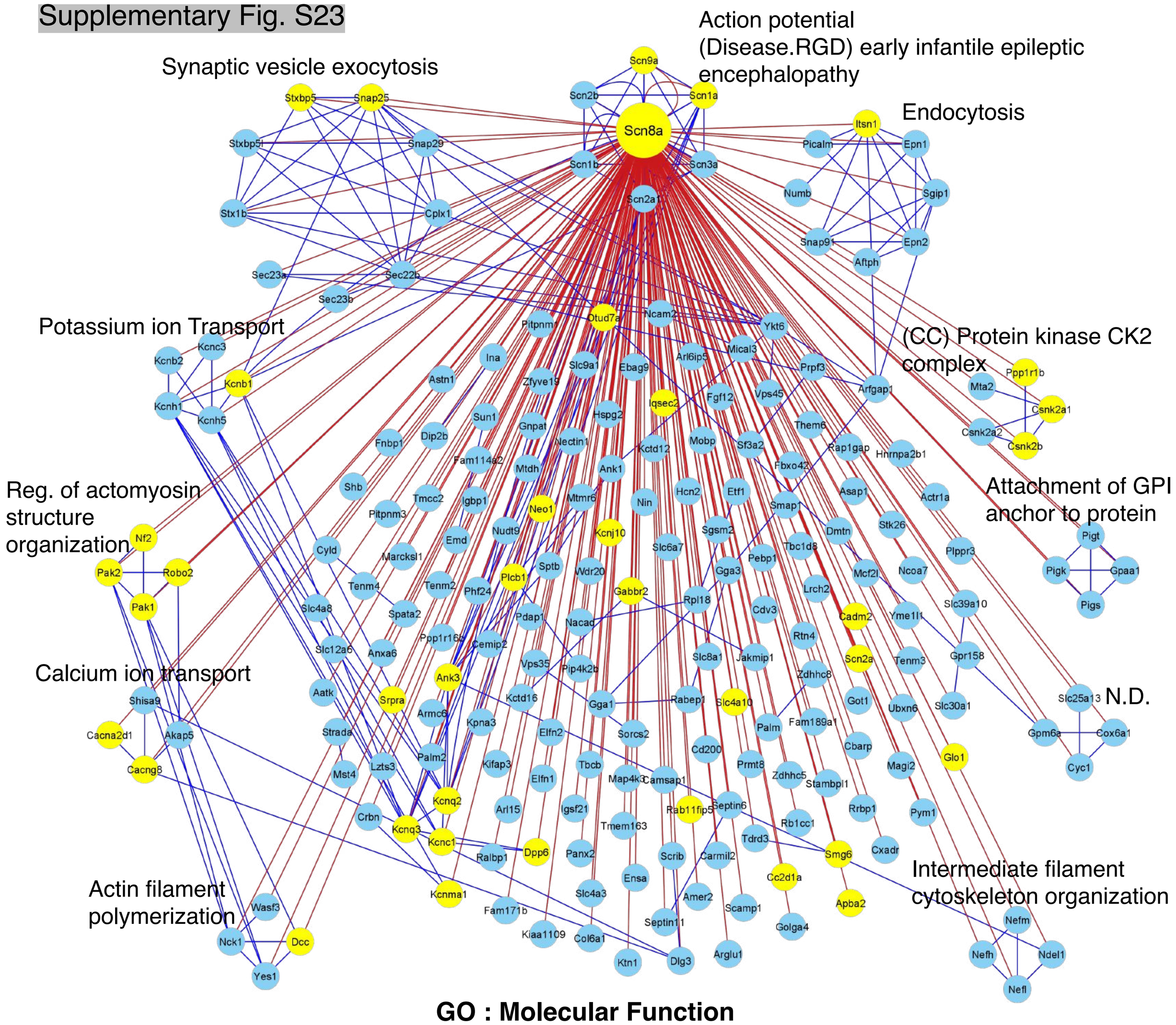

GO : Molecular Function

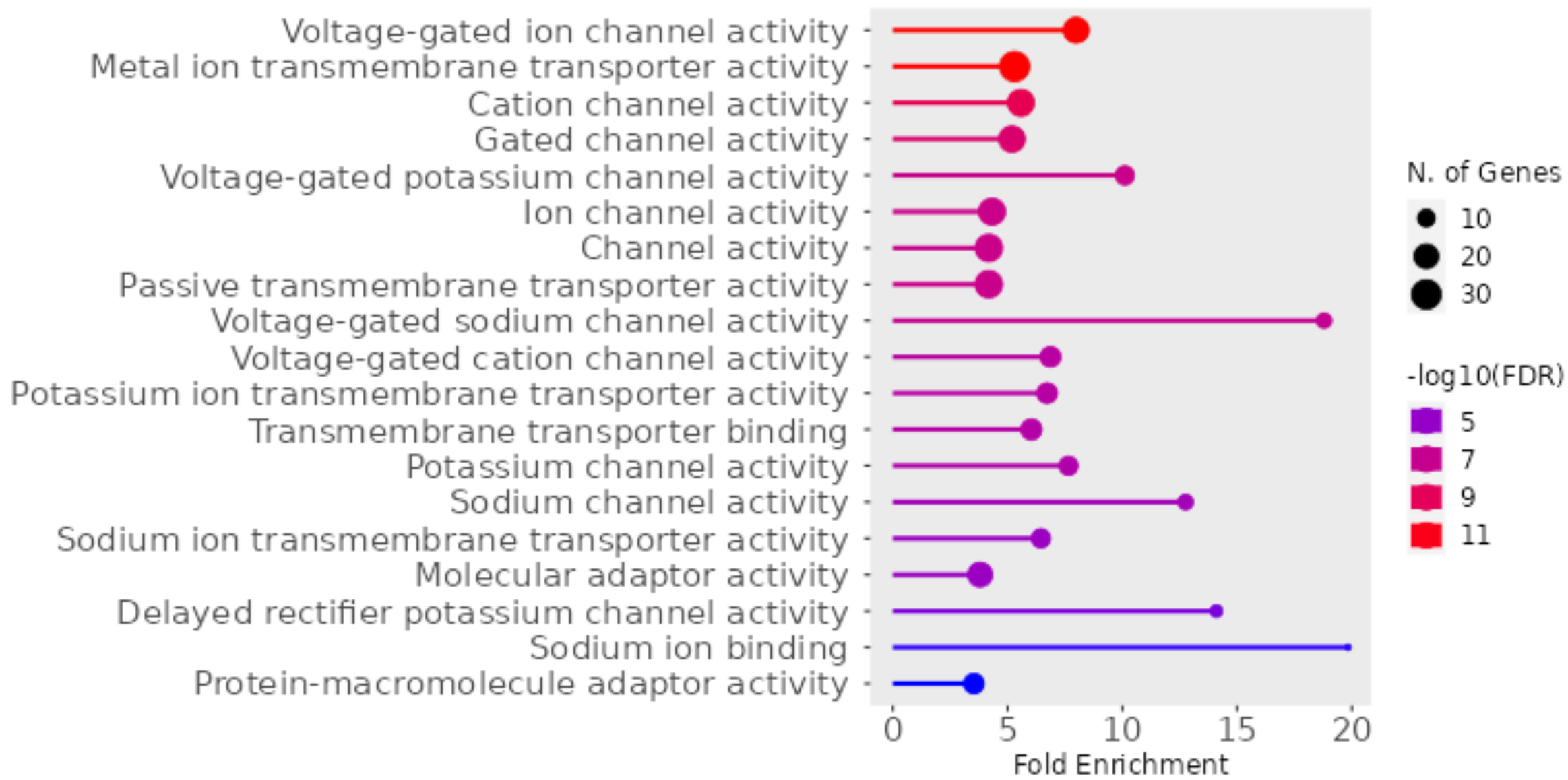

Supplementary Fig. S24

Hnrnpu interactome

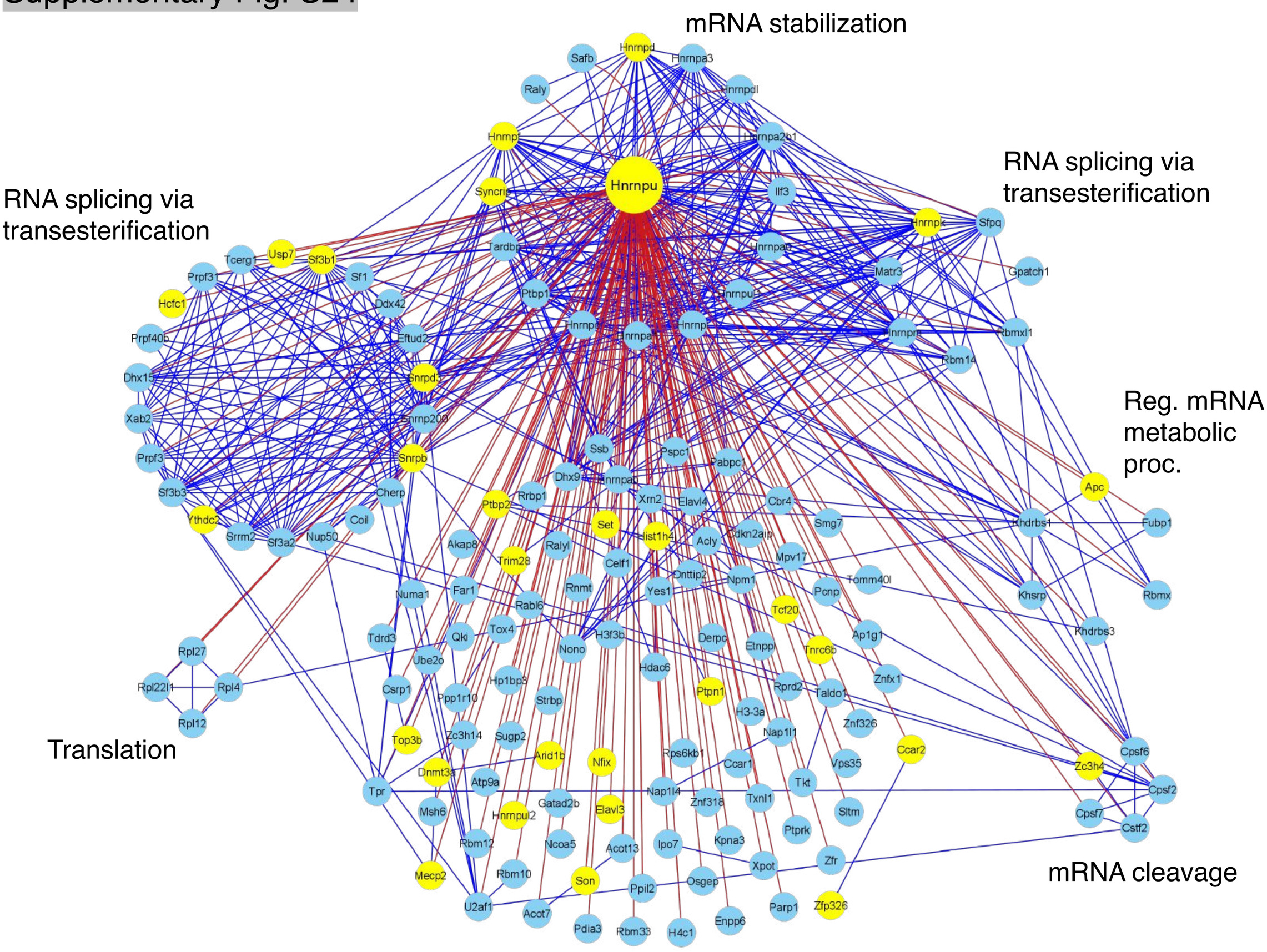

GO : Molecular Function

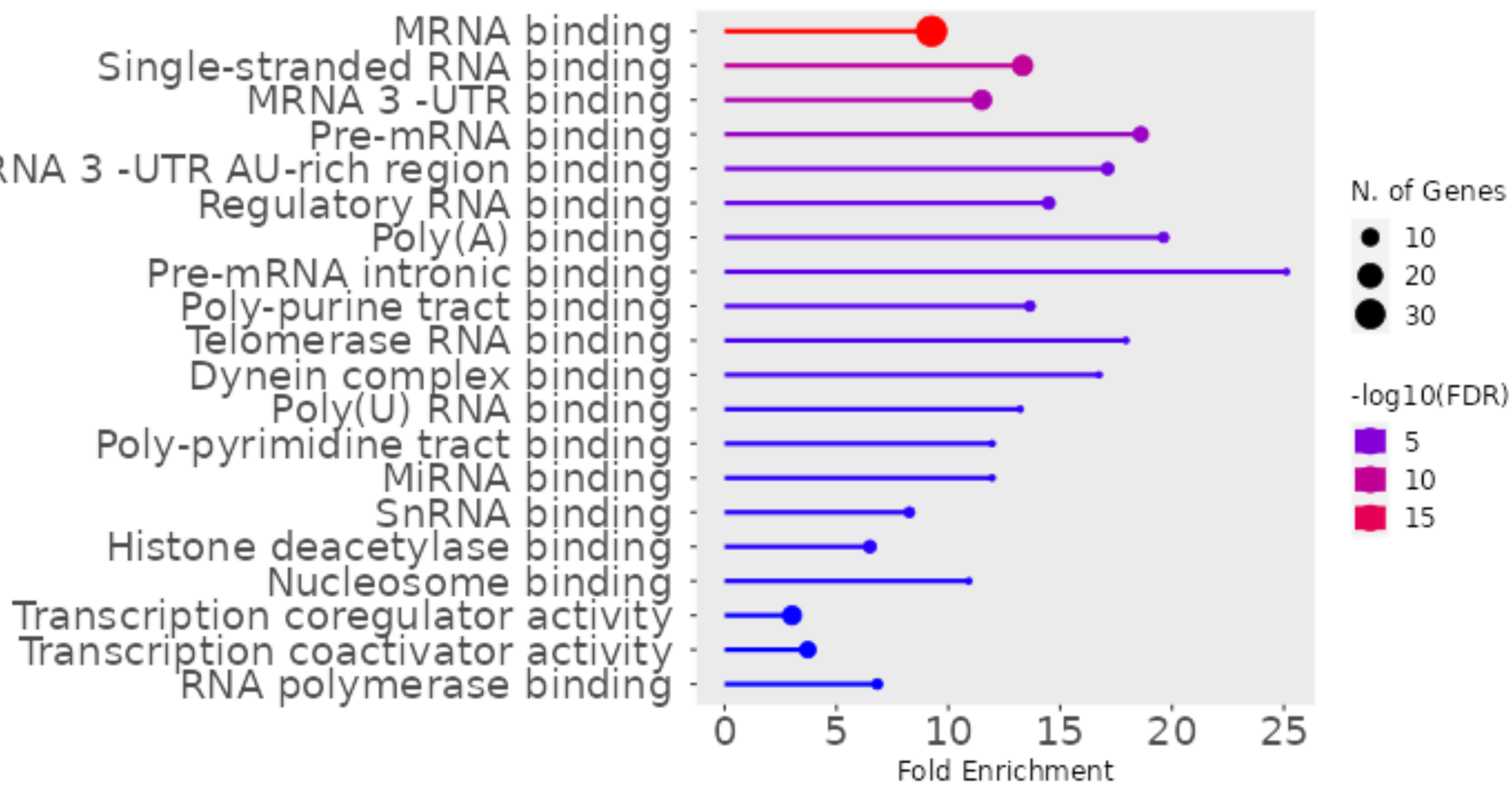

Supplementary Fig. S25

Homer1 interactome

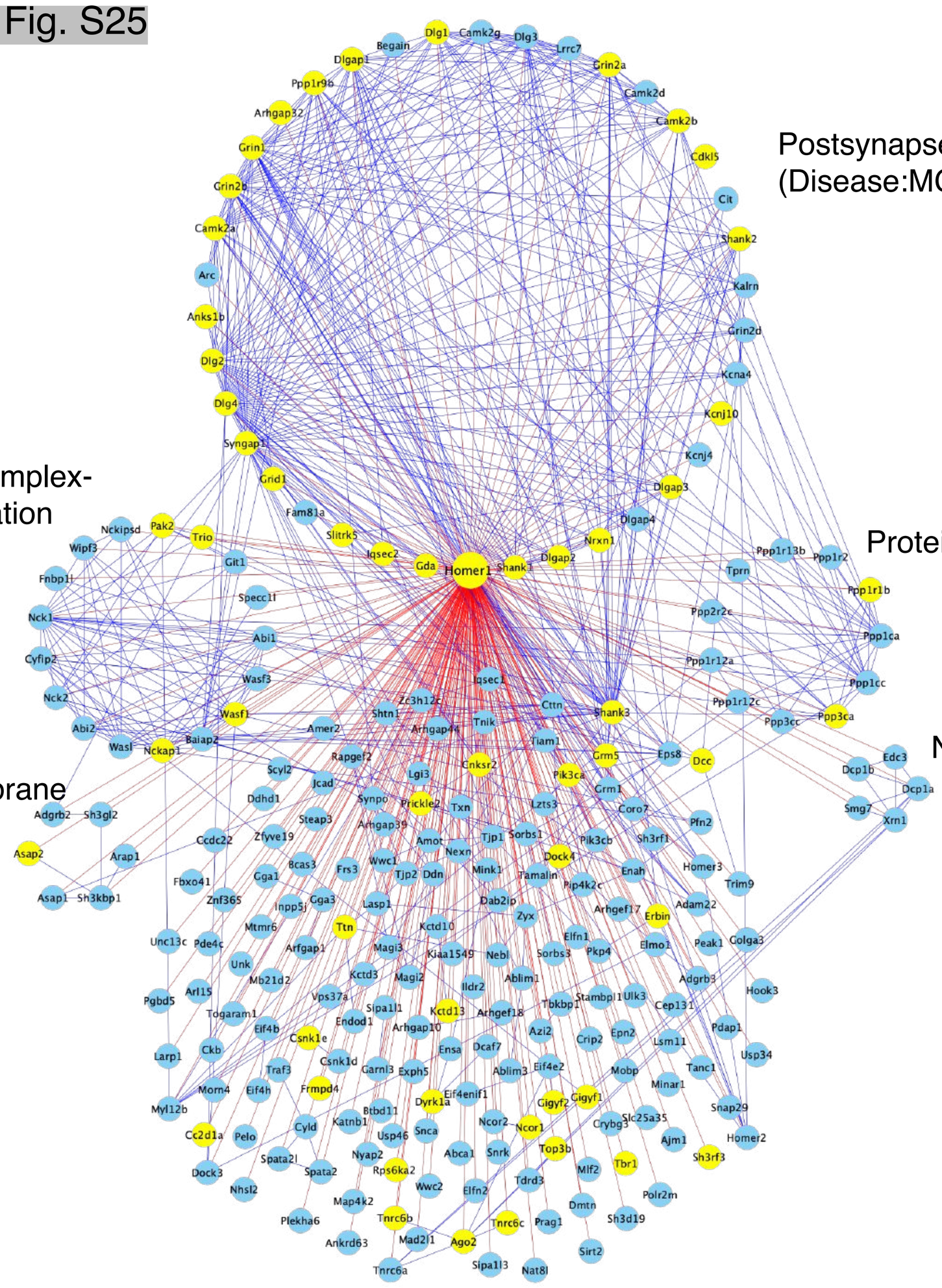

GO : Molecular Function

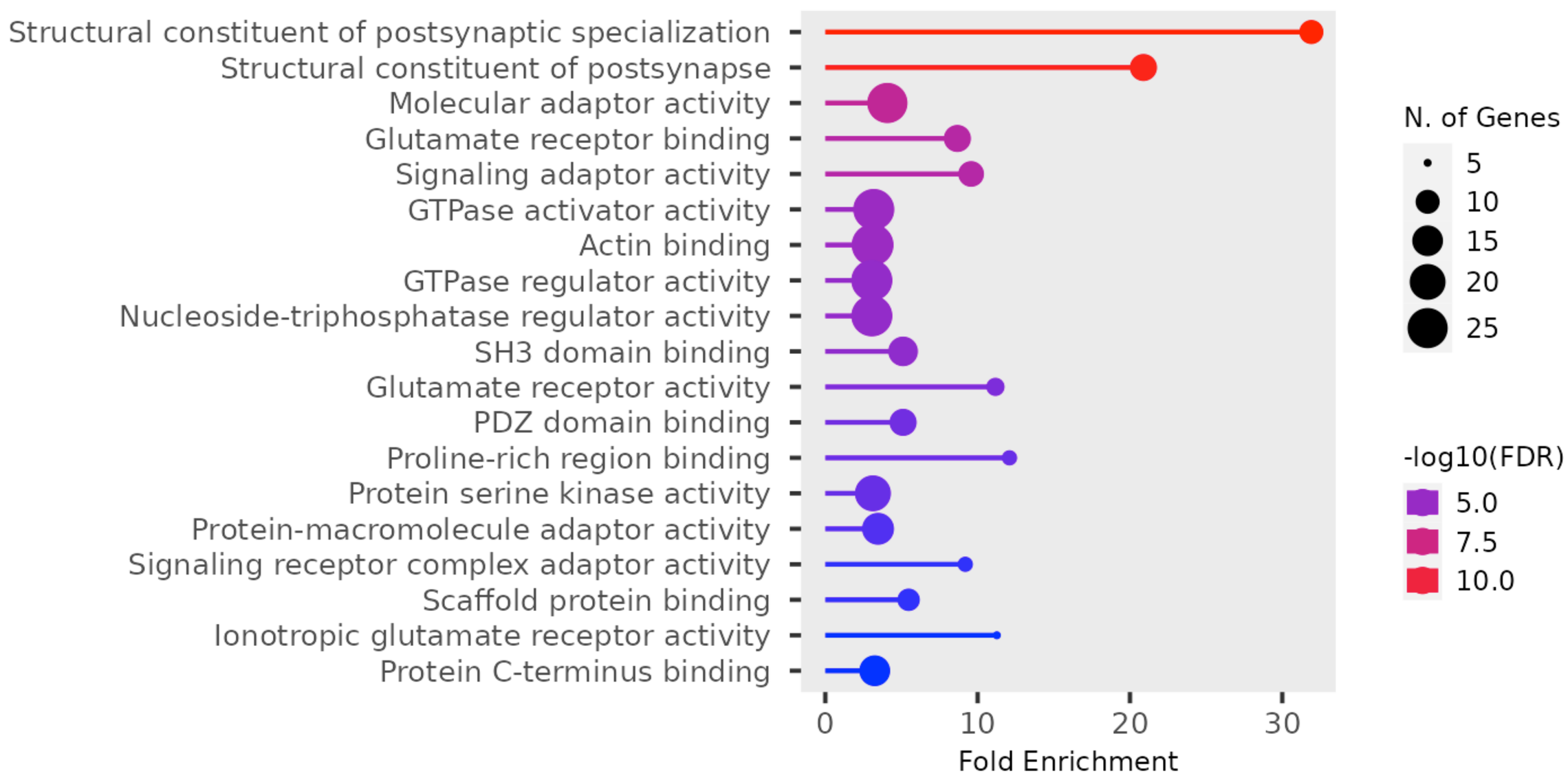

Supplementary Fig. S26

Wasf1 interactome

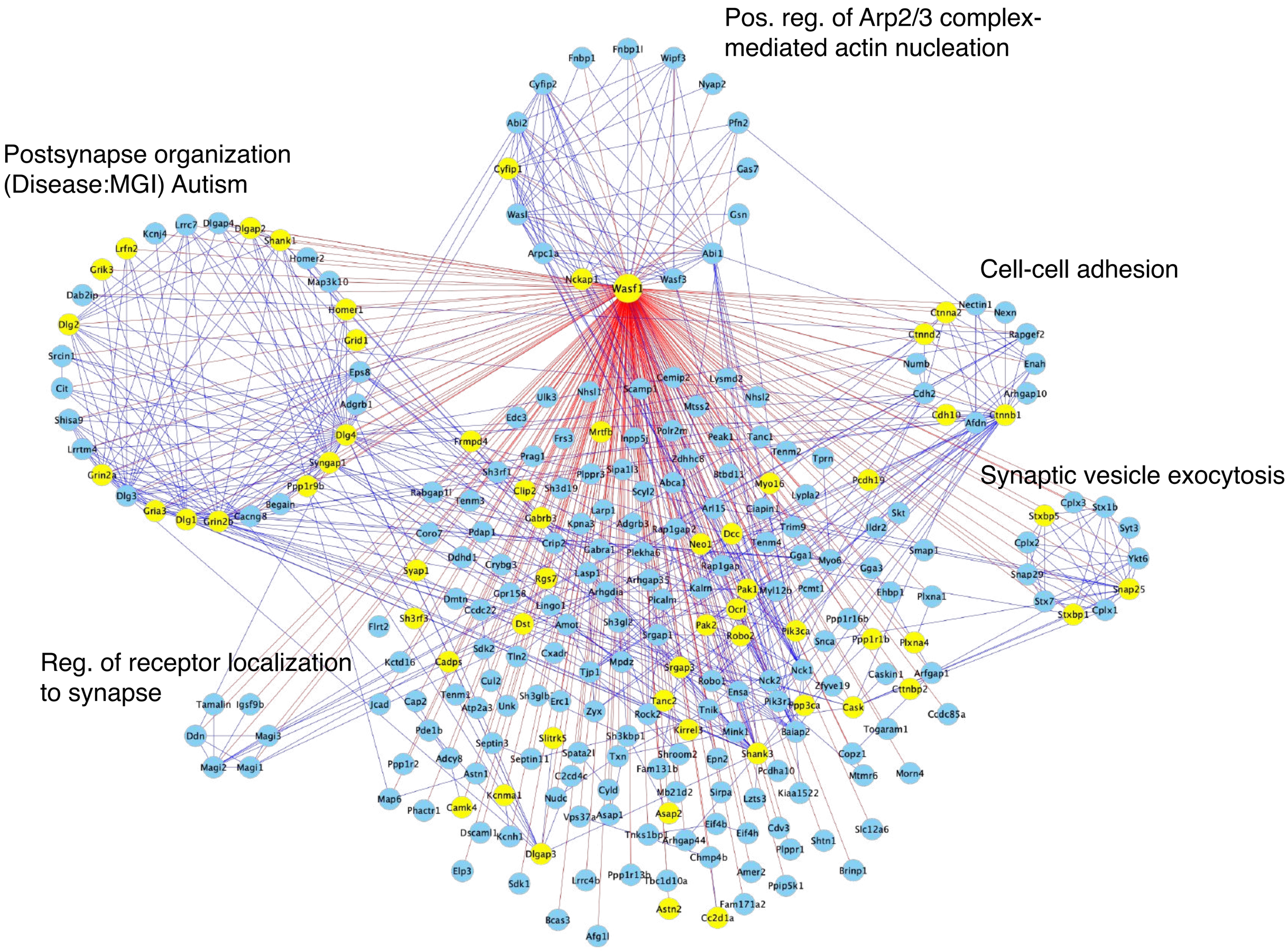

GO : Molecular Function

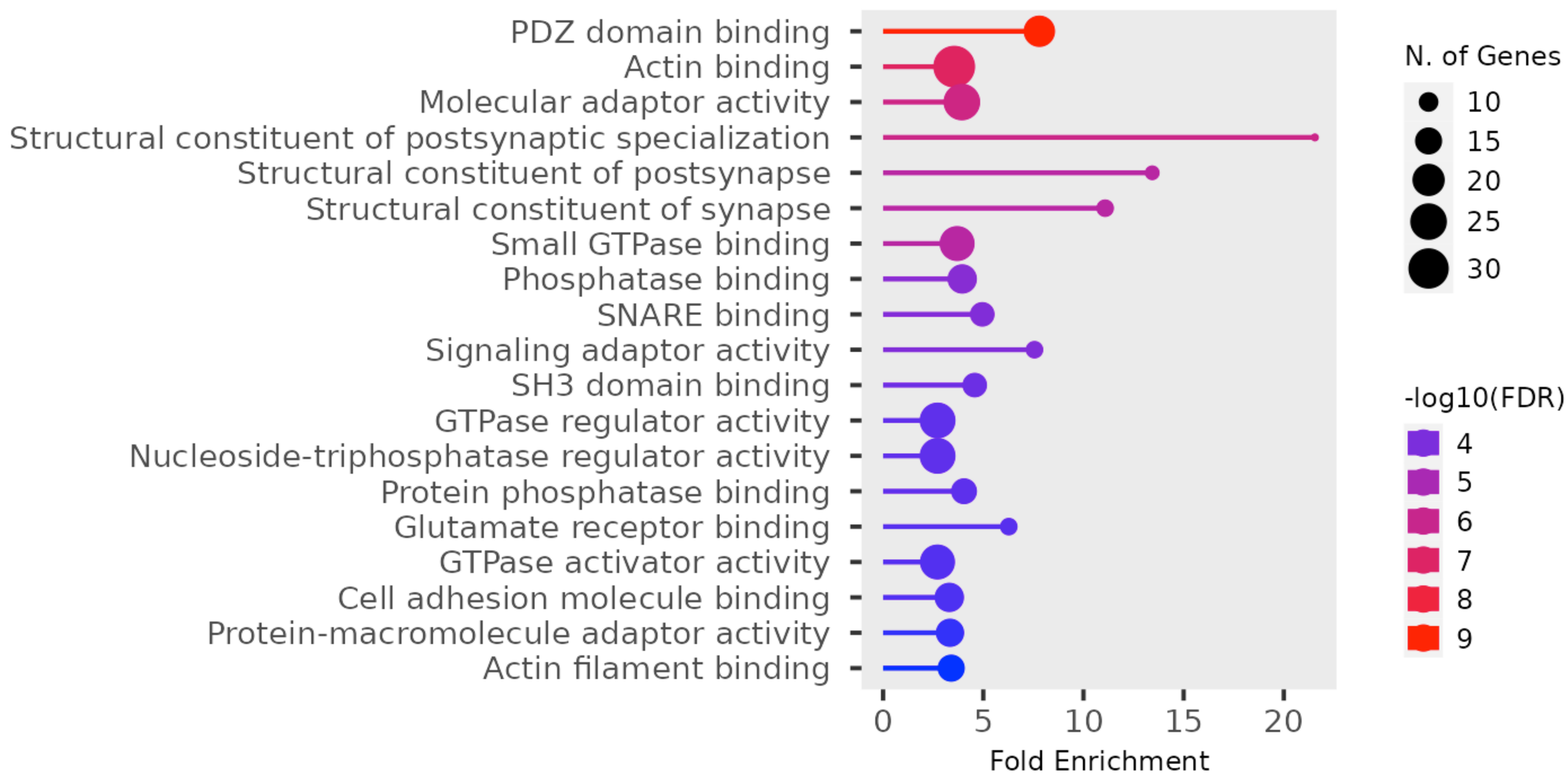

Supplementary Fig. S27

SynGO analyses

Anks1b

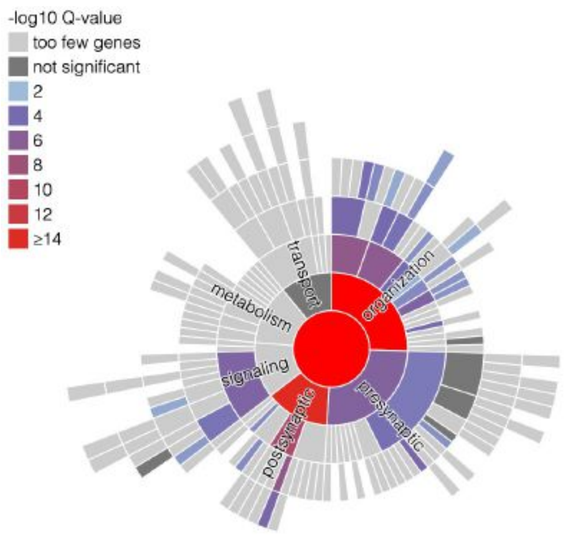

Syngap1

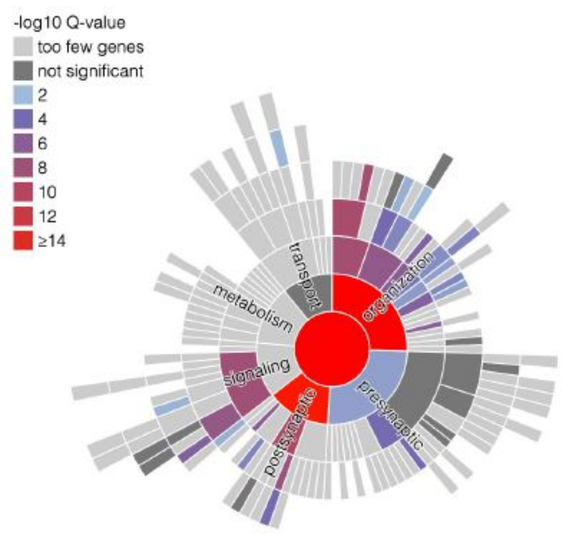

Shank2

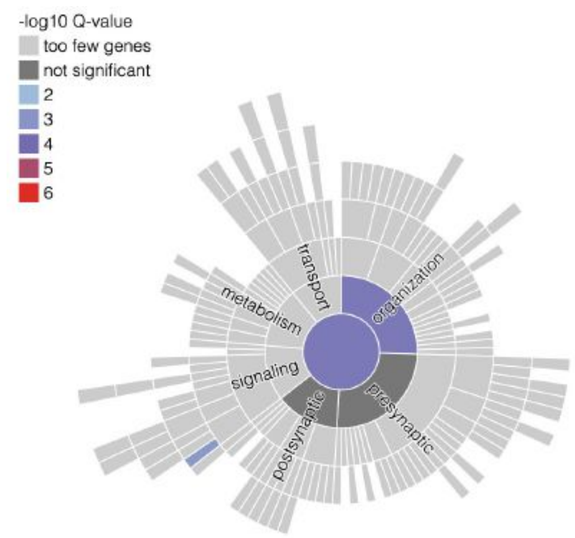

Shank3

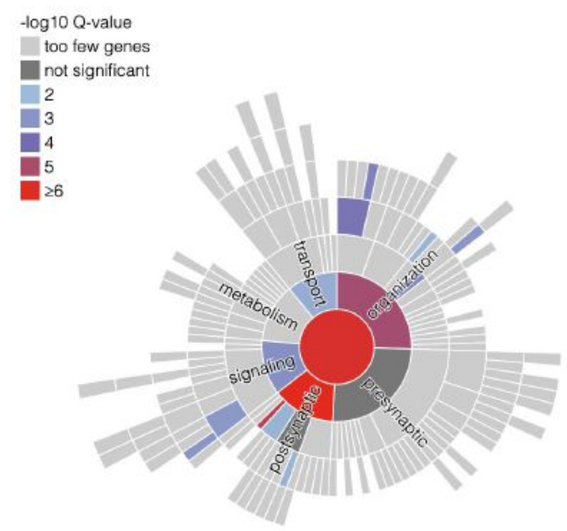

Nckap1

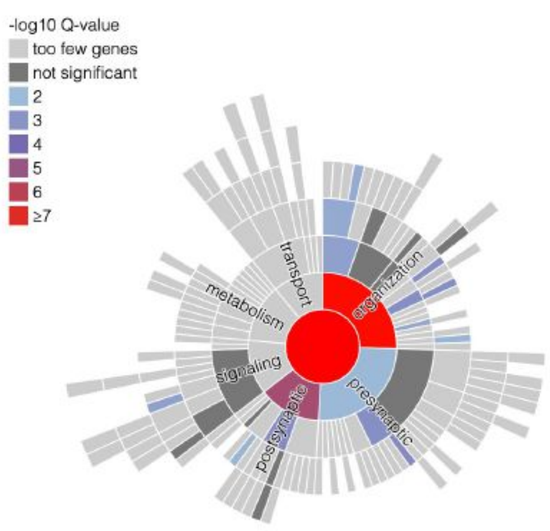

Nbea

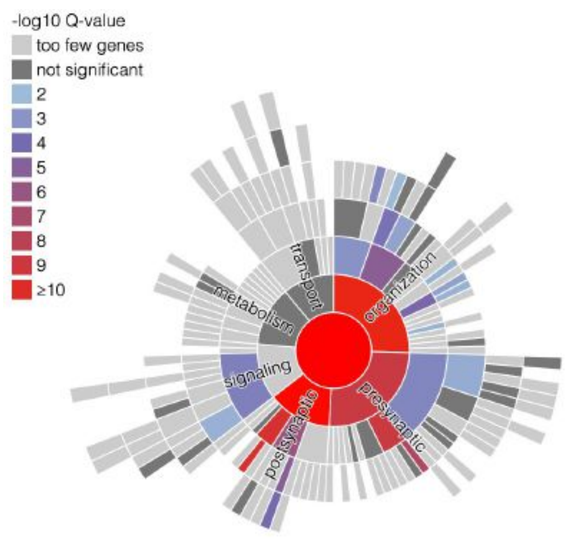

Ctnnb1

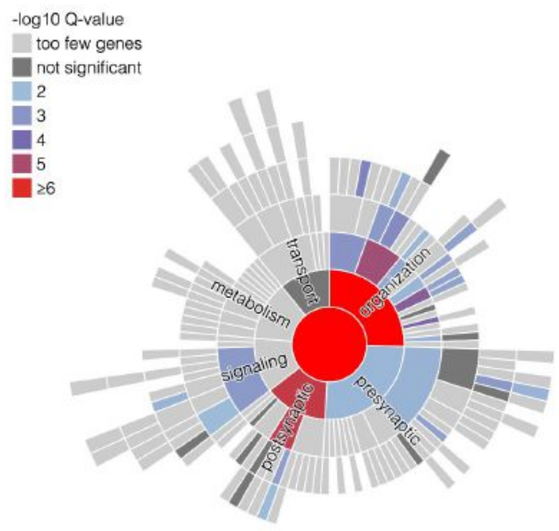

Lrrc4c

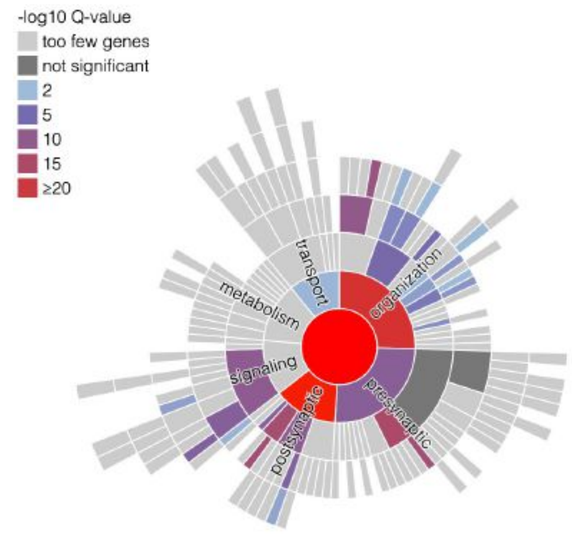

Iqsec2

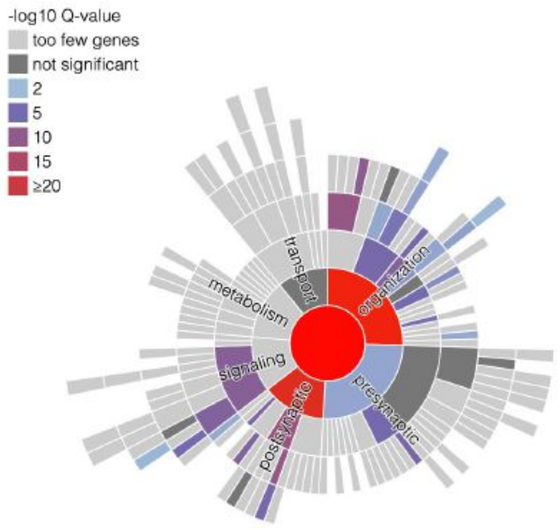

Arhgef9

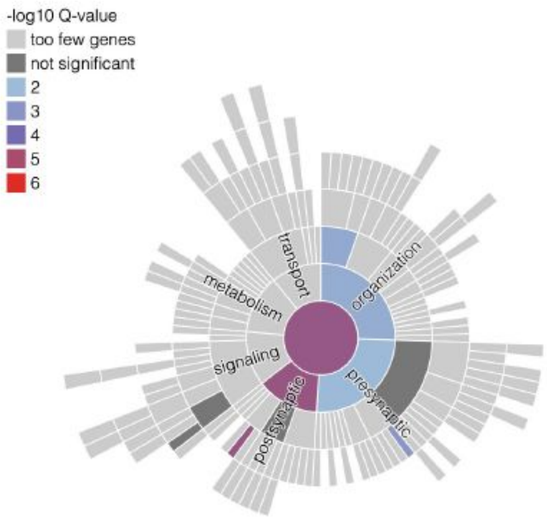

Homer1

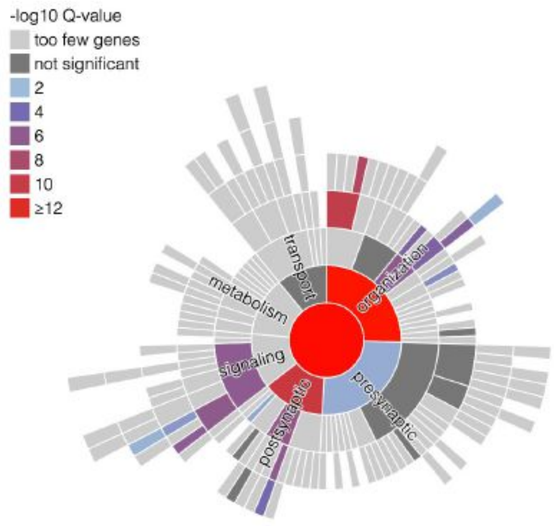

Wasf1

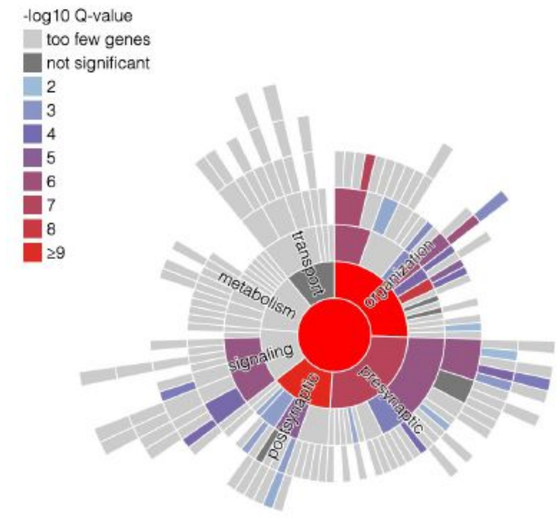

Hnrnpu

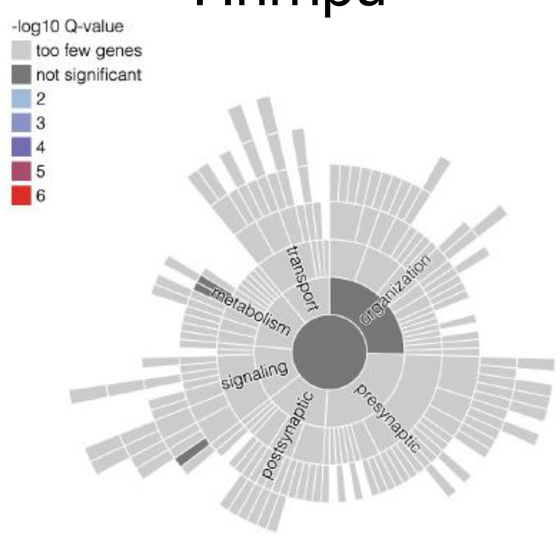

SynGO Reference Codes
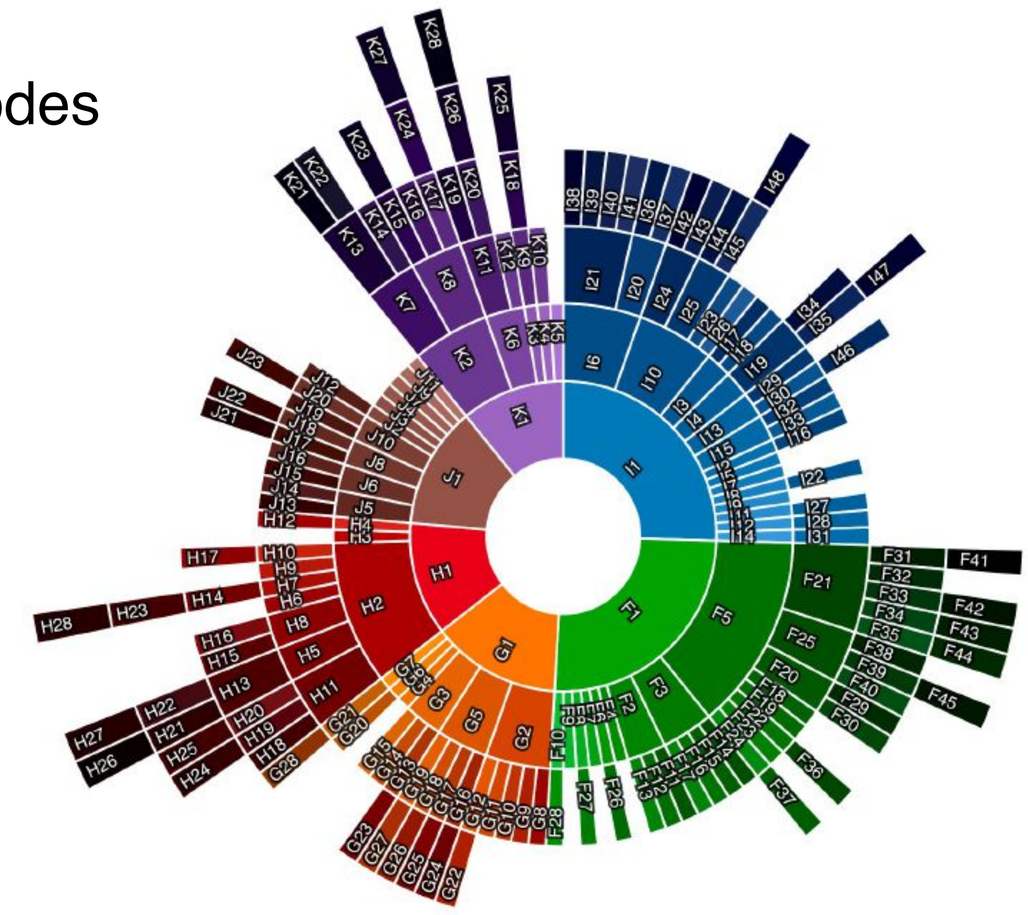
ontology term
- synapse organization
- process in the presynapse
- process in the postsynapse
- synaptic signaling
- metabolism
- transport